DISSERTATION


INITIATION AND INTENSIFICATION OF EAST PACIFIC EASTERLY WAVES



Submitted by

Adam V. Rydbeck

Department of Atmospheric Science



In partial fulfillment of the requirements

For the Degree of Doctor of Philosophy

Colorado State University

Fort Collins, Colorado

Fall 2015


Doctoral Committee:

    Advisor:  Eric Maloney

    Richard Johnson
    Thomas Birner
    Jeffrey Niemann

ABSTRACT

INITIATION AND INTENSIFICATION OF EAST PACIFIC EASTERLY WAVES

The background atmospheric state of the east Pacific (EPAC) warm pool in which easterly waves (EWs) develop varies dramatically on intraseasonal time scales. EPAC intraseasonal variability is well known to modulate local convective and circulation patterns. Westerly intraseasonal phases are associated with westerly low-level wind and positive convective anomalies and easterly intraseasonal phases are associated with easterly low-level wind and negative convective anomalies. This study first investigates the perturbation available potential energy (PAPE) and perturbation kinetic energy (PKE) budgets of easterly waves composited during westerly, easterly, and neutral intraseasonal phases, respectively. During neutral and westerly intraseasonal phases, the generation of PAPE associated with perturbation diabatic heating that is subsequently converted to PKE is enhanced and is the dominant energy source for EWs. EWs draw energy from low-level barotropic conversion, regardless of phase. A novel and previously unrecognized result is the detection of strong barotropic generation of PKE at midlevels during westerly intraseasonal phases. This previously unidentified source of PKE at midlevels is in part due to strong intraseasonal modulation of the background midlevel winds.

Processes associated with the local amplification of EWs in the EPAC warm pool are then explored. Developing EWs favor convection in the southwest and northeast quadrants of the disturbance. In nascent EWs, convection favors the southwest

ii

quadrant. In these quadrants, lower tropospheric vorticity is generated locally through vertical stretching that supports a horizontal tilt of the wave from the southwest to the northeast. EWs with such tilts are then able to draw energy via barotropic conversion from the background cyclonic zonal wind shear present in the east Pacific. EWs during westerly and neutral intraseasonal periods are associated with robust convection anomalies. Easterly intraseasonal periods are, at times, associated with very weak EW convection anomalies due to weaker moisture and diluted CAPE variations.

The in-situ generation of EWs in the EPAC is then investigated using the Weather Research and Forecasting Model (WRF). Sensitivity tests are performed to examine the atmospheric response to the removal of external and internal EW forcing in the EPAC warm pool. External forcing of EPAC EWs is removed by filtering EWs in wavenumber frequency space from the model's boundary forcing. Internal forcing of EWs is removed by reducing the terrain height in portions of Central and South America to suppress the strong source of diurnal convective variability in the Panama Bight. These regions of high terrain are associated with mesoscale convective systems that routinely initiate in the early morning and propagate westward into the EPAC warm pool. In both sensitivity tests, EW variance is significantly reduced in the EPAC, suggesting that both EWs propagating into the EPAC from the east and EWs generated locally in association with higher frequency convective disturbances are critical to EPAC EW variability.

A new mechanism is proposed to explain the in-situ generation of EPAC EWs. Serial mid-level diurnal vorticity and divergence anomalies generated in association with deep convection originating in the Panama Bight underpin the local generation,

intensification, and spatial scale selection of EW vorticity by vertical vorticity stretching. Diurnal vorticity anomalies in the Panama Bight are able to initiate disturbances capable of growing into robust EWs through a tendency to organize vorticity upscale.

# ACKNOWLEDGMENTS

I would like to thank those who have (un)intentionally encouraged, enthused, and educated me. Hopefully the preceding fortune of being endowed with such capable teachers and mentors will not be restricted in the future. In particular, I am grateful to Eric Maloney for his kindness, patience, resolve, and acumen, which helped to greatly offset my sporadic impatience, stubbornness, and misapprehension.

I am deeply thankful for my wife who continually uplifts and supports me. She is the hardest working person I know and a tremendous example.

PREFACE

"It is well known that the low latitudes furnish a large fraction of the heat needed to balance the radiation deficit elsewhere. If conditions are not steady but variable within the tropics, could one still maintain that the tropics are without influence on variations of the general circulation in middle and high latitudes? The last ten years have shown repeatedly that the investigator of the general circulation cannot proceed like a physicist who turns on a well-controlled flame underneath a tank and then proceeds without further reference to the flame."

– Herbert Riehl (1954)

"The school gives a man, Slotkin said, the fantastic amount of guts it takes to add to culture. It gives him morale, esprit de corps, the resources of many brains, and – maybe most important – one-sidedness with assurance. (My reporting what Slotkin said four years ago is pretty subjective – so let's say Vonnegut, a Slotkin derivative, is saying this.) About this one-sidedness: I'm convinced that no one can amount to a damn in the arts if he becomes sweetly reasonable, seeing all sides of a picture, forgiving all sins."

– Kurt Vonnegut (1951)

"They say the smart dog obeys, but the smarter dog knows when to disobey. Yes, she says, the smarter anything knows when to disobey."

– Amy Hempel (1983)

TABLE OF CONTENTS

**CHAPTER 1 Introduction**

**1.1 Purpose**

Easterly waves (EWs) are important to the tropical atmosphere because they provide a majority of the tropical convective variance at timescales less than 10 days (Kiladis et al. 2006), compose 25-40% of the deep convective clouds in the Intertropical Convergence Zone (ITCZ; Tai and Ogura 1987, Gu and Zhang 2002), and seed the majority of Atlantic and east Pacific tropical cyclones (e.g Avila and Guinney 2000, Avila et al. 2003, Pasch et al. 2009). The purpose of this study is to understand the processes by which EWs in the east Pacific (EPAC) initiate and mature.

**1.2 East Pacific Easterly Waves: An Overview**

EWs are off-equatorial low-pressure convective regions that migrate westward in tropical easterlies at approximately 8 m/s. EPAC EWs are characterized by wavelengths of 2500 – 3500 km and periods of 3 – 5 days (Tai and Ogura 1987, Serra et al. 2008). Many waves are identified on visible and infrared satellite imagery by inverted "V" shapes in the cloud field. Scatterometer winds are also used to identify cyclonic turning of surface winds associated with EW low-pressure centers. In many analyses, vorticity or meridional wind anomalies between 600-850 hPa are used to identify EWs. EWs also tend to have signatures in total precipitable water.

Previous studies have shown that EPAC EWs are energized by latent heating associated with deep convection and by the meridional shear of the mean zonal wind at low-levels (Maloney and Hartmann 2001, Serra et al. 2008). The latter is associated with a process called barotropic conversion. Chapter 2 discusses the vertical profile of

these kinetic energy tendency contributions and shows that strong barotropic conversions also occur in the middle troposphere in addition to previous work that highlighted lower tropospheric barotropic conversions (e.g. Maloney and Hartmann 2001). The presence of strong midlevel vorticity anomalies within EWs has been suggested as being critical to the development of tropical cyclones (Davis 2015). The processes by which EWs gain kinetic energy also display dramatic variations as the background atmospheric state of the EPAC changes. Intraseasonal variability in the EPAC is well known to modify the background atmospheric state that contributes to EW kinetic energy increases (Maloney and Hartmann 2001). The byproduct of these variations in the background state is a significant increase in tropical cyclogenesis events in the EPAC and Gulf of Mexico (Maloney and Hartmann 2000). The strong intraseasonal variations in the transfer of EW available potential energy to EW kinetic energy as well as those in the barotropic conversion are also examined in Chapter 2.

The organization of moisture and convection surrounding EPAC EWs has received relatively little attention as of late; in contrast to the ever-increasing resolution and coverage of EW cloud properties by satellites. The spatial structure of convection in relation to Atlantic EW troughs was a primary concern when satellite data was initially made available in the late 1960s with the TIROS satellite. Prior to that, Herbert Riehl considered the distribution of moisture in relation to the circulation of EWs in the Intra-Americas Seas a primary concern and was one of the first to hypothesize mechanisms responsible for their spatial arrangement. However, the organization of moisture and convection with relation to EPAC EWs has not been thoroughly addressed. In light of recent advances in assimilating data from past and current satellites, such as the

National Climatic Data Center high resolution outgoing longwave radiation dataset, it appears timely to improve our understanding of the distribution (and the processes determining the distribution) of moisture surrounding EWs. I'm sure Herbert Riehl would agree. The distribution within and interactions of convection with the EW circulation are investigated in Chapter 3.

According to forecasters at the National Hurricane Center, approximately 70% of tropical cyclogenesis events in the EPAC are said to be associated with EWs propagating from West Africa (percentage is calculated by cataloging the origins of tropical cyclones listed in the reports produced by the National Hurricane Center from 1997-2011). Approximately 5% of tropical cyclogenesis events are said to develop exclusively from in-situ sources and the remaining 25% of events are not detailed. An important assumption included in the calculation of these statistics is that a continuum of EWs is presumed to exist between West Africa and the EPAC, even when such waves are not observable. Chapter 4 proposes a novel mechanism by which diurnal anomalies can organize vorticity upscale in the Panama Bight such that EW vorticity is generated locally, as documented in a full-physics regional model. This mechanism does not require any external assistance such as remote tropical synoptic forcing from the Atlantic or West Africa.

## 1.3 Study Overview

The purpose of this research is to determine the behavior and mechanisms of EPAC EW initiation and growth in observations, reanalysis, and regional climate simulations. In Chapter 2, the vertically integrated perturbation available potential and kinetic energy budgets of EPAC EWs are investigated using reanalysis. This includes an examination

of the sensitivity of EW energy budgets to intraseasonal variations in the background state of the EPAC. In Chapter 3, the coupling between EW convection and circulation anomalies that helps energize the wave and determine its vorticity structure are investigated using satellite observations and reanalysis. Finally, regional model simulations that test the sensitivity of EPAC EW formation to remote and in-situ forcings are analyzed in Chapter 4. The roles of diurnal transients in the initiation and growth of EPAC EWs are also investigated. Chapter 5 presents a summary of the primary findings, suggests strategies to improve forecasts of EPAC EWs, and discusses approaches to address questions for future work.

**CHAPTER 2 Energetics of East Pacific Easterly Waves during Intraseasonal Events[1]**

## 2.1 Introduction

The east Pacific (EPAC) background state that fosters the development of easterly waves (EWs) exhibits significant variability on intraseasonal timescales during boreal summer. Low-level zonal winds and precipitation in the EPAC warm pool contain significant spectral peaks near 50-days during boreal summer (Maloney and Hartmann 2001; Maloney and Esbensen 2003, Maloney and Esbensen 2007, Maloney et al. 2008, Jiang and Waliser 2008, Jiang and Waliser 2009, Small et al. 2011, Rydbeck et al. 2013). Observed EPAC intraseasonal events are thought to be synchronized to intraseasonal variability in the Eastern hemisphere via rapid Kelvin wave propagation across the equatorial Pacific (Maloney et al. 2008, Rydbeck et al. 2013). However, modeling results of Rydbeck et al. (2013) suggest that EPAC intraseasonal variability can also occur independently of such Kelvin wave communication. In either case, EPAC intraseasonal events are characterized by alternating easterly and westerly low-level zonal wind anomalies. Low-level easterly intraseasonal wind anomalies are associated with suppressed intraseasonal convective and surface flux anomalies in the EPAC warm pool. Westerly intraseasonal wind anomalies are associated with enhanced intraseasonal convective and surface flux anomalies (Maloney and Hartmann 2001).

Intraseasonal variability has been shown to be statistically and dynamically linked to EPAC synoptic eddy activity. When EPAC EWs were first analyzed by Nitta and

---

Takayabu (1985), they noted strong correlations between EPAC EW activity and intraseasonal variability using data from just one summer season. Easterly waves are said to be responsible for seeding a majority of the tropical cyclones in the EPAC (e.g. Avila and Guiney 2000, Avila et al. 2003, Pasch et al. 2009). Maloney and Hartmann (2000) showed that westerly intraseasonal phases are associated with a 4 times greater likelihood of EPAC tropical cyclogenesis than easterly intraseasonal phases due to favorable cyclonic shear of the low-level zonal wind anomalies there. They also argued that EW activity supporting genesis was enhanced during westerly intraseasonal phases by satisfying the Charney and Stern (1962) necessary condition for barotropic instability through a reversal of the meridional potential vorticity gradient. Barotropic instability is also thought to strengthen EWs transiting from Africa upon their entry into the EPAC (Molinari et al. 1997, Molinari and Vollaro 2000). Conversely, easterly intraseasonal phases favor enhanced anticyclonic shear and low-level divergence anomalies, suppressing tropical cyclogenesis.

Conversions of perturbation available potential energy (PAPE) to perturbation kinetic energy (PKE) and barotropic conversion of PKE have been suggested as important to the growth of EWs in the EPAC (Maloney and Hartmann 2001, Maloney and Esbensen 2003, Serra et al. 2008, Serra et al. 2010). PAPE is destroyed and PKE is created by rising (sinking) warm (cold) anomalies. In evaluating this contribution to the PKE budget, Serra et al. (2008) concluded that latent heating was critical to the generation of PAPE that subsequently drives increases in PKE. East Pacific intraseasonal variability is well known to modulate convection and likely affects PAPE to PKE conversions. Barotropic conversions at low levels are also notably different

between westerly and easterly phases of EPAC intraseasonal events due to marked shifts in the magnitude and direction of the mean wind. At 850 hPa, barotropic conversions during westerly intraseasonal events are approximately 6 times greater than during easterly events (see Figure 2.10, Maloney and Hartmann 2000). The results of this study will also show that barotropic conversion in the middle troposphere dramatically increases during westerly intraseasonal events compared to easterly intraseasonal events.

Significant intraseasonal events have been shown to be present during 60% of the boreal summer season in the EPAC (Maloney and Hartmann 2000). By averaging over the different regimes of westerly and easterly intraseasonal periods, the climatological fields may not be representative of the varying background field that EWs feel during a given time. This is especially critical when the intraseasonal anomalies are of comparable magnitude to the climatological field, as is the case in the low-level wind field of the EPAC warm pool. Because the climatological low-level winds in the EPAC warm pool are weak westerlies, intraseasonal wind anomalies are easily able to alter the direction of the total wind by 180° (see Figure 2.12, Maloney and Esbensen 2007). Alterations of the total zonal wind direction are more even more easily achieved during El Niño periods when the background westerlies are reduced in amplitude (Harrison and Larkin 1998).

This paper investigates the vertically averaged budgets of PKE and PAPE as a function of the phase (westerly, easterly, and neutral) of EPAC intraseasonal events to determine the importance of the background state for EW energetics. Previous studies have assumed that most of EPAC EWs are a result of EWs propagating continuously

across the Atlantic and Caribbean from Africa (e.g. Avila and Pasch 1992, Avila and Pasch 1995, Beven et al. 2005). In contrast, we are interested in determining if local EPAC energetic conversions are sufficient such that EWs are able to initiate and grow in-situ as suggested in pioneering (Nitta and Takayabu 1985, Tai and Ogura 1987) and later (Maloney and Hartmann 2001, Serra et al. 2008, Serra et al. 2010) studies of EPAC EWs. Section 2.2 describes the data and the methods for identifying EWs and categorizing the waves by intraseasonal phase. Section 2.3 describes the composite structure and characteristics of EWs during different intraseasonal phases. Sections 2.4 and 2.5 describe the analysis of the vertically averaged PAPE and PKE budgets composited over each intraseasonal phase. Section 2.6 examines the vertical structure of the barotropic conversion during each intraseasonal phase. Section 2.7 presents a discussion and conclusions.

## 2.2 Data and Methods

The European Center for Medium-Range Weather Forecasts Interim Reanalysis (ERAi) (Dee et al. 2011) from 1991-2010 is used for the study. The 6 hourly, 1.5° grid spaced data is used to calculate the total, mean, and perturbation fields. Mean fields are calculated by applying a ten-day running mean to the total fields and perturbation fields are calculated as deviations from the ten-day running means. The data is collected at 50 hPa intervals from 1000 hPa to 200 hPa.

Intraseasonal events are identified by taking the first principal component (PC) of 30 - 90 day bandpass filtered 850 hPa zonal wind anomalies over the domain 0° - 25.5°N, 120°W - 75°W that explains 63% of the intraseasonal variance, similar to the methods of Maloney and Hartmann (2001). The corresponding empirical orthogonal

function (EOF) structure (not shown) is that of a zonal wind jet centered about 11°N, similar to Figure 1 of Maloney and Hartmann (2001). After the PC is normalized, local maxima greater than 1.0 are defined as westerly intraseasonal events. Local minima less than -1.0 are defined as easterly intraseasonal events. Values between 0.5 and -0.5 are defined as neutral intraseasonal periods with the center of the event defined as the time step nearest 0.0 of the normalized PC. Events are limited to boreal summer (June – October) when EPAC intraseasonal variability is strongest (Maloney and Hartmann 2000, Maloney and Esbensen 2003). Over the twenty years of data, 41 westerly events, 42 easterly events, and 126 neutral periods are identified. Each event is defined to include the 5 days before and after the event's peak. This index is referred to as the intraseasonal events index. Based on selection with the index, no overlapping of intraseasonal events occurs (e.g. positive events with neutral periods). Composites of the total 850 hPa wind field for neutral, westerly, and easterly intraseasonal events are included in Figures 6, 7, and 8, respectively.

Easterly waves require robust identification methods, as simple time filtering does not isolate EW anomalies from phenomena with similar timescales such as mixed Rossby-gravity waves and tropical cyclones. Criteria are established to detect prolonged and intense EWs. First, 2.5 – 12 day bandpass filtered 700 hPa vorticity anomalies are calculated. Eigenanalysis is performed on the filtered vorticity anomalies over the domain 3°N – 19.5°N, 134°W – 81.5°W. The first two PCs calculated from the filtered vorticity anomalies are significantly different from lower modes according to the criterion of North et al. (1982), and explain 5.6% and 5.5% of the variance, respectively. The PCs have a correlation of 0.84 when $PC_2$ leads $PC_1$ by 1.25 days, significant at the

95% confidence level. The complimentary EOFs are a quadrature pair and describe a northwestward propagating signal. The EOF structure is similar to that of the composite anomalous vorticity field shown in Figure 1. As a result, EW phase and amplitude can be calculated from the normalized PCs using the following formulas:

$$\text{Amplitude} = \sqrt{PC1^2 + PC2^2} \, ,$$

$$\text{Phase} = \arctan\left(\frac{PC1}{PC2}\right).$$

Easterly waves are selected if the amplitude of the normalized PC pair exceeds 0.5 over 8 consecutive 45° phases ranging from 0° - 360°, similar to the methods of detecting EWs used in Lau and Lau (1992) and Maloney and Dickinson (2003). These thresholds for selecting EWs are the same for neutral, westerly, and easterly intraseasonal events. Easterly waves composite structures (shown in Figures 1, 2, and 3) are robust to reasonable changes in the amplitude threshold. There are 227 EWs that meet the criteria with an average length of 5.25 days such that each phase represents 15.75 hours of the cycle. Qualifying EW phases are then sorted into intraseasonal phases using the intraseasonal events index. Approximately 101, 29, and 28 EWs are selected for neutral, westerly, and easterly intraseasonal phases, respectively. By construction, the EW phases are periodic and phase composites of EWs can be followed continuously from the end at phase 8 back to the beginning at phase 1 (see Figures 1, 2, and 3). For energy budget calculations, EW energetics are composited over all qualifying EW phases for each respective intraseasonal phase. As a note, the PKE budget was also performed without any subsetting of the record based on EW amplitude or phase such that all times are included during positive and negative events

and neutral periods. Apart from slightly weaker amplitudes, the results and conclusions are unchanged.

Easterly waves are said to seed the majority of tropical cyclones in the EPAC, and these tropical cyclones understandably project strongly onto 2.5 – 12 day filtered anomaly fields used for studying EWs. Because we are only interested in investigating the anomalies related to EWs, we attempt to suppress the effects of strong tropical cyclones in the ERAi data. Tropical cyclones are identified using the 850 hPa vorticity, similar to the methods of Vitart and Stockdale (2001). Local maxima greater than $7.5*10^{-5}$ s$^{-1}$ are considered tropical cyclone strength. After identifying the 850 hPa vorticity maximum of the tropical cyclone, the anomalies of all fields are weighted by the function used in Aiyyer et al. (2012) to remove tropical cyclone anomalies:

$$w(x,y) = 1 - \exp\left[ -\frac{r^2 \ln(4)}{2R^2} \right]$$

where $r = r(x,y)$ is the distance of a given grid point from the tropical cyclone center and $R = 500$ km sets the length scale for the weighting function. The weighting function is applied at each vertical level to a 6° x 6° horizontal box centered on the tropical cyclone. Examination of 2.5 – 12 day bandpass filtered 850 hPa relative vorticity variance maps (not shown) ensured that strong tropical cyclones are adequately being removed using this method. Similar results were found using relative vorticity at other levels in the lower troposphere and reasonable variations to the threshold value.

## 2.3 Easterly waves During Intraseasonal Events

Before examining the energy budgets of EWs, we first investigate variations in the EW life cycle as a function of intraseasonal phase. The analysis of EW evolution proves

useful when examining the energetic contributors to EW growth in later sections. Figure

2.1 shows 2.5 – 12 day bandpass filtered outgoing longwave radiation (OLR), 700 hPa

### Easterly Wave Composite (Neutral)
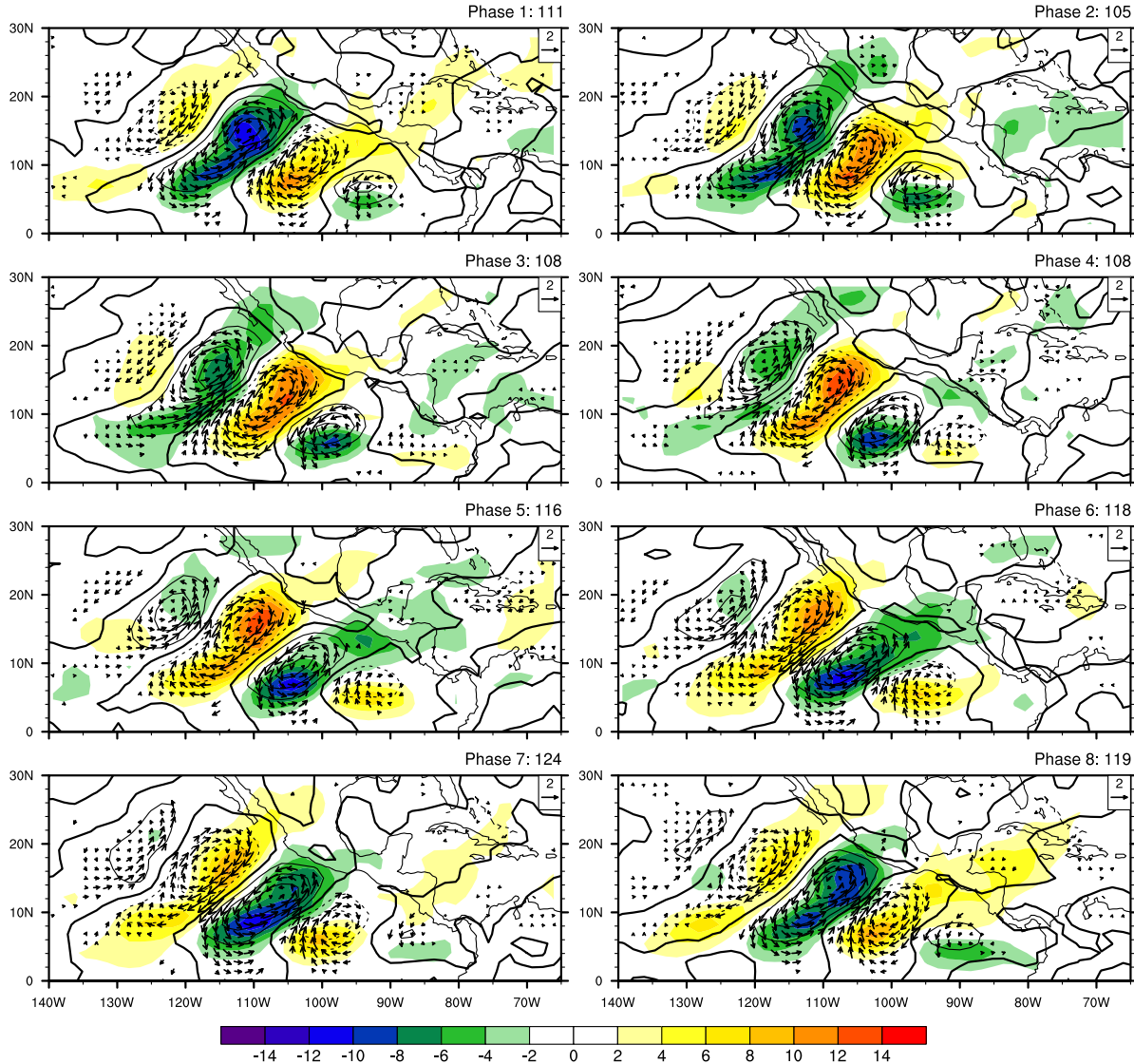


Fig. 2.1 Composite of easterly waves during neutral intraseasonal periods showing 2.5 – 12 day bandpass filtered 700 hPa wind (ms^{-1}, vectors), relative vorticity (*10[-6] s^{-1}, line contours), and outgoing longwave radiation anomalies (Wm[-2], color contours). Vorticity contour interval is 3*10[-6] s^{-1}. Positive (negative) line contours are solid (dashed). The thick solid line is the zero contour. The reference vector is located in the upper right of each panel. Anomalous winds are only plotted in regions where the anomalous vorticity is statistically significant from zero at the 95% confidence level. Easterly wave phase and the number of days used to composite each phase are shown above each panel.

horizontal wind, and 700 hPa vorticity anomalies as a function of EW phase composited over neutral intraseasonal periods. Wind anomalies are only plotted where the vorticity anomalies are significantly different from zero at the 95% confidence level. OLR is used as a proxy for deep convection. During neutral periods, significant EW circulation anomalies begin near 6°N, 87°W on the cyclonic shear side of the Papagayo jet (Chelton et al. 2000a,b) exit region as shown in phase 7. The circulation center appears slow to intensify on the southeast tail of the wave train through phases 8 and 1. By phase 2, approximately one and a half days after the wave's first appearance in phase 7, the nascent positive vorticity center has strong and persistent OLR anomalies near 7°N, 96°W. By phase 4, the developing EW center exhibits a southwest to northeast horizontal tilt and begins to intensify more rapidly through phase 7. During the mature stage of the positive vorticity center seen in phase 8, strong OLR anomalies are present in the northeast quadrant of the wave, similar to regression plots in Serra et al. (2008). Wave trajectories parallel the coasts of Central America and Mexico, but anomalies remain primarily over the EPAC. Significant vorticity anomalies in the EPAC suggest little connection with those in the Gulf of Mexico and Caribbean Sea.

Figure 2.2 shows similar EW composites for westerly intraseasonal events. Compared to EW composites during neutral periods, those during westerly intraseasonal events establish strong and persistent OLR anomalies quicker near 7°N, 93°W of phase 1 and intensify earlier in the life cycle, closer to the Central American coast. Mature EWs during westerly intraseasonal events have larger negative OLR and positive vorticity anomalies that are oriented along a southwest to northeast tilt of the trough axis. During mature EW stages in phases 7 and 8, the strongest OLR anomalies

are positioned north of the vorticity anomaly maximum. Interestingly, during phases 6, 7, and 8, the two OLR maxima located on the poleward and equatorward flanks of the intensifying EW trough migrate and grow towards the positive vorticity center.

Easterly Wave Composite (Westerly)
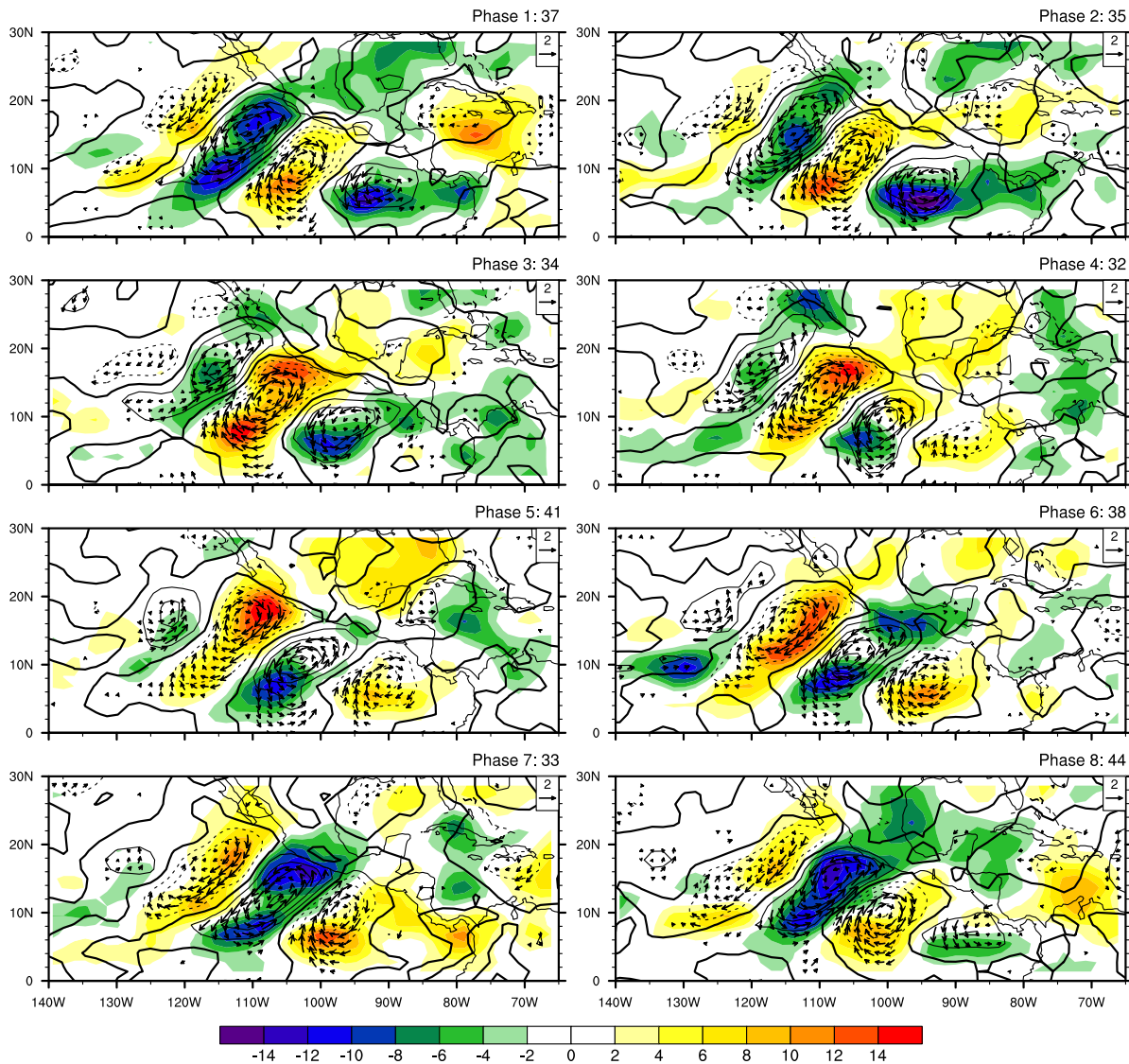


Fig. 2.2 Same as Fig. 2.1, except for westerly intraseasonal events.

During easterly intraseasonal events, EW OLR and 700 hPa vorticity anomalies are weaker than those during westerly intraseasonal events (Figure 2.3). Like neutral periods and westerly intraseasonal events, nascent EW circulation features originate

14

near the exit region of the Papagayo jet, but are much slower to develop. During the developing stages, the vorticity maximum is displaced equatorward of the broader

## Easterly Wave Composite (Easterly)



Fig. 2.3 Same as Figs. 2.1 and 2.2, except for easterly intraseasonal events.

cyclonic circulation. Easterly waves do not appear to intensify until they reach 110°W (phase 6). OLR anomalies during mature EW stages (phases 8, 1, and 2) are displaced east of the 700 hPa anomalous vorticity center. The trajectories of EWs are shifted southward relative to neutral and westerly intraseasonal events, tracking further away

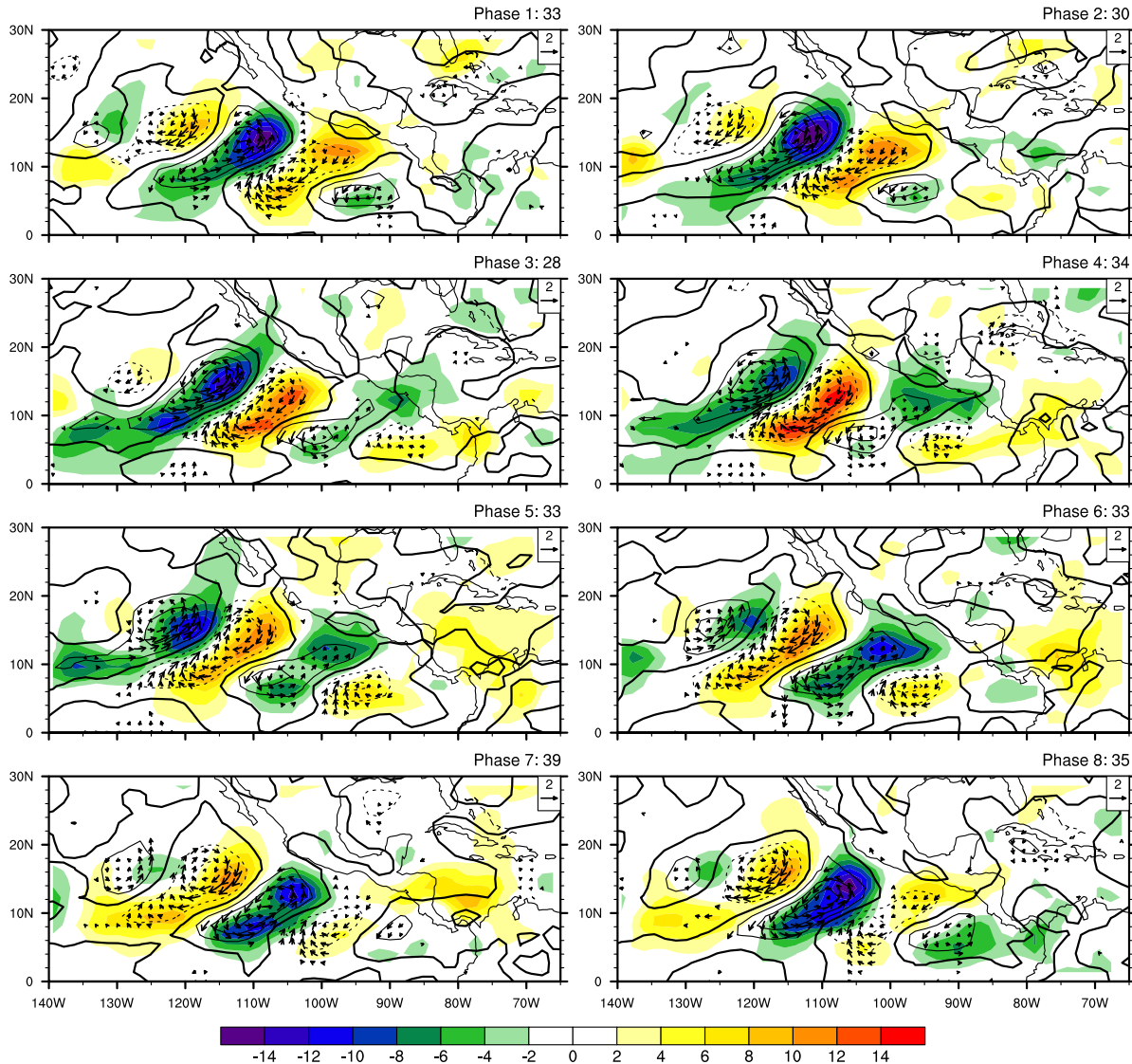from the Central American and Mexican coast. To note, composites of EWs for the respective intraseasonal phases are similar if instead EW EOFs/PCs are computed separately for neutral, westerly, and easterly intraseasonal periods.

Statistically significant differences of composited vertically averaged total PKE exist between westerly and easterly intraseasonal phases (Figure 2.4). PKE is represented by

$$K' = \frac{1}{2}(\overline{u'^2} + \overline{v'^2}).$$

Over-barred fields represent ten-day running means and primed quantities represent deviations from the ten-day running means. Total PKE has a local maximum in the EPAC between 100°W-115°W, 8°N-17°N during neutral periods with values from 9 – 10.5 $m^2s^{-2}$ (Figure 2.4a). This region is increased in amplitude during westerly intraseasonal events and extends farther east towards Nicaragua (Figure 2.4b). During easterly intraseasonal events, PKE is significantly reduced by approximately 35 - 40% compared to westerly intraseasonal events (Figure 2.4b,c) in regions of strong EW activity (see Figures 2.1, 2.2, and 2.3).

For neutral, westerly, and easterly intraseasonal phases, EW composites display differing intensities of vorticity and OLR anomalies, latitudes and longitudes of intensification, phasing of convective and low-level vorticity anomalies, and propagation characteristics. Additionally, statistically significant differences in vertically averaged total PKE are present between westerly and easterly intraseasonal events. To better understand the assorted characteristics of EWs for different intraseasonal phases, we examine the vertically averaged PAPE and PKE budgets of EWs calculated as a function of the intraseasonal background state.

# Total Perturbation Kinetic Energy
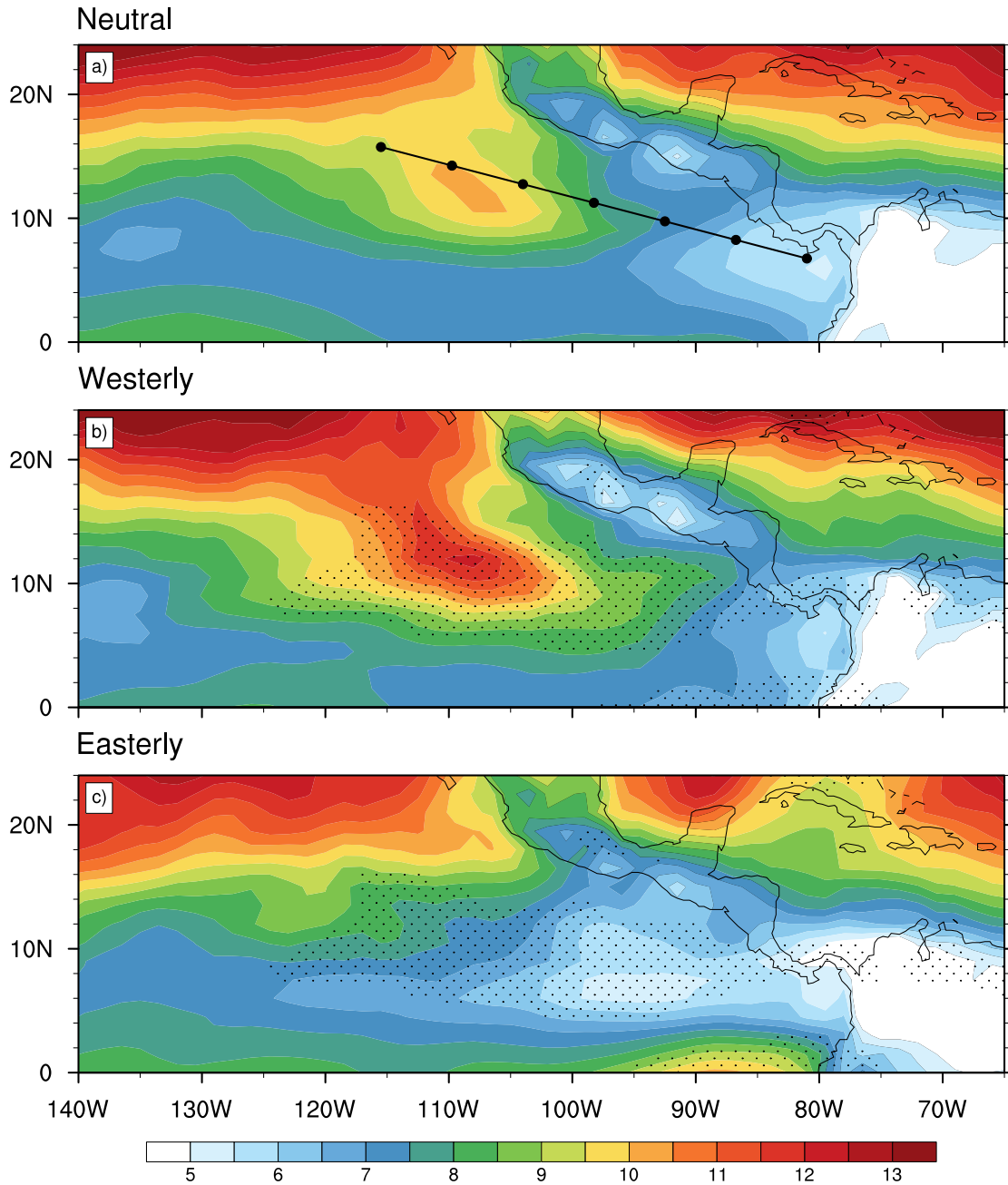


Fig. 2.4 Composites of vertically averaged total perturbation kinetic energy for a) neutral, b) westerly, and c) easterly intraseasonal events. Units are $m^2s^{-2}$. Stipling in b) and c) indicates areas where total PKE during westerly intraseasonal events is significantly different from total PKE during easterly intraseasonal events at the 95% confidence level. The black line and dots in (a) represent the cross section axis used in subsequent analysis.

## 2.4 Perturbation Available Potential Energy Budget

To investigate the importance of diabatic as well as baroclinic energy sources that perhaps arise from strong land-sea temperature contrasts that aid baroclinic energy conversions, we calculate the vertically averaged PAPE budget similar to that in Norquist et al. (1977) and Lau and Lau (1992). The approximate form of the PAPE budget used is:

$$\frac{\partial A'}{\partial t} \approx \gamma(\overline{Q_1'T'})/\overline{T} + R\left(\overline{\omega'T'}\right)/p \; - \; c_p\gamma\left(\overline{V_h'T'\cdot\nabla_h\overline{T}}\right)/\overline{T} \qquad (1)$$

where the PAPE is represented by

$$A' = c_p\gamma\overline{T'^2}/2\overline{T},$$

the perturbation apparent heat source is approximately given by

$$Q_1' \approx c_p\frac{\partial T'}{\partial t} - c_p\left(\omega'\overline{\sigma} - V_h'\cdot\nabla_h\overline{T}\right),$$

the static stability is represented by

$$\sigma = \frac{RT}{c_p p} - \frac{\partial T}{\partial p},$$

$\gamma = \Gamma_D/(\Gamma_D - \Gamma)$, $\Gamma_D$ is the dry adiabatic lapse rate, $\Gamma$ is the observed lapse rate, $c_p$ is the specific heat at constant pressure, $T$ is the temperature, $\omega$ is the vertical pressure velocity, $V$ is the three dimensional velocity vector, $V_h$ is the horizontal velocity vector, $R$ is the gas constant for dry air, and $p$ is the pressure. $\gamma$ is limited to magnitudes less than 50 to omit observed lapse rates nearing the dry adiabatic lapse rate which makes A' ill-defined. Over-barred fields represent ten-day running means and primed quantities represent deviations from the ten-day running means. The first term on the right side of equation (1), $\gamma(\overline{Q_1'T'})/\overline{T}$, is the generation of PAPE through the correlation of the

perturbation apparent heat source and temperature. The second term of (1), $R\left(\overline{\omega'T'}\right)/p$, is the destruction of PAPE through conversions to PKE. The third term of (1), $-c_p\gamma\left(\overline{V_h'T'}\cdot\nabla_h\overline{T}\right)/\overline{T}$, is the conversion of mean available potential energy to PAPE. Composite terms are calculated by averaging over strong EW periods as designated by the EW index for each intraseasonal phase. The terms are vertically averaged from 1000 hPa to 200 hPa.

The generation of PAPE by perturbation diabatic heating, $\gamma(\overline{Q_1'T'})/\overline{T}$, largely balances conversions of PAPE to PKE, $R\left(\overline{\omega'T'}\right)/p$, during neutral periods (Figure 2.5a,b). Conversion of mean available potential energy to PAPE is generally an order of magnitude smaller than the other leading terms in the budget (not shown), similar to the findings of Serra et al. (2008). To first order, baroclinic conversion of PAPE by eddies acting on the mean temperature gradient are not critical to the PAPE budget in the EPAC and western Caribbean. Both the generation of PAPE by perturbation diabatic heating and the conversion of PAPE to PKE maximize in an ellipse centered near 11°N, 105°W. These large values extend eastward toward a second maximum in the Panama Bight. The two maxima are separated by weaker values located near 9°N, 103°W. This location is near the Costa Rica Dome, a region of shallow oceanic thermocline, decreased sea surface temperature, enhanced static stability, and reduced annual convection (Xie et al. 2005).

Westerly events are characterized by stronger generation of PAPE by perturbation diabatic heating and conversion of PAPE to PKE, with stronger conversions appearing more continuous across the path of EW propagation than during
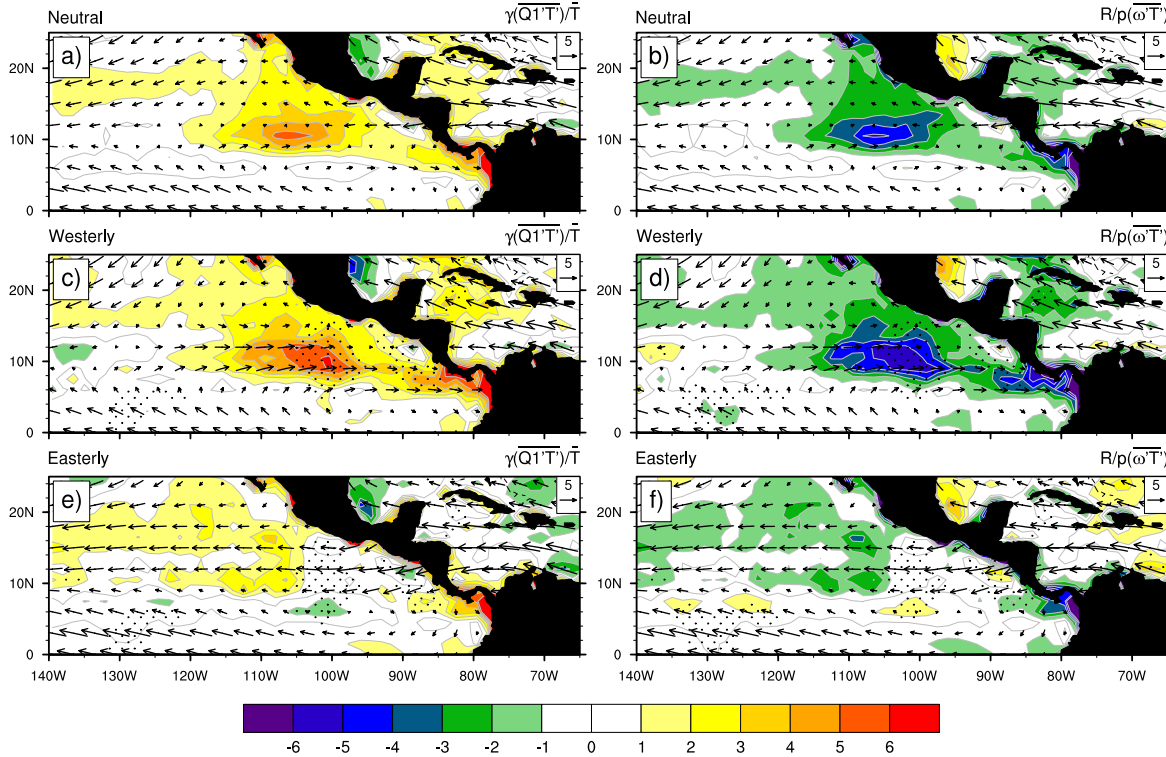
## PAPE Composite Terms



Fig. 2.5 Composites of vertically averaged $\gamma(\overline{Q_1'T'})/\overline{T}$ (left column) and $R(\overline{\omega'T'})/p$ (right column) of the PAPE budget over a) and b) neutral, c) and d) westerly, and e) and f) easterly intraseasonal events. Values are $*10^{-5}$ ($m^2s^{-2}$)$s^{-1}$. Stipling in c), d), e), and f) indicates significantly different areas between westerly and easterly intraseasonal events at the 95% confidence level. Composite total 850 hPa winds with tropical cyclone anomalies removed are shown for each respective intraseasonal phase. The reference vector is located in the upper right of each panel.

neutral periods (Figure 2.5c,d). Values that are statistically different from those during easterly intraseasonal events at the 95% confidence level are stippled. The generation of PAPE by perturbation diabatic heating (and thus the budget) is largely balanced by the conversion of PAPE to PKE. The maximum (minimum) of the generation (conversion) term during westerly events located near 10°N, 100° W is approximately 15% stronger than during neutral periods and is substantially and significantly different than during easterly intraseasonal events. Values near Panama are also stronger and

extend farther westward into the EPAC warm pool than during neutral periods, weakening near the Costa Rica Dome. Thus, the generation of PAPE and conversion to PKE is stronger and more continuous across EW paths during westerly intraseasonal events compared to neutral periods.

For easterly intraseasonal events, PAPE generation and conversion terms are generally weakened in the EPAC warm pool, except for a limited region in the Panama Bight where values remain semi-constant across all intraseasonal phases (Figure 2.5e,f). This region does not extend westward as during neutral and westerly intraseasonal events. Generation of PAPE and conversion to PKE do not appear to strongly contribute to EW energetics during easterly intraseasonal events, in sharp contrast to both neutral and westerly intraseasonal events. Statistically significant differences in the generation and conversion of PAPE between westerly and easterly intraseasonal events exist near 10°N, 100°W and the exit region of the Papagayo jet near 8°N, 87°W.

## 2.5 Perturbation Kinetic Energy Budget

To investigate the statistically significant differences of total PKE between westerly and easterly intraseasonal events, the dominant terms of the PKE budget are analyzed using the formulation derived by Lau and Lau (1992). This budget is similar to that also utilized by Maloney and Hartmann (2001) to examine the PKE budget of EPAC EWs as a function of intraseasonal phase at the 850 hPa pressure level. In this study, we are calculating the vertically averaged budget as a function of intraseasonal phase. Previous studies have shown leading contributions from barotropic energy conversions due to strong modulation of low-level zonal winds by EPAC intraseasonal variability and

from PAPE conversions that result from latent heating by convection (Maloney and Hartmann 2001, Serra et al. 2008, Serra et al. 2010). The PKE budget is written as:

$$\frac{\partial K'}{\partial t} = -\overline{V_h'(V'\cdot\nabla)\overline{V}_h} - \overline{V}\cdot\nabla K' - \overline{V'\cdot\nabla K'} - R\left(\overline{\omega'T'}\right)/p - \nabla\cdot\left(\overline{V'\Phi'}\right) + D \qquad (2)$$

where $\Phi$ is the geopotential. The first term on the right side of equation (2), $-\overline{V_h'(V'\cdot\nabla)\overline{V}_h}$, represents the barotropic conversion of PKE from the mean kinetic energy. The second and third terms, $-\overline{V}\cdot\nabla K' - \overline{V'\cdot\nabla K'}$, represent the advection of PKE by the background and perturbation wind field, respectively. The fourth term, $-R\left(\overline{\omega'T'}\right)/p$, represents the conversion of PAPE to PKE through the negative correlation of perturbation pressure velocity and temperature, which is a process also contained in the PAPE budget. The fifth term, $-\nabla\cdot\left(\overline{V'\Phi'}\right)$, represents the rearrangement of PKE by geopotential flux convergence. The last term, *D*, is not calculated in our budget but represents the dissipation of PKE by friction, subgrid-scale effects, and any residual in the budget. Terms are vertically averaged from 1000 hPa to 200 hPa.

To establish a baseline for examining the PKE budgets during westerly and easterly intraseasonal events, we first examine the budget during neutral intraseasonal periods. The dominant terms of the PKE budget during neutral periods are shown in Figure 2.6. The largest sources of PKE are the barotropic conversion and PAPE to PKE conversion (Figure 2.6a,b). Positive values of the barotropic conversion term are located along a strip extending west-northwest from Nicaragua, just a couple of degrees north of the ITCZ (see Figure 2.12a). The EPAC warm pool barotropic conversion maximum is located east of 115°W with values ranging from 2-3*10⁻⁵ (m²s⁻²)s⁻¹ and generally lies along the path of composite EWs during neutral periods (see Figure 2.1).

The positive barotropic conversion region located in the southwest Caribbean is an interesting feature that lies on the cyclonic shear side of the Caribbean low-level jet between the South and Central American landmasses. The largest positive conversion from PAPE in the EPAC is located near the Panama Bight and extends west-northwest along the ITCZ. A secondary maximum is located near 10°N, 105°W with values between $3\text{-}6*10^{-5}$ $(m^2s^{-2})s^{-1}$. Similar to the barotropic conversion, the largest positive PAPE conversion values are located east of 115°W. Terms not shown include the advection of PKE by the mean and perturbation winds as they are generally small, suggesting that most redistribution of PKE is performed by the geopotential flux convergence (Figure 2.6c). The residual of the PKE budget during neutral periods is of a comparable order of magnitude to the leading terms of the budget (Figure 2.6d). PKE sinks, such as friction in the boundary layer, are likely a substantial contribution to this term (e.g. Lau and Lau 1992).

For westerly intraseasonal events, the PKE sources, the barotropic conversion and PAPE to PKE conversion, are enhanced (Figure 2.7a,b) compared to those during neutral periods and easterly intraseasonal events (see Figure 2.8). Regions where values are significantly different at the 95% confidence level during westerly intraseasonal events compared to easterly intraseasonal events are stippled. The barotropic conversion in the EPAC maximizes near 12°N, 103°W with values ranging from $3\text{-}5*10^{-5}$ $(m^2s^{-2})s^{-1}$, very near the maximum of PAPE generation by $\gamma(\overline{Q_1 {}'T{}'})/\overline{T}$ (see Figure 2.5c). This maximum of barotropic conversion is significantly different from that during easterly intraseasonal events. A local maximum of the barotropic conversion

# PKE Composite Terms (Neutral)
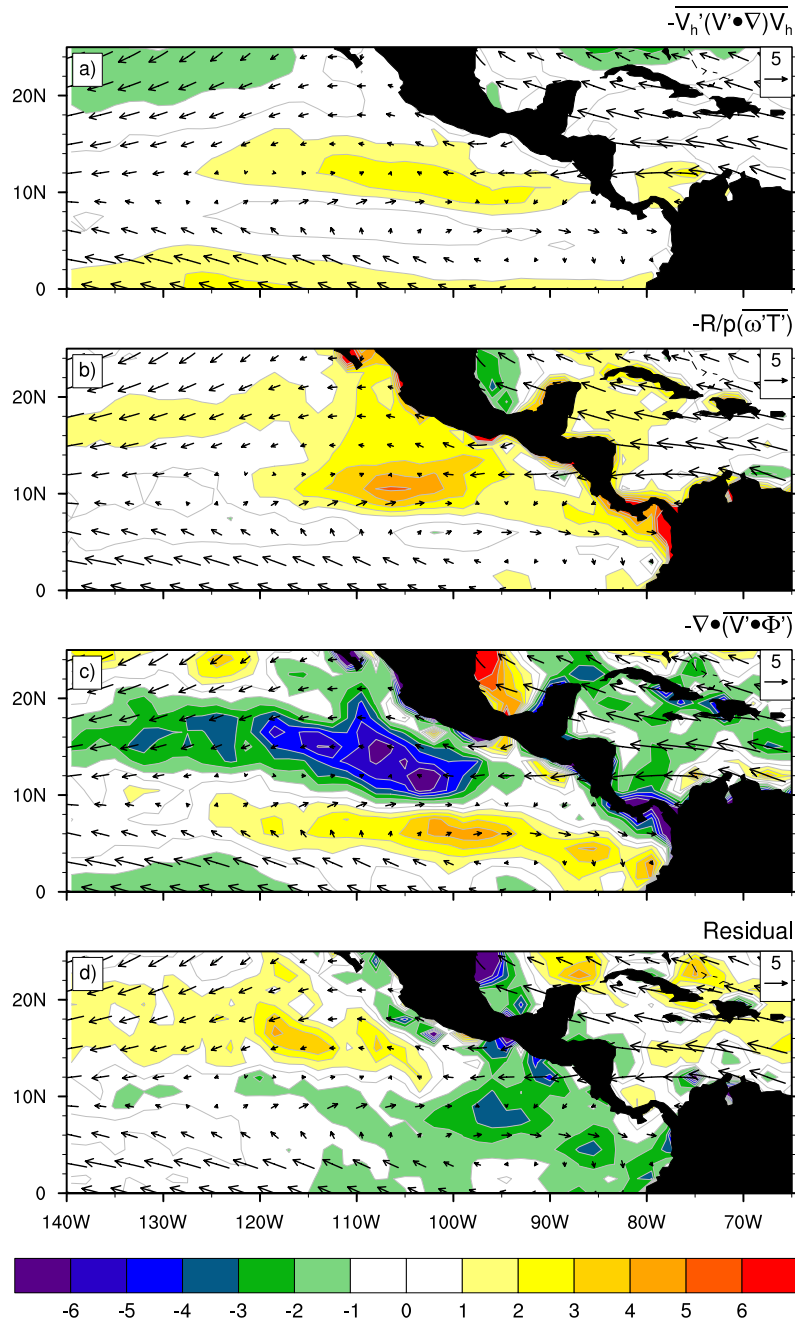


Fig. 2.6 Composites of vertically averaged a) barotropic conversion, b) PAPE to PKE conversion, c) geopotential flux convergence, and d) residual of the perturbation kinetic energy budget over neutral intraseasonal periods. Values are $*10^{-5}$ $(m^2s^{-2})s^{-1}$. Composite total winds at 850 hPa with tropical cyclone anomalies removed are shown for neutral intraseasonal periods. The reference vector is located in the upper right of each panel.

# PKE Composite Terms (Westerly)



Fig. 2.7 Same as Fig. 2.6, except for westerly intraseasonal events. Stipling in a), b), and c) indicates significantly different areas between westerly and easterly intraseasonal events at the 95% confidence level.

is also present in the southwestern Caribbean. The generation of PKE from the conversion of PAPE has two local maxima, one near the Panama Bight ($4\text{-}11*10^{-5}$ $(m^2s^{-2})s^{-1}$) and another near 11°N, 101°W ($3\text{-}6*10^{-5}$ $(m^2s^{-2})s^{-1}$) (Figure 2.7b). Reduced values are located between the m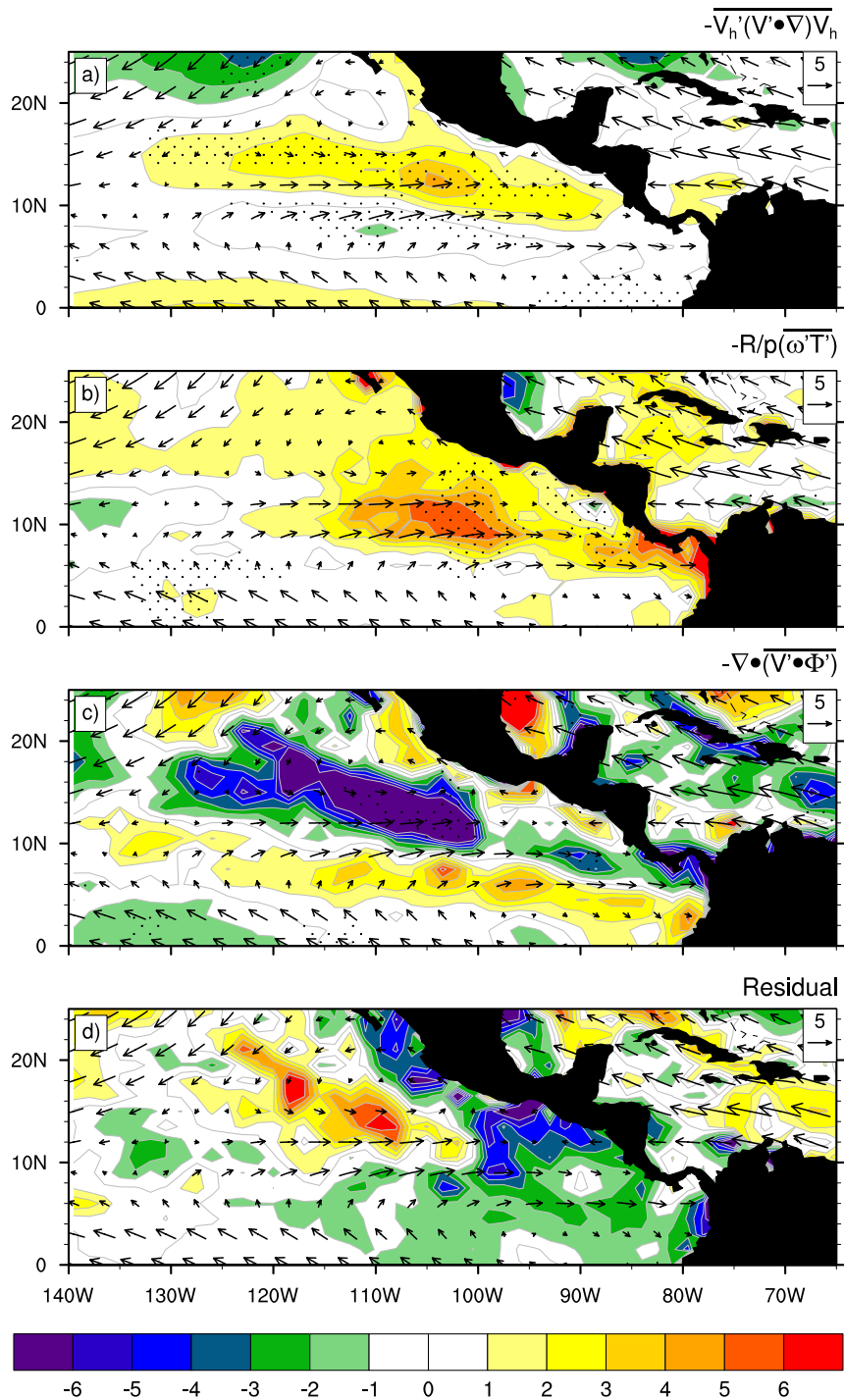axima near the Costa Rica Dome. Geopotential flux convergence is strongly negative during westerly intraseasonal events extending semi-continuously from the Panama Bight to the northwest (Figure 2.7c). The term has a maximum contribution near the regions of strongest PAPE generation by $\gamma(\overline{Q_1'T'})/\overline{T}$.

Compared to neutral and westerly intraseasonal events, easterly intraseasonal events are characterized by weaker PKE sources (Figure 2.8). The barotropic generation of PKE is weaker than during westerly intraseasonal events and much narrower meridionally. Further, the strongest barotropic conversions are shifted southward. Barotropic conversions extend zonally from the southwestern Caribbean and across the EPAC, maximizing near 10°N, 105°W (Figure 2.8a). Notable conversions of PAPE to PKE along this path are only located near the Panama Bight and west of 105°W (Figure 2.8b). Negative geopotential flux convergence values are located near regions of strong PAPE to PKE conversion (Figure 2.8c). Thus, barotropic conversion is weaker over the life cycle of EWs during easterly intraseasonal events, but plays a larger fractional role in EW growth. Convection is generally suppressed during easterly intraseasonal events and may contribute to a suppression of convection associated with EWs (e.g. Maloney and Esbensen 2007). The southward shift of composite EWs track during easterly intraseasonal events (see Figure 2.3) compared to westerly intraseasonal events (see Figure 2.2) is perhaps related to the southward shift of a leading PKE source term, the barotropic conversion. Like neutral periods and
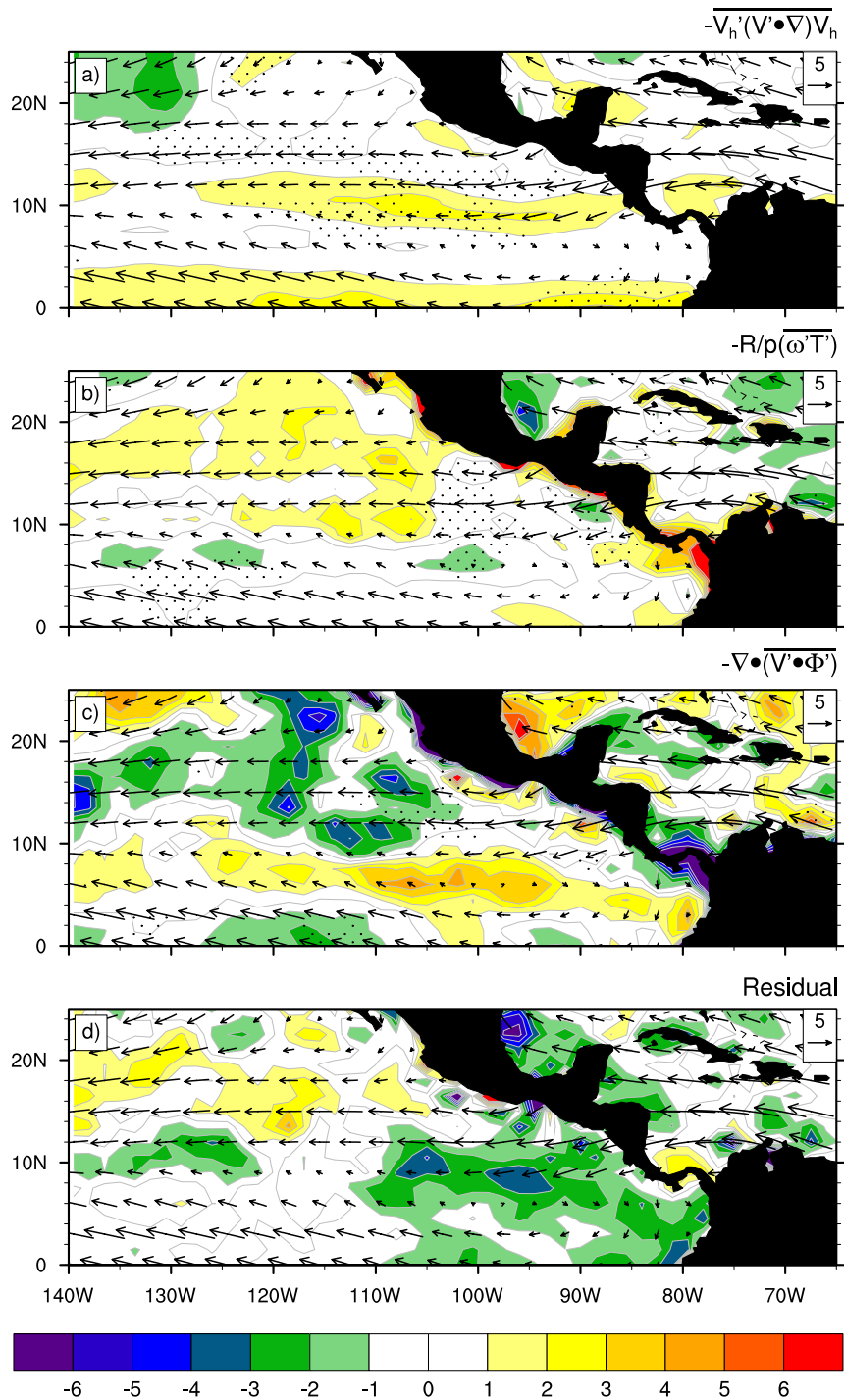
# PKE Composite Terms (Easterly)



Fig. 2.8 Same as Fig. 2.6 and 2.7, except for easterly intraseasonal events. Stipling in a), b), and c) indicates significantly different areas between westerly and easterly intraseasonal events at the 95% confidence level.

westerly intraseasonal events, the residual of the PKE budget during easterly intraseasonal events is of the same order of magnitude as the leading terms (Figure 2.8d).

## 2.6 Vertical Structure

This section investigates the vertical structure of the barotropic conversion in the PKE budget. By examining cross-sections along the paths of EWs we are able to better understand the horizontal and vertical locations of the barotropic conversion that assists in the maintenance and development of EWs as they propagate westward during different intraseasonal background states.

Barotropic conversions in the EPAC have been shown to strongly vary at low levels as a function of intraseasonal phase (Maloney and Hartmann 2001). Forced Kelvin waves in response to strong MJO convective heating anomalies in the Eastern hemisphere propagate rapidly across the central Pacific producing strong upper and lower level zonal wind anomalies along the equator (Rydbeck et al. 2013). The zonal wind anomalies are also enhanced by synchronized local intraseasonal convective variability. The zonal wind fluctuations are evident in the total 850 hPa wind fields previously shown (Figures 2.4, 2.6, 2.7, and 2.8). Because EWs typically have their most robust dynamical features in the mid to low levels, the strong change in background state of the low and middle troposphere resulting from EPAC intraseasonal variability would seem to have the largest impact on barotropic conversions. We will show that while strong changes of the barotropic conversions do occur at low levels, the largest changes occur at midlevels where the flow is strongly forced by intraseasonal diabatic heating.

The barotropic conversion term of the PKE budget can be separated into three dominant terms: $-\overline{u'v'}\partial\overline{u}/\partial y$, $-\overline{u'v'}\partial\overline{v}/\partial x$, and $-\overline{u'^2}\partial\overline{u}/\partial x - \overline{v'^2}\partial\overline{v}/\partial y$. We assume barotropic terms involving vertical shear of the mean horizontal wind are small, similar to Maloney and Hartmann 2001. The first term represents the extraction of energy from the meridional shear of the mean zonal wind by the EW. The second term represents the extraction of energy from the zonal shear of the mean meridional wind by the EW. The third term is referred to as the net barotropic convergence, shown as a summation of the zonal and meridional convergence terms. These terms often compensate for one another by shrinking and stretching along axes of contraction and dilatation.

Figure 2.9 shows the cross-section of the total barotropic conversion term and leading contributing terms to the total barotropic conversion term along the northwesterly track of EWs during neutral intraseasonal periods. The track along which all cross-sections are analyzed is shown in Figure 2.4a. These cross-sections are averaged over a 1.5° width. The term involving the zonal shear of the meridional wind, $-\overline{u'v'}\partial\overline{v}/\partial x$, weakly contributes to the total barotropic conversion term and is not shown. The total barotropic conversion maximizes just above the surface between 12.75°N, 104°W - 8.25°N, 86.75°W (Figure 2.9a). Generally, the strongest values are confined below 700 hPa with the exception of an upward extension of large positive values to midlevels near 12.75°N, 104°W. The term involving the meridional shear of the mean zonal wind, $-\overline{u'v'}\partial\overline{u}/\partial y$, is shown in Figure 2.9b. Easterly waves with southwest to northeast tilts extract energy from the meridional shear of the mean zonal wind. This term has local maxima at 850 hPa near 9.75°N, 92.5°W and 600 hPa between 14.25°N, 109.75°W - 12.75°N, 104°W (Figure 2.9b). The midlevel maximum is approximately
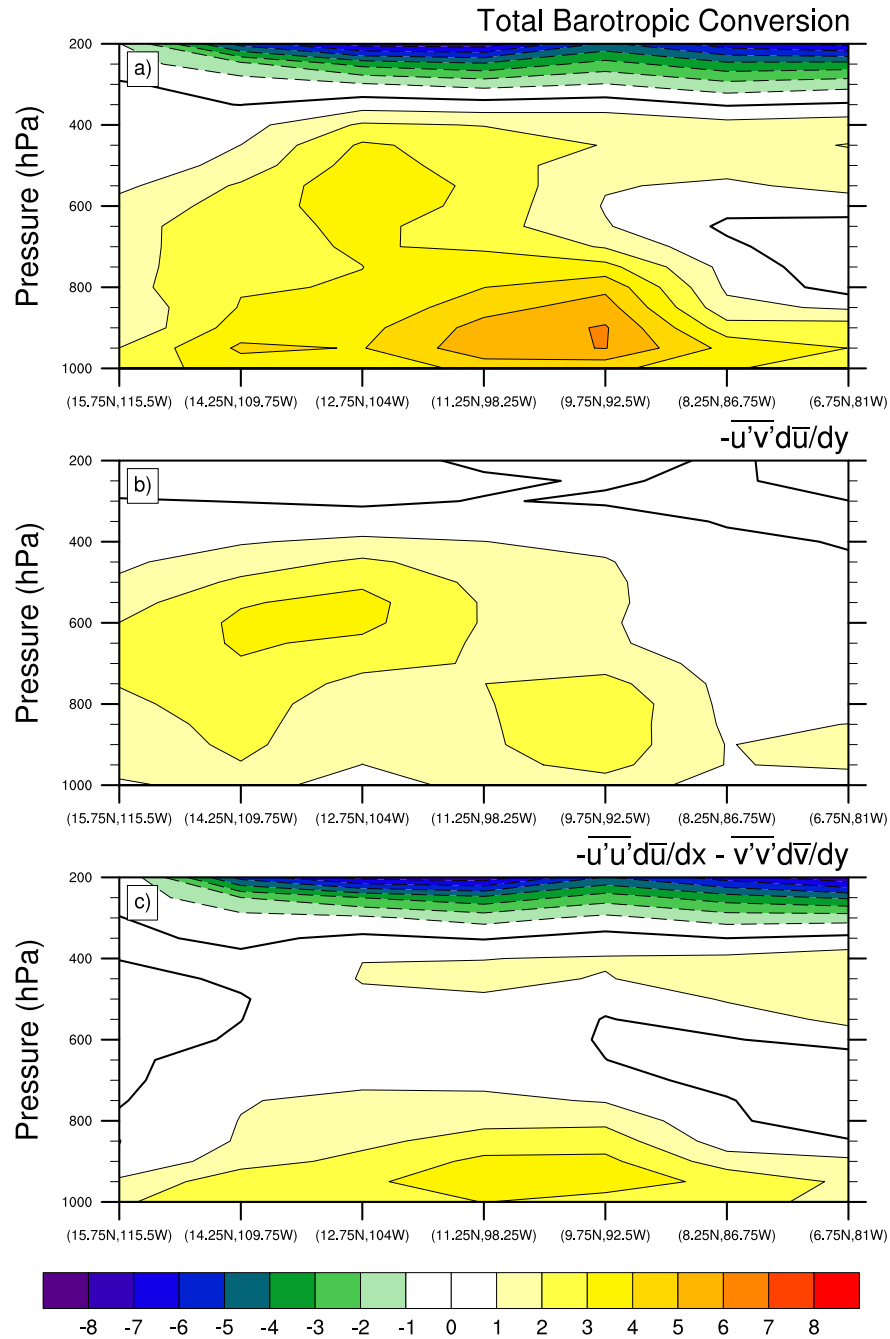
Fig. 2.9 Composite cross-sections from the northwest to the southeast averaged over a 1.5° width of a) total barotropic conversion, b) $-\overline{u'v'}\partial\overline{u}/\partial y$, and c) $-\overline{u'^2}\partial\overline{u}/\partial x - \overline{v'^2}\partial\overline{v}/\partial y$ for neutral intraseasonal periods. Positive (negative) line contours are solid (dashed). The thick solid line is the zero contour. Units are $*10^{-5}$ $(m^2s^{-2})s^{-1}$.

25% larger than the low-level maximum with values greater than $3*10^{-5}$ $(m^2s^{-2})s^{-1}$. The net barotropic convergence, $-\overline{u'^2}\partial\overline{u}/\partial x - \overline{v'^2}\partial\overline{v}/\partial y$, maximizes just above the surface and below 700 hPa (Figure 2.9c) with values equivalent to $-\overline{u'v'}\partial\overline{u}/\partial y$. The maximum of net barotropic convergence is collocated with the maximum in the total barotropic conversion (Figure 2.9a,c).

Figure 2.10 shows a similar cross-section of the total barotropic conversion term and leading contributors during westerly intraseasonal events. Compared to neutral intraseasonal periods, total barotropic conversions during westerly intraseasonal events are generally enhanced along the same cross section (Figure 2.10a). The maximum between 700 hPa - 500 hPa near 12.75°N, 104°W is increased in magnitude by approximately 50%. This region is also close to the latitude and longitude of the maxima of vertically averaged generation of PAPE by perturbation diabatic heating, $\gamma(\overline{Q_1'T'})/\overline{T}$ (see Figure 2.5c). Low-level total barotropic conversions are increased by approximately 40% in the northwestern region of the cross section near 14.25°N, 109.75°W. Figure 2.10b,c shows the leading contributors to the total barotropic energy conversion term. Barotropic conversions by eddies acting on the meridional shear of the mean zonal wind, $-\overline{u'v'}\partial\overline{u}/\partial y$, are shown in Figure 2.10b. The conversions generally maximize in the mid-troposphere between 500 hPa -700 hPa with values exceeding $5*10^{-5}$ $(m^2s^{-2})s^{-1}$ and are located mostly in the northwestern half of the cross-section. This result contrasts with the results of previous studies where $-\overline{u'v'}\partial\overline{u}/\partial y$ was assumed to maximize at low levels during westerly intraseasonal events (e.g. Maloney and Hartmann 2001). A secondary maximum that is slightly increased from neutral periods is centered near 9.75°N, 92.5°W at 800 hPa and is approximately half the magnitude of
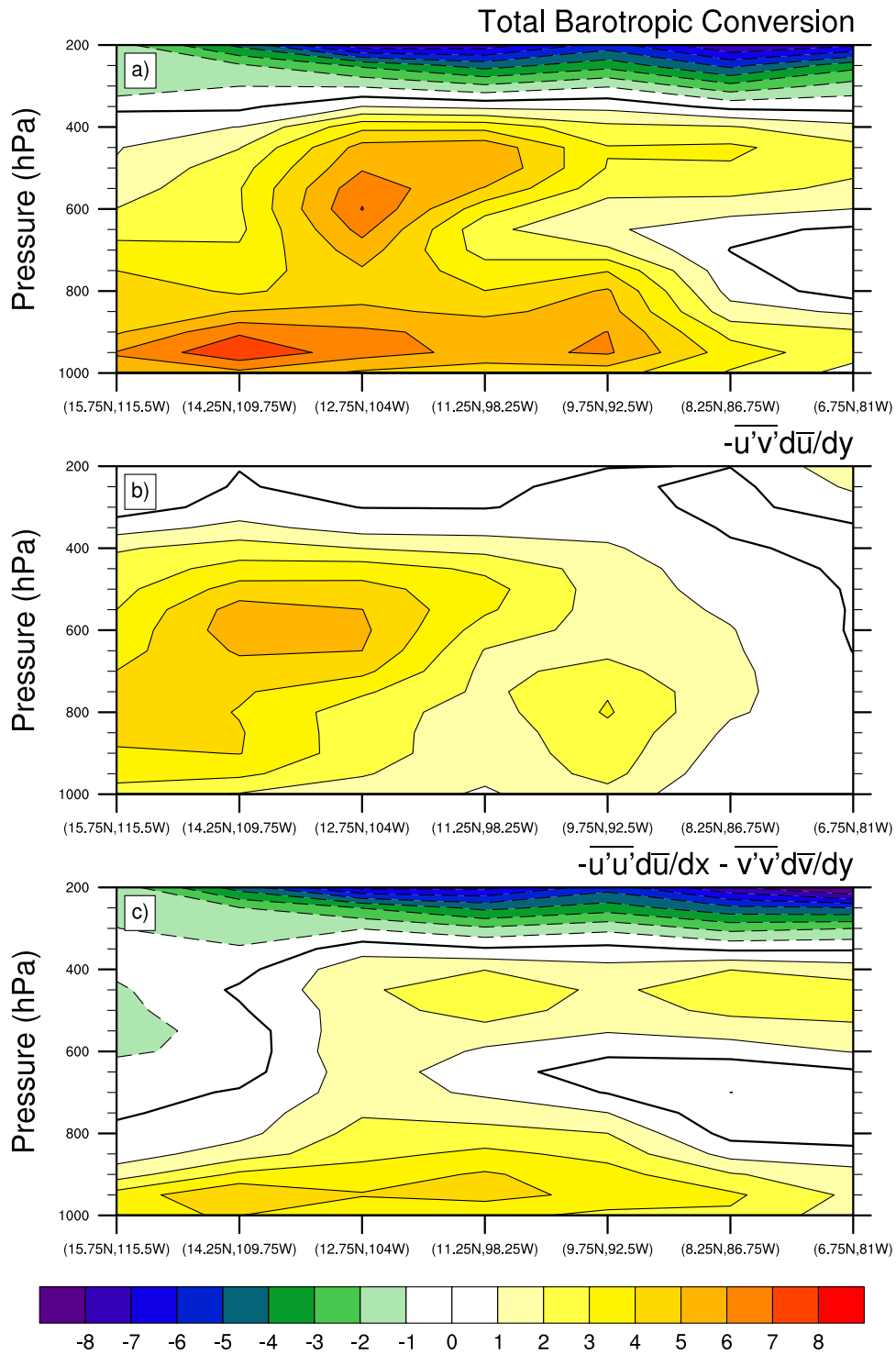
Fig. 2.10 Same as Fig 2.9, except for westerly intraseasonal events.

the midlevel maximum. Compared to the net barotropic convergence during neutral periods, the net barotropic convergence during westerly intraseasonal events is increased (Figure 2.10c). The strongest net barotropic convergence occurs just above the surface and is confined below 700 hPa. Secondary maxima are located between 400 - 500 hPa. Large negative PKE budget residual values (e.g. as in Figure 2.7d) in the low-levels (not shown) suggest that frictional dissipation is countering the effects of positive eddy kinetic energy tendency associated with net barotropic convergence in the boundary layer. Conversions by $-\overline{u'v'}\partial \overline{v}/\partial x$ are generally an order of magnitude smaller, except near 15°N, 109.75°W where weak negative values are present in the low to mid-troposphere (not shown).

Figure 2.11 shows a cross-section of the total barotropic conversion term and leading contributors during easterly intraseasonal events. The total barotropic conversion term maximizes below 700 hPa, near 9.75°N, 92.5°W (Figure 2.11a). Barotropic conversions due to $-\overline{u'v'}\partial \overline{u}/\partial y$ are shown in Figure 2.11b. Such conversions maximize in the same region as the total barotropic conversion below 700 hPa. Unlike westerly intraseasonal events, barotropic conversions due to $-\overline{u'v'}\partial \overline{u}/\partial y$ during easterly intraseasonal events are small at midlevels. The net barotropic convergence is greatest below 800 hPa and is of comparable magnitude to $-\overline{u'v'}\partial \overline{u}/\partial y$ (Figure 2.11c). Thus, easterly intraseasonal events have reduced barotropic conversions along the composite EW track with notable reductions in the midlevel barotropic conversion compared to westerly intraseasonal events. Because strong barotropic conversions are shifted southward during easterly intraseasonal events, we are not sampling the strongest barotropic conversions, but only those conversions that lie along the cross-section

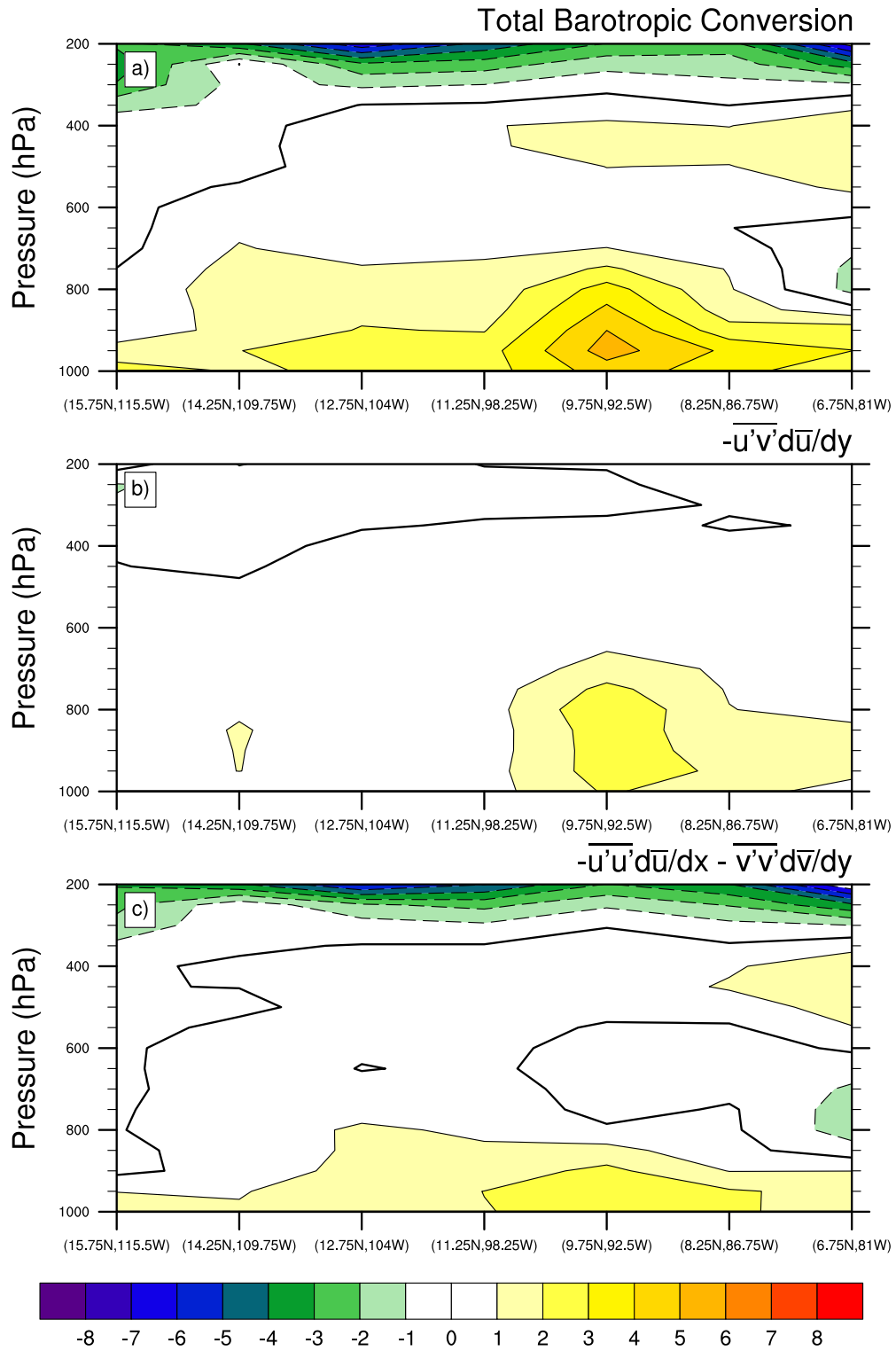# Barotropic Conversion Composites (Easterly)



Fig. 2.11 Same as Figs. 2.9 and 2.10, except for easterly intraseasonal events.

shown in Figure 2.4a. To note, cross-sections along the vertically averaged barotropic conversion maximum during easterly intraseasonal events show strong low-level barotropic conversions west of 105°W, primarily resulting from enhanced net barotropic convergence (not shown).

The strong barotropic conversion in the mid troposphere during westerly intraseasonal events is an interesting and previously unidentified feature of the EPAC PKE budget. The midlevel maximum is primarily caused by $-\overline{u'v'}\partial\overline{u}/\partial y$. This term is a function of the perturbation wind magnitude and the meridional shear of the mean zonal wind. Such conversions have previously only been shown in the low levels where strong zonal wind anomalies associated with EPAC intraseasonal variability occur (Maloney and Hartmann 2001). To further explore the midlevel barotropic conversion component present during neutral and westerly intraseasonal events but absent during easterly intraseasonal events, we examine maps of mean OLR, mean wind at 550 hPa, and meridional shear of the mean zonal wind, $\partial\overline{u}/\partial y$, at 550 hPa during neutral, westerly, and easterly intraseasonal events, respectively (Figure 2.12). During neutral periods, 550 hPa cyclonic shear extends from the northwest corner of South America across Nicaragua and into the EPAC, poleward of the ITCZ (Figure 2.12a). The shear maximizes in the east pacific warm pool near 11°N, 100°W. For westerly events, the shear is slightly shifted to the northwest and is wider latitudinally (Figure 2.12b). For Figure 2.12b, the OLR is shown as a difference from neutral periods ($OLR_{westerly} - OLR_{neutral}$). The maximum shear during westerly intraseasonal events is enhanced by approximately 20% in regions of reduced OLR. The enhanced cyclonic shear zone is caused by strongly reduced easterlies in regions south of enhanced convection.

## 550 hPa Mean Wind and Meridional Shear
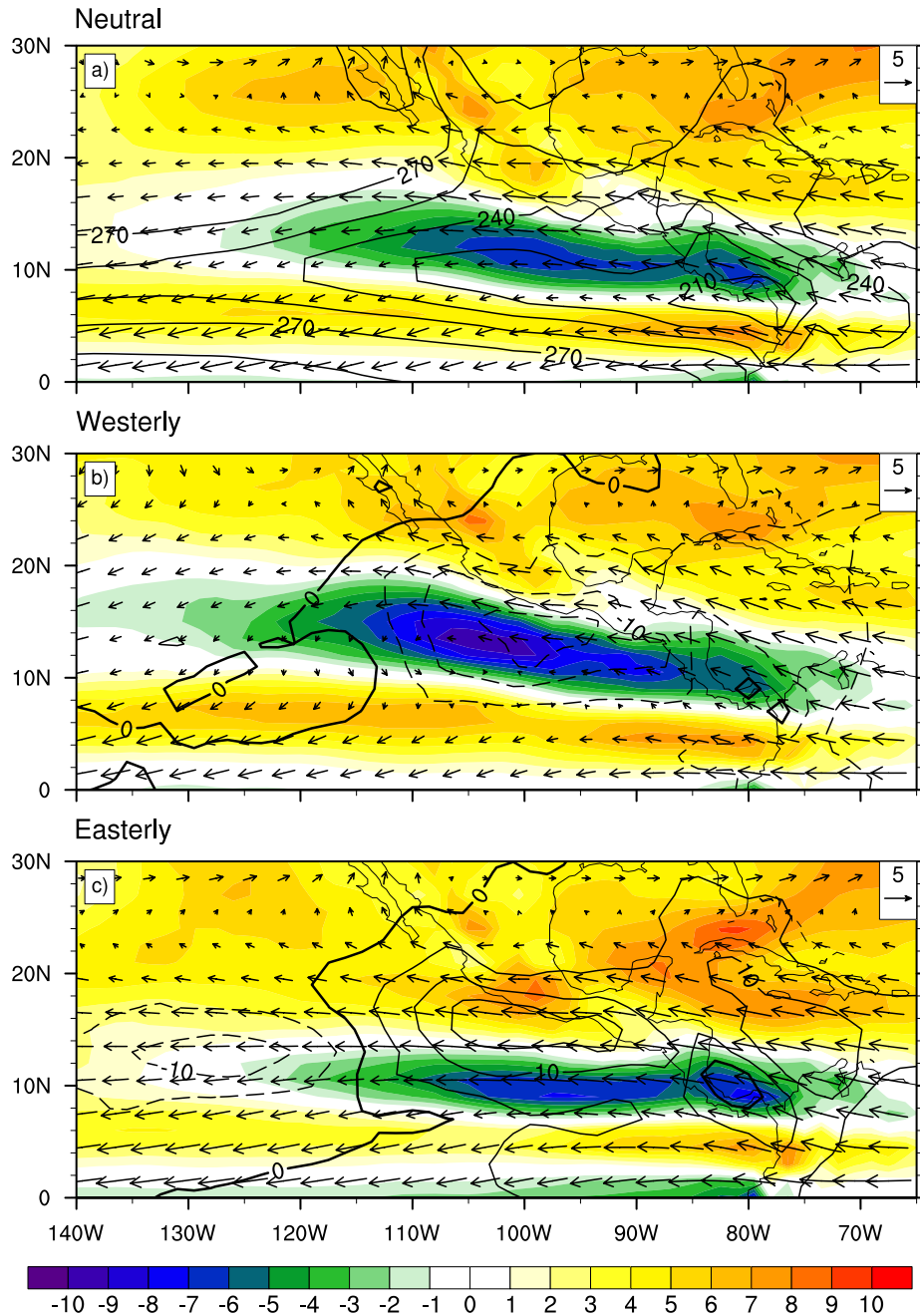


Fig. 2.12 For a) composite of 550 hPa mean wind (m/s, vectors), mean OLR (Wm$^{-2}$, line contours), and $\partial\overline{u}/\partial y$ (*10$^{-6}$ s$^{-1}$, color contours) for neutral intraseasonal periods. For b) westerly and c) easterly intraseasonal events, same as a) except OLR is shown as a difference from neutral periods ($OLR_{westerly/easterly}$ – $OLR_{neutral}$). OLR contour interval is 15 Wm$^{-2}$ for a) and 5 Wm$^{-2}$ for b) and c). Negative contours are dashed. Reference vector is located in the upper right of each panel.

Although stronger eddies during this period may also enhance $-\overline{u'v'}\partial\overline{u}/\partial y$, the cyclonic shear of the zonal wind at mid levels favorably contributes to increases in PKE. During easterly events, the cyclonic shear region is narrower, shifted south, and oriented more zonally than during neutral periods, although of comparable magnitude even though mean OLR is increased (Figure 2.12c).

Compared to neutral intraseasonal periods, the region of strongest reduction in mean midlevel zonal wind magnitudes during westerly intraseasonal events is of similar structure to the leading EOF of 850 hPa zonal wind in the east pacific used to identify intraseasonal events in this study (see also Maloney and Hartmann 2001). Intraseasonal variability strongly modulates convective patterns in the EPAC that in turn modify the local circulation. At a particular vertical level without strong frictional contributions and characterized by positive absolute vorticity, convective patterns that drive net mass convergence in the horizontal act to increase the vorticity (Haynes and McIntyre 1987). During westerly intraseasonal events, increased convergence at midlevels resulting from enhanced diabatic heating would intensify the background cyclonic vorticity. When comparing the mean 550 hPa winds during neutral periods and westerly intraseasonal events (Figure 2.12a, b), the largest decrease in easterlies occurs just south of the negative OLR anomaly, suggesting vorticity convergence driven by enhanced diabatic heating is responsible for the increased barotropic conversion at midlevels during westerly intraseasonal events.

To explore the possible connection between background diabatic heating during intraseasonal events and modulation of the background midlevel circulation in the EPAC, a vertical cross-section of $\overline{Q_1}$ and $\partial\overline{\omega}/\partial p$ is shown in Figure 2.13a for neutral

periods. By mass continuity, $\partial\overline{\omega}/\partial p$ represents mean horizontal convergence. Figure 2.13b,c shows vertical cross-sections of $\overline{Q_1}$ and differences of $\partial\overline{\omega}/\partial p$ from neutral periods for westerly and easterly intraseasonal events, $\partial\overline{\omega}/\partial p_{westerly/easterly}$ - $\partial\overline{\omega}/\partial p_{neutral}$, respectively. Positive (negative) differences represent increased (reduced) convergence. Neutral periods have maximum values of $\overline{Q_1}$ between 110-120 $(m^2s^{-2})s^{-1}$ near 11°N, 98.25°W between 600 hPa – 400 hPa. $\partial\overline{\omega}/\partial p$ maximizes in regions of strong vertical gradients of $\overline{Q_1}$, which in the free troposphere occur above 700 hPa. During westerly intraseasonal events, patterns of $\overline{Q_1}$ are strengthened compared to neutral periods (Figure 2.13b). Positive $\partial\overline{\omega}/\partial p$ values in much of the middle troposphere between 700 hPa - 400 hPa are also strengthened, presumably enhancing vorticity convergence and thus cyclonic vorticity. Negative $\partial\overline{\omega}/\partial p$ values strengthen above 400 hPa. For easterly intraseasonal events, the $\overline{Q_1}$ maximum at midlevels near 11°N, 98.25°W is 80-100 $(m^2s^{-2})s^{-1}$ compared to 140 – 150 $(m^2s^{-2})s^{-1}$ during westerly intraseasonal events (Figure 2.13c). Positive $\partial\overline{\omega}/\partial p$ values are notably reduced during easterly intraseasonal events compared to neutral periods through the majority of the middle and lower troposphere, reducing vorticity convergence and cyclonic vorticity.

Our results suggest that the mean winds at midlevels are strongly modulated by the vertical distribution of $\overline{Q_1}$ such that the local mean midlevel circulation pattern is modulated, affecting the meridional shear of the mean zonal wind. During westerly intraseasonal events, the mean diabatic heating and vertical velocity profiles are more

38
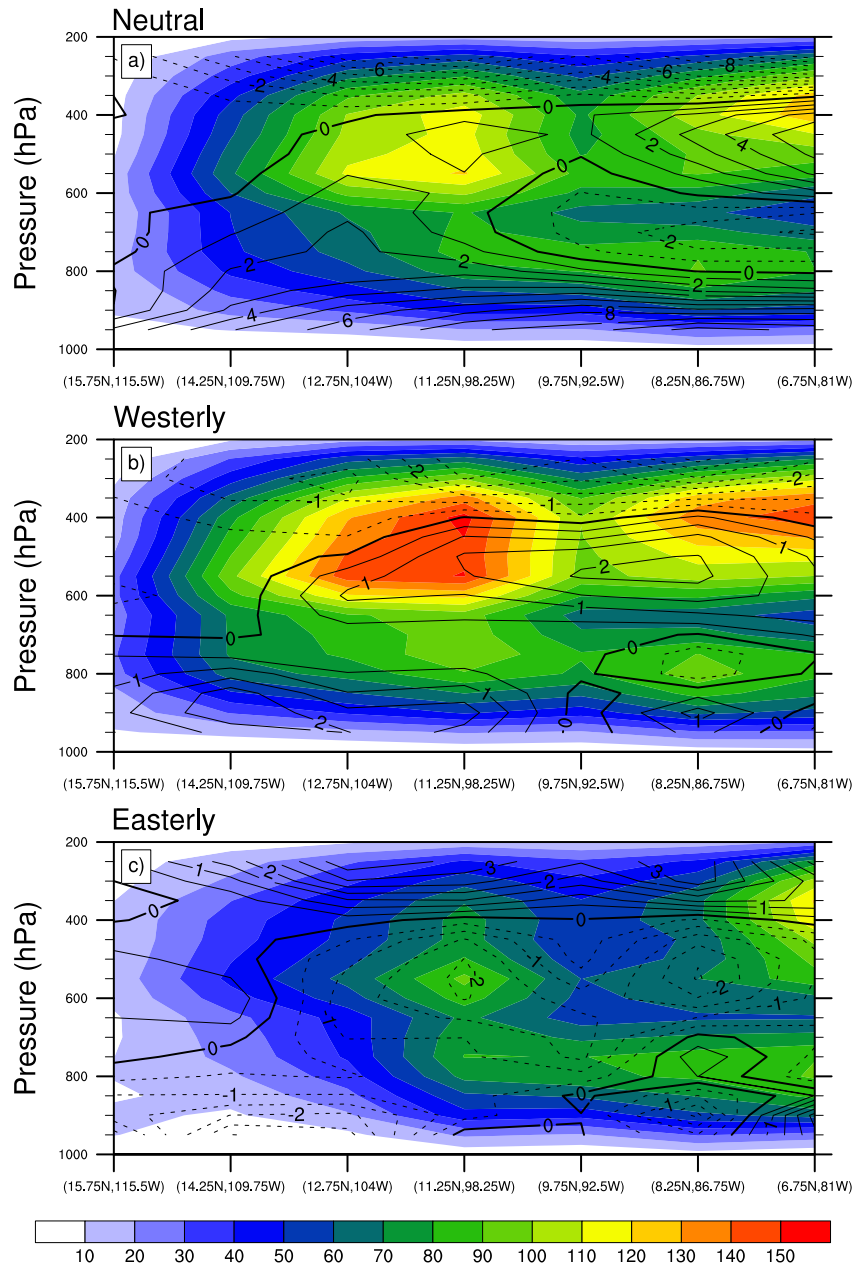
Fig. 2.13 For a) composite cross-section from the northwest to the southeast averaged over a 1.5° width of $\overline{Q_1}$ (($m^2s^{-2}$)$s^{-1}$, color contours) and $\partial\overline{\omega}/\partial p$ (*$10^{-6}$ $s^{-1}$, line contours) during neutral periods. $\partial\overline{\omega}/\partial p$ is contoured every 1*$10^{-6}$ $s^{-1}$. For b) westerly and c) easterly intraseasonal events, same as a) except $\partial\overline{\omega}/\partial p$ is shown as a difference from neutral periods ($\partial\overline{\omega}_{westerly/easterly}/\partial p$ - $\partial\overline{\omega}_{neutral}/\partial p$). $\partial\overline{\omega}/\partial p$ is contoured every 0.5*$10^{-6}$ $s^{-1}$. Negative contours are dashed.

top-heavy with positive anomalous heating and vertical velocity gradients above 700 hPa, enhancing positive vorticity convergence. Mid tropospheric vertical velocity gradients are weakened during easterly intraseasonal events, generating anomalous negative vorticity.

## 2.7 Discussion and Conclusions

The mechanism, magnitude, location, and vertical structure of EPAC EW energetics strongly vary on intraseasonal timescales. The EPAC exhibits significant intraseasonal variability during boreal summer marked by strong variations of low-level zonal winds and convection. Westerly (easterly) low-level wind anomalies are generally associated with enhanced (suppressed) convection in the EPAC warm pool. Such intraseasonal anomalies strongly affect the background state on which EWs develop and are maintained. To quantify the role of EPAC intraseasonal variability on the energetics of EPAC EWs, PAPE and PKE budgets are calculated for vigorous EWs occurring during neutral, westerly, and easterly intraseasonal events.

The generation of PAPE during neutral periods and westerly intraseasonal events is dominated by the correlation of perturbation diabatic heating and temperature. This source of PAPE is almost entirely balanced by the conversion of PAPE to PKE. The conversion PAPE to PKE is enhanced by approximately 25% during westerly intraseasonal events compared to neutral periods. Generation of PAPE during easterly intraseasonal events is significantly weaker than during westerly intraseasonal events over much of the composite EW track. Sources of PAPE due to baroclinic conversions of mean available potential energy to PAPE do not strongly contribute to the budget, suggesting that strong land-sea temperature differences along the North and South

American coasts are not of first-order importance to EW growth or decay, unlike in the west African monsoon region (e.g. Hsieh and Cook 2005).

A novel result of this study is the detection of strong PKE generation by barotropic conversion at midlevels during westerly intraseasonal events. Previous studies assumed that the strongest variations in barotropic conversion occurred in the lower troposphere (e.g. Maloney and Hartmann 2001). However, our results suggest that equally strong barotropic conversion occurs in the midlevels during westerly intraseasonal events. The source of the midlevel barotropic conversion is in part due to the strong intraseasonal modulation of midlevel mean zonal winds. We hypothesize that increased vorticity convergence caused by enhanced diabatic heating gradients at midlevels during westerly intraseasonal events modifies the midlevel mean winds such that mean cyclonic shear is enhanced. These results provide insight into the possible growth and transition of midlevel vortices associated with mesoscale convective systems into EWs capable of seeding tropical cyclones (Bister and Emanuel 1997, Raymond et al. 1998, Raymond et al. 2013). We are currently investigating the origins of such pre-existing midlevel and low-level vortices that develop into EWs in the EPAC. Interestingly, fig. 13 suggests that the shallow meridional circulation of Zhang et al. (2004) is not modulated on intraseasonal timescales, only the deep overturning circulation.

The energetic analysis presented supports previous suggestions that EWs capable of seeding tropical cyclones are able develop entirely locally in the EPAC. The vertically averaged total PKE maxima are divided by the sum of the leading vertically averaged terms of the PKE budget, the conversion of PAPE to PKE and barotropic

conversion, to determine a reasonable EW growth timescale. The EPAC supports the development of a trivial disturbance to a robust EW in approximately 1.5 – 2.5 days, confirming similar conclusions made by Maloney and Hartmann (2000). Easterly wave energy sources and sinks during westerly intraseasonal events are seen as an amplification of the patterns observed during neutral periods. In particular, barotropic conversions are preferentially enhanced in the middle troposphere. Easterly waves during easterly intraseasonal events are almost entirely dependent on barotropic conversions for their growth, whereas waves during westerly intraseasonal events are supported by conversions of PAPE to PKE and barotropic conversions. These results contrast with those performed by Serra et al. (2010), which suggest that EW activity and tropical cyclogenesis are enhanced during periods when the Caribbean low-level jet is strongest. The Caribbean low-level jet is enhanced during easterly intraseasonal events in our study but is associated with decreased total PKE in the EPAC. We plan to further investigate the interactions of EWs and intraseasonal variability with local orography and terrain-induced mesoscale convective systems through the use of a regional model.

**CHAPTER 3 On the Convective Coupling and Moisture Organization of East Pacific Easterly Waves[2]**

## 3.1 Background

East Pacific (EPAC) easterly waves (EWs) are off-equatorial convectively coupled phenomena that occur during boreal summer. EWs provide a majority of the tropical convective variance at timescales less than 10 days (Kiladis et al. 2006), are associated with 25-40% of deep convective clouds in the ITCZ (Tai and Ogura 1987, Gu and Zhang 2002), and seed the majority of EPAC tropical cyclones (e.g. Avila and Guinney 2000, Avila et al. 2003, Pasch et al. 2009). East Pacific EWs are energized from the latent heat release associated with convection and by extracting kinetic energy from the background flow (Tai and Ogura 1987, Maloney and Hartmann 2001, Hartmann and Maloney 2001, Serra et al. 2008, Aiyyer and Molinari 2008; Serra et al. 2010, Rydbeck and Maloney 2014, Hoover et al. 2014). In this study, we show that convection within the EW is also able to modulate the horizontal orientation of an EW's circulation in addition to its intensity.

The orientation, or tilt, of the EW is critical to the barotropic conversion of mean kinetic energy to perturbation kinetic energy. In the presence of cyclonic shear of the mean zonal wind, as typically occurs in the EPAC warm pool, EWs are energized if the wave's horizontal flow field is elongated along a diagonal from the southwest (SW) to the northeast (NE). Such EWs produce a downgradient momentum flux in the presence of cyclonic shear of the mean zonal wind associated with eddy growth at the expense of

---

the mean flow. The barotropic conversion term in the perturbation kinetic energy budget of EWs responsible for this process is $-\overline{u'v'}\,\partial\overline{u}/\partial y$ (Rydbeck and Maloney 2014). In this study, we explore the role of convection in producing the observed SW to NE horizontal tilt of EWs in the EPAC.

Since the discovery of EWs, different conceptual models of the wave's convection and circulation have been hypothesized (e.g. Dunn 1940; Riehl 1945, 1948, 1954; Palmer 1952; Malkus and Riehl 1964). In particular, many analyses have suggested various phasing of convection with regard to the wave axis. We briefly summarize three leading conceptual models of EW phasings: the Caribbean, the Atlantic, and the African wave model.

The Caribbean wave model, often referred to as Riehl's classical EW model, was derived from 4-times daily atmospheric soundings over Puerto Rico and visual observations (Riehl 1945, 1948, 1954). Riehl's work built on findings by Dunn (1940) regarding the relationship of precipitation and cloud types to "isallobaric centers" (regions of greatest negative pressure tendency) in the Caribbean. In the Caribbean wave model, to the west of the wave axis, the depth of the moist layer is at a minimum, near 5,000 feet (~1500 meters), and largely associated with non-precipitating trade cumulus and cumulus humulis. This region of subsidence and surface divergence precedes the wave axis. Near and just to the east of the wave axis, the moist layer deepens rapidly to above 20,000 feet (~6100 meters) and cumulus congestus, cumulonimbus, altostratus, stratocumulus, altocumulus, and cirrus clouds are prevalent. Far to the east of the wave axis, the depth of the moist layer gradually decreases but is still accompanied by cumulus, cumulus congestus, stratocumulus, altocumulus, cirrus,

and occasional cumulonimbus. Thus, in the Caribbean wave model deep convection and column integrated moisture anomalies favor regions in and behind the wave axis. These observations of surface convergence to the east and surface divergence to the west of the wave axis were hypothesized by Riehl (1954) to result from the principles of conservation of potential vorticity in the moist layer for easterly currents passing through the wave. Subsequent modeling studies of EWs in the Caribbean corroborated Riehl's observational findings (Krishnamurti and Baumhefner 1966, Yanai and Nitta 1967).

The Atlantic wave model, often referred to as Frank's inverted V model, was first proposed by Simpson et al. (1968), and later developed by Frank (1969) using cloud mosaics from the television infrared observation satellite (TIROS) over the Atlantic. The distribution of clouds in the Atlantic wave model is banded and forms an upside down V shape. The Atlantic wave model mainly differs from the Caribbean wave model in that convection is equally distributed across the wave axis. The deep convective features in the Atlantic wave model are present both upstream and downstream of the wave axis and do not display a rapid buildup in cloud depth near the axis as in the Caribbean wave model. Frank (1969) suggested that differences in the mean state as well as the vigor of waves sampled in the studies were at least partly responsible for the differing distributions of convection between the Atlantic and Caribbean wave model.

The African wave model proposed by Carlson (1969) suggested that the maximum convection and precipitation associated with EWs over west Africa occurred ahead of the wave axis. Using GATE observations and SMS IR brightness temperatures, Reed et al. (1977) was able to confirm Carlson's results. The peak upward vertical motion occurred in advance of the wave axis and maximized near

700mb. The upstream convection persisted even when opposed by a relatively dry lower troposphere transported southward from the Sahara, suggesting that large-scale forcing was aiding convection ahead of the wave. The phasings of convection relative to the wave axis vary considerably based on the season and geographic location, but Carlson's original findings generally hold for waves in west Africa and south of the African easterly jet axis during June - October (Gu et al. 2004; Kiladis et al. 2006 and references therein).

Recent studies of EWs in the EPAC suggest various phasings of convection and moisture relative to the wave axis. Analysis of EW moisture by Serra et al. (2008) in the EPAC agrees with the Caribbean wave model. Positive specific humidity anomalies are confined to the lower troposphere in advance of the wave axis and rapidly deepen near the wave axis. These results also agree with an earlier study by Tai and Ogura (1987) that suggested deep convection occurs within or slightly behind the wave axis in the EPAC. Yet, results from Petersen et al. (2003) using Doppler radar from EPIC-2001 suggest that EWs in the EPAC are likely to have deep convection in front of the wave axis and weaker but more widespread convection at and behind the wave axis, although this study was derived for a relatively short time record. Furthermore, Serra and Houze (2002) note that EWs in the EPAC are readily identified in the EPAC by their inverted V shapes noted on visible satellite imagery, as in the Atlantic wave model. These differences in the phasing of convection with the wave circulation may partly result from sampling the wave at various stages of its life cycle and/or during different background states of the EPAC. The analysis below will support this contention.

Tropical convection shows strong sensitivity of precipitation to the build up and removal of free tropospheric moisture (Raymond, 2000; Sobel et al. 2004; Bretherton et al. 2004; Peters and Neelin 2006; Holloway and Neelin 2009, Sahany et al. 2012). We will show that anomalous convection favors certain regions of EWs, and these regions are also areas where vertically integrated moisture anomalies occur. The regulatory processes for the moisture anomalies are examined using a column-integrated moisture budget. We also partition the budgets with respect to intraseasonal phase, which is known to strongly modulate the background fields through which EWs propagate and are energized (e.g. Nitta and Takayuba 1985; Molinari and Vollaro 2000; Maloney and Hartmann 2001; Aiyyer and Molinari 2008; Rydbeck and Maloney 2014). Understanding the preferred regions of anomalous convection within EWs is important as the convection can locally generate vorticity through vorticity convergence. We hypothesize that the local generation of vorticity by convection leads to a horizontally tilted structure of the EW favorable for wave intensification in regions of background cyclonic shear.

A description of the data used in the study and the methods for compositing both EWs and intraseasonal events in the EPAC are described in section 3.2. Evolution of strong EWs during various intraseasonal states is described in section 3.3. The column integrated moisture budget for EWs is examined in section 3.4. The role of adiabatic forcing to support EW convection is investigated in section 3.5. Section 3.6 discusses how EW convection modulates the horizontal wave structure by briefly examining the vorticity budget. Section 7 presents the conclusions of the study.

## 3.2 Data and Methods

Temperature, specific humidity, precipitation, surface evaporation, and winds from the European Centre for Medium-Range Weather Forecasts Interim Reanalysis (ERAI) (Dee et al. 2011) are used throughout the study. The 6 hourly, 1.5° grid spaced data cover a 20 year period from 1991-2010. For the purposes of calculating column integrated moisture budgets, raw variables are used that span 1000 hPa to 200 hPa in 50 hPa intervals. The top level (200 hPa) is quite close to the typical level of neutral buoyancy for a boundary layer parcel during boreal summer in the Intra-American Seas (Jordan 1958). As a proxy for convection, the newly released National Climatic Data Center outgoing longwave radiation (OLR) daily climate data record from 1991-2010 is used (Lee 2014). Because only daily averages are available, the 1°x1° grid spaced OLR data are linearly interpolated to 6-hourly time steps to be utilized in the EW composites shown later.  The linearly interpolated NCDC OLR dataset is largely consistent with 6-hourly OLR data from ERAI in the EW composites (see Rydbeck and Maloney 2014).

EW fields are composited both as a function of EW phase and intraseasonal phase. The framework for identifying strong EWs relies on the use of the leading empirical orthogonal function (EOF) pair of 2.5 – 12 day bandpass filtered 700 hPa vorticity anomalies. Tropical cyclone related vorticity anomalies are removed as in Aiyyer et al. (2012) before the EOF analysis is performed on the filtered vorticity anomalies. The leading EOF pair describes a northwestward propagating vorticity anomaly that is used to partition the EW's lifecycle into eight EW phases. Only strong EWs, those exceeding 0.5 standard deviations, are chosen using amplitudes derived from the corresponding principal component (PC) pair. More details regarding the

methods used to calculate both EW and intraseasonal phase angle, amplitude, and selection criteria as well as the sensitivities of the methodology are described in Rydbeck and Maloney (2014).

The phase and amplitude criteria of the intraseasonal oscillation in the EPAC are based on the normalized leading PC of 30 – 90 day bandpass filtered 850 hPa zonal wind anomalies. Local maxima greater than 1.0 standard deviation are defined as the peak of westerly intraseasonal events. Local minima less than -1.0 are defined as the peak of easterly intraseasonal events. Neutral intraseasonal events are defined as the time step closest to zero for values between -0.5 and 0.5. Each intraseasonal period is defined to include the five days before and after the event's peak. As in Rydbeck and Maloney (2014), the results are not overly sensitive to reasonable changes in the thresholds used to identify EWs and intraseasonal events.

## 3.3 Easterly Wave Evolution

The background state through which EPAC EWs propagate shows dramatic variations in winds and shear, moisture and convection, and SST and latent heat fluxes on intraseasonal timescales (Maloney and Hartmann 2000, 2001; Molinari and Vollaro 2000; Maloney and Kiehl 2002; Maloney and Esbensen 2003, 2005, 2007; Aiyyer and Molinari 2008; Maloney et al. 2008; Jiang and Waliser 2008; Small et al. 2011; Rydbeck et al. 2013; Rydbeck and Maloney 2014; Crosbie and Serra 2014). Westerly intraseasonal periods are associated with enhanced low-level westerlies, precipitation, and surface latent heat fluxes. Easterly intraseasonal periods are associated with anomalous low-level easterlies, suppressed precipitation, and suppressed surface latent heat fluxes. These variations are associated with differences in the generation of EW

49

kinetic energy, with westerly intraseasonal periods characterized by significant increases in EW kinetic energy versus easterly intraseasonal periods (Maloney and Hartmann 2001; Hartmann and Maloney 2001; Aiyyer and Molinari 2008; Rydbeck and Maloney 2014, Crosbie and Serra 2014). To understand the intraseasonal variability of EWs as well as the evolution of EW convection and circulation anomalies, we review their composite structure as a function of intraseasonal phase.

Figure 3.1 shows the composite evolution of EW 2.5 – 12 day bandpass filtered 700 hPa vorticity and OLR anomalies during neutral intraseasonal periods. The EW initially develops in association with a weak positive vorticity anomaly located west of Panama in Phases 7, 8, and 1. Throughout this description of EW evolution, we concentrate on the half wavelength encompassing the positive vorticity anomaly, and use this synonymously with the term "easterly wave". This positive anomaly intensifies as OLR anomalies become increasingly negative. By phase 2, negative OLR anomalies associated with the incipient vortex are most prominent in the SW quadrant of the growing wave. In phase 4, the nascent positive vortex is tilted from the SW to the NE and negative OLR anomalies are still largely confined to the SW quadrant of the wave. Such a horizontal tilt could arise from low-level vorticity convergence forced by deep convection in that same SW quadrant. We will explore this stretching mechanism below when analyzing the vorticity budget. By phase 5, the vortex is prominently tilted from the SW to the NE, which would support EW kinetic energy generation by barotropic conversion in a region of cyclonic shear of the zonal wind that characterizes the basic state flow in this region (e.g. Figure 3.5 in Rydbeck and Maloney 2014). During phase 5, OLR minima are present in both the SW and NE quadrants of the wave. The wave

continues to intensify in phases 6, 7, and 8 as the OLR minimum in the SW quadrant weakens and the minimum previously in the NE quadrant intensifies and shifts slightly west of the wave. The intensification of the vorticity maximum and OLR minimum persist until the EW encounters cooler waters to the NW of the EPAC warm pool.



Easterly Wave OLR and 700hPa Vorticity (Neutral)
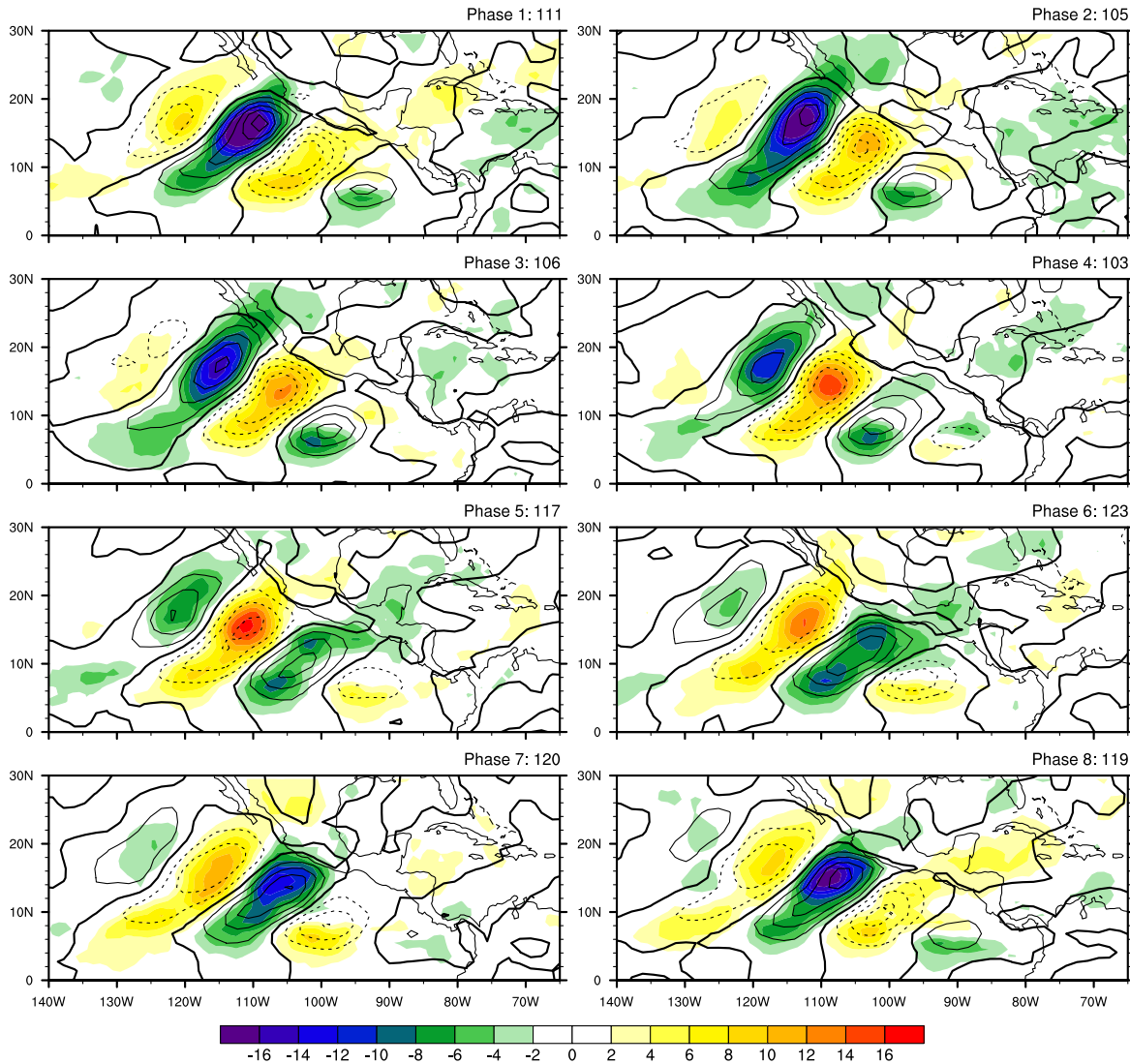
Fig. 3.1 2.5 – 12 day bandpass filtered 700 hPa relative vorticity (*$10^{-6}$ s$^{-1}$, line contours) and OLR (W m$^{-2}$, color contours) anomalies composited for neutral intraseasonal periods and strong easterly waves. Vorticity contour interval is 1*$10^{-6}$ s$^{-1}$. Zero relative vorticity contours are heavy solid lines, and positive (negative) contours are solid (dashed). Phase and number of days included in each composite are shown on the right above each panel.

EWs during westerly intraseasonal periods are characterized by stronger vorticity

and OLR anomalies (Figure 3.2) than waves during neutral intraseasonal

periods. Composites of EW anomalies during westerly intraseasonal periods are noisier

than those during neutral intraseasonal periods likely due to the reduced number of

events. The nascent vortex to the west of the Panama Bight in phase 8 quickly

intensifies by phase 1 while the anomalous OLR minimum in the SW quadrant

Easterly Wave OLR and 700hPa Vorticity (Westerly)



Fig. 3.2 Same as Figure 3.1 but for strong easterly waves during westerly
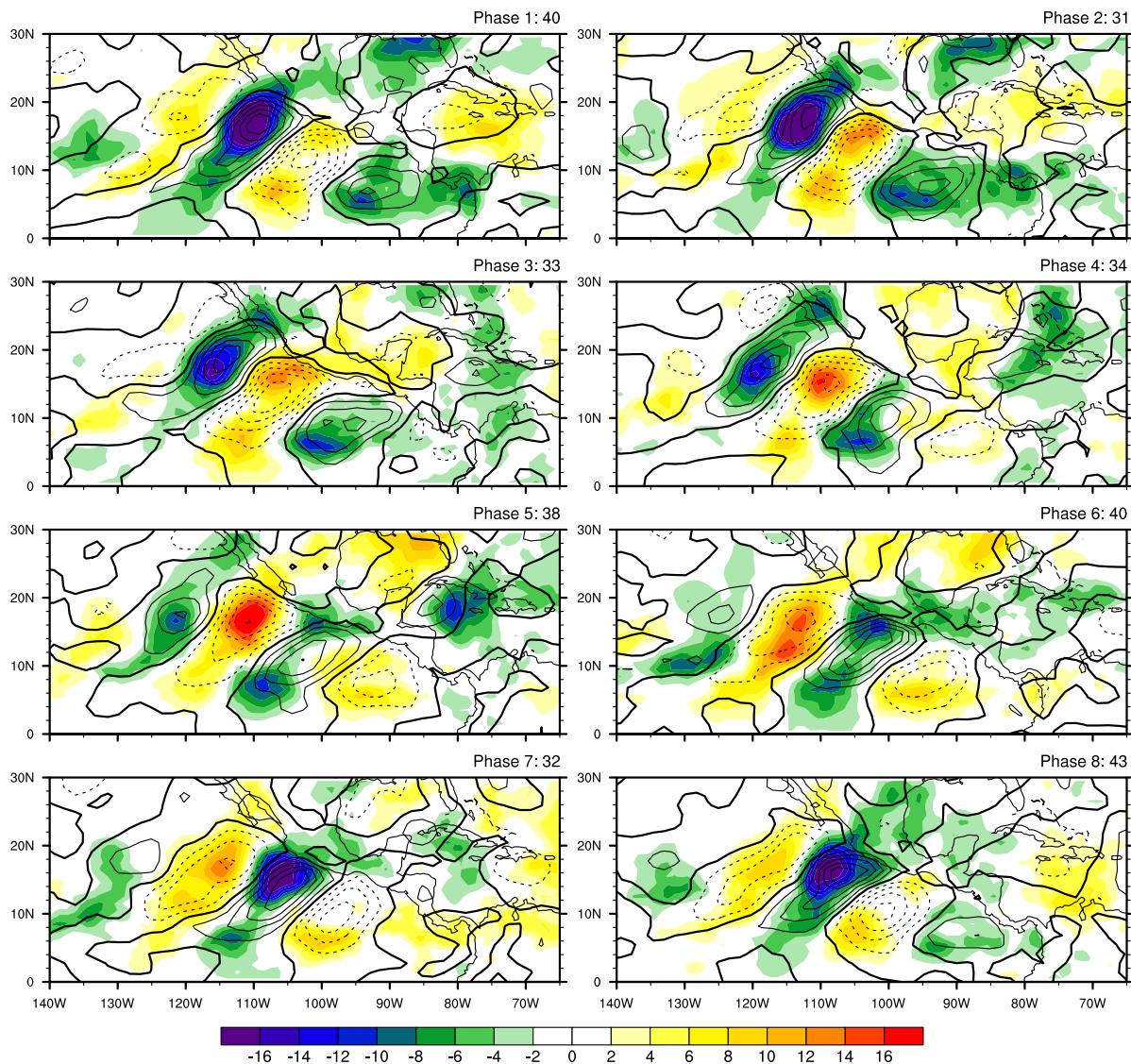intraseasonal periods.

increases in magnitude from -6 W/m$^2$ to -10 W/m$^2$. During phases 1 and 2, the OLR minimum in the SW quadrant of the nascent wave is connected to a tongue of negative OLR anomalies extending westward from Panama. Like EWs during neutral intraseasonal periods, the OLR minimum is largely confined to the SW quadrant as the wave matures. As the wave continues to grow in phase 5, a second OLR minimum develops in the NE quadrant. The wave axis also exhibits a prominent SW to NE tilt at this time. Through phases 6, 7, and 8 the OLR minimum in the NE quadrant intensifies from -8 W/m$^2$ to less than -16 W/m$^2$. The OLR minimum during these phases slightly leads the EW. The vortex eventually weakens in association with a weakened OLR minimum upon entering a region of climatologically cooler sea surface temperatures.

Composite EW vorticity is weaker during the incipient phases for easterly intraseasonal periods and slower to develop compared to neutral and westerly intraseasonal periods (Figure 3.3). OLR minima associated with the EW do not display a consistent strengthening in the early stages of the EW life cycle (phases 1, 2, 3, and 4). Unlike neutral and westerly intraseasonal periods, the OLR minimum slightly lags the positive vortex such that convection anomalies are located in the SE quadrant of the nascent vortex during phases 1 and 2. OLR anomalies associated with the nascent vortex weaken by phases 3 and 4 to greater than -4 W/m$^2$. OLR minima favor the NE quadrant by phases 6, 7, and 8. These phases are also when the maturing EW vortex exhibits a more defined SW to NE tilt. Vorticity and OLR anomalies associated with the mature EW are largely collocated during phases 1, 2, and 3.

The relationship of convection to the circulation of EWs varies as the wave grows from an incipient disturbance to a robust wave. The convection displays noteworthy

zonal and meridional asymmetries. Generally, the OLR minimum prefers the SW quadrant of the wave early in the life cycle and favors the NE quadrant as the wave reaches maturity. Strong convective anomalies are simultaneously present in both the SW and NE quadrants of growing waves during neutral and westerly intraseasonal periods. The asymmetries in convection occur in conjunction with asymmetries in the circulation, namely a SW to NE tilt of the horizontal flow field. We later discuss how the

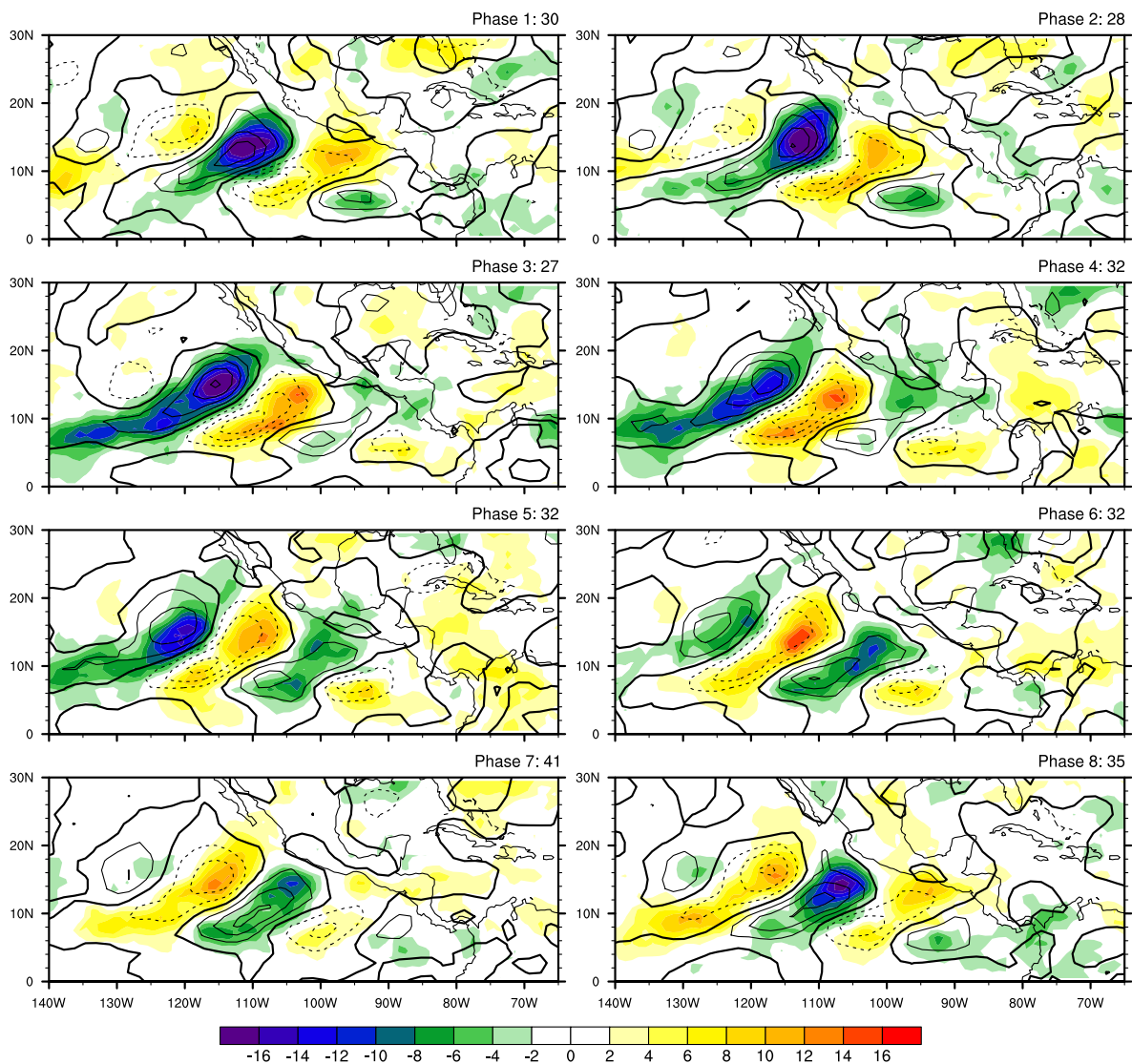Easterly Wave OLR and 700hPa Vorticity (Easterly)



Fig. 3.3 Same as Figures 3.1 and 3.2 but for strong easterly waves during easterly intraseasonal periods.

convection and circulation may be coupled to produce such an effect. The exception to this generalization occurs during easterly intraseasonal periods when convection is much weaker during the formative stages. Eventually a single but broad OLR minimum is centered near the vortex during peak intensity. The exact phasing and vigor of convection relative to the EW circulation varies as a function of the intraseasonal background state with the most vigorous EWs occurring during westerly intraseasonal periods and weakest waves during easterly intraseasonal periods. To verify that the features are strongly related to EWs and not tropical cyclones that project onto the same frequency band, we also removed the influence of tropical cyclones from the anomaly fields in the same manner as Rydbeck and Maloney (2014). The same conclusions hold (not shown here).

**3.4 Moisture Budget**

As mentioned previously, tropical convection exhibits strong sensitivity to free tropospheric moisture. More specifically, Raymond et al. (1998) noted the importance of moistening the middle troposphere to the development and maintenance of deep convection in EPAC EWs during the summer of 1991. EW composites of 2.5 – 12 day bandpass filtered total precipitable water (TPW), OLR, and 700 hPa wind anomalies during phases 3 and 7 for neutral, westerly, and easterly intraseasonal periods, respectively, are shown in Figure 3.4 to determine if a similar relationship between moisture and convection is present. Regardless of the intraseasonal period, TPW maxima (minima) are generally collocated and supportive of the OLR minima (maxima) during both incipient and mature stages of the EW. Building on the previous large body of observational and modeling evidence that suggests daily mean tropical convection

and precipitation are strongly constrained by column moisture, we now analyze the processes that regulate moisture locally on EW timescales utilizing the vertically integrated moisture budget. It is hypothesized that moisture anomalies in the SW and NE quadrants support convection anomalies that help tilt growing waves in a manner

## Easterly Wave Total Precipitable Water
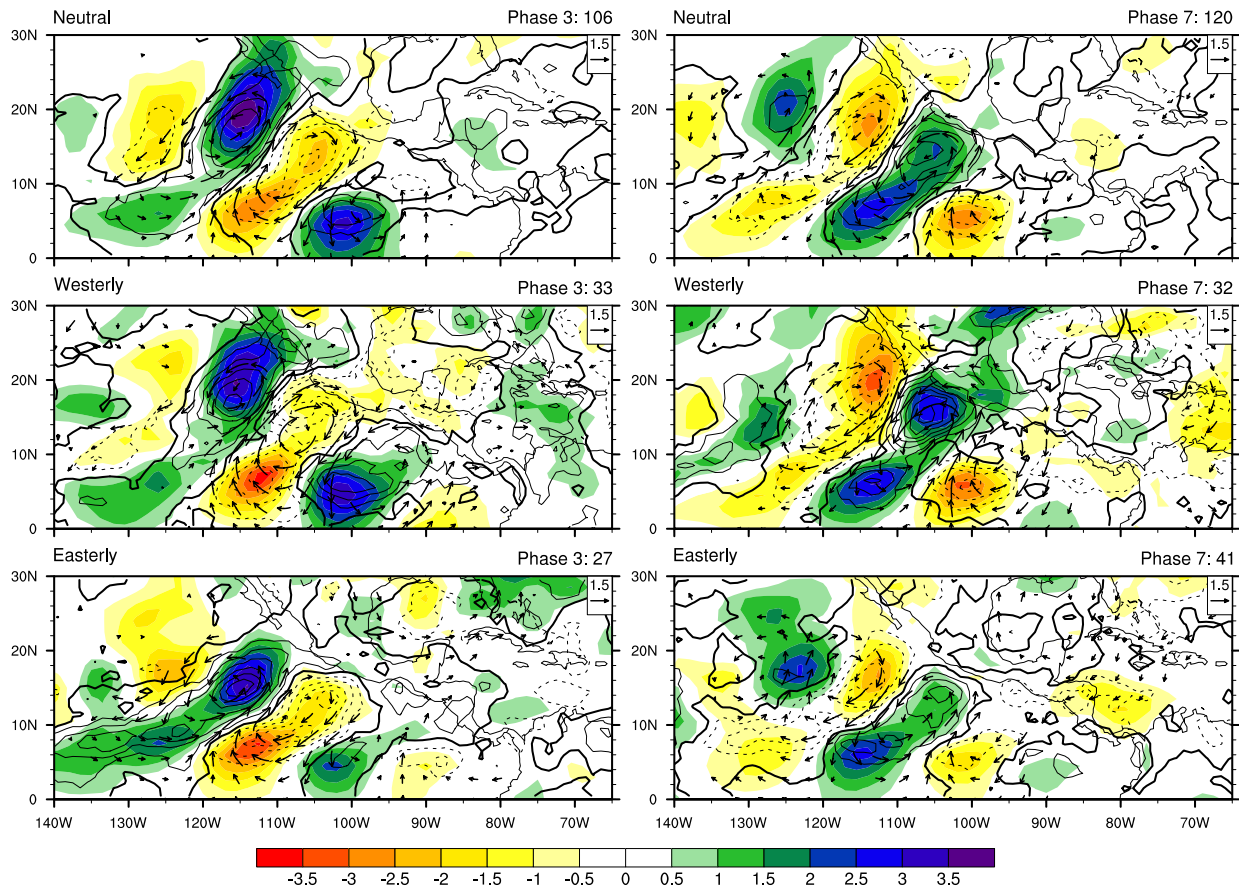


Fig. 3.4 2.5 – 12 day bandpass filtered TPW (mm, color contours), OLR (W m$^{-2}$, line contours), and 700 hPa wind (m s$^{-1}$, vectors) anomalies composited for phases 3 (left) and 7 (right) of neutral (top row), westerly (middle row), and easterly (bottom row) intraseasonal periods and strong easterly waves. OLR contour interval is 3 W m$^{-2}$. Zero OLR contours are heavy solid lines, and negative (positive) contours are solid (dashed). Phase and number of days included in each composite are shown on the right above each panel. Reference wind vectors are located in the upper right of each panel. Wind vectors less than 0.3 m s$^{-1}$ are not shown.

favorable for increased barotropic conversion of EW kinetic energy as quantified in Rydbeck and Maloney (2014). The vertically integrated moisture budget is approximately given by:

$$\left[\frac{\partial q}{\partial t}\right]' = -[v_h \bullet \nabla_h q]' - \left[\omega\frac{\partial q}{\partial p}\right]' + E' - P' \qquad (1)$$

where $[\ ]$ represents the mass-weighted vertical integral from 1000 hPa to 200 hPa and

′ represents a 2.5 – 12 day bandpass filter. The term on the left hand side of equation 1 represents the vertically integrated 2.5 – 12 day bandpass filtered specific humidity tendency. This term is simply referred to as the EW moisture tendency. The first term on the right hand side of equation 1 is the moisture tendency resulting from horizontal advection. The second term on the right hand side is the moistening by vertical advection. The third and fourth terms on the right hand side are the column moisture tendency due to surface evaporation and precipitation, respectively.

### 3.4.1 Neutral Intraseasonal Periods

The composite evolution of the EW moisture tendency for phases 3 and 7 during neutral periods is shown in the top row of Figure 3.5. The positive moisture tendency during the early period of the EW lifecycle maximizes in the SW quadrant of the wave, near the transition between the ridge and trough. That same positive moisture tendency is present in the SE quadrant of the ridge before the nascent EW is well established as can be seen in phase 7 near 5° N, 95° W. For the strongest EW vorticity center seen in phase 7, the positive moisture tendency is elongated and leads the wave with maxima in advance of the SW and NE quadrants. Compared with Figure 3.4, anomalous moistening is occurring in advance of the negative OLR and positive TPW anomalies

57

associated with the westward-propagating wave. By phases 8, 1, and 2 (not shown), the

positive moisture tendency in advance of the NE quadrant of the mature EW intensifies

and the local maximum in the SW quadrant relaxes such that only a single moistening
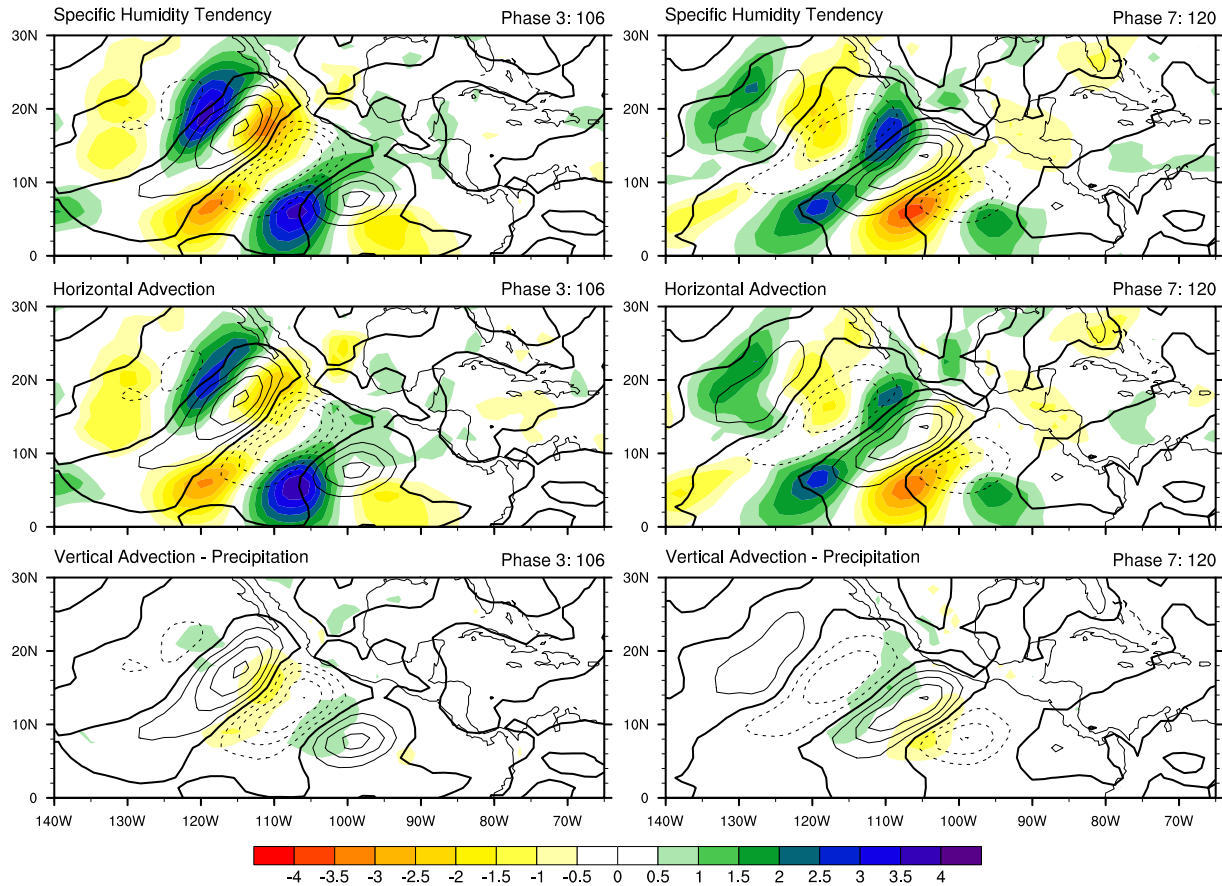


Fig. 3.5 Composite overlay of 2.5 – 12 day bandpass filtered 700 hPa relative vorticity ($*10^{-6}$ $s^{-1}$, line contours) with easterly wave specific humidity tendency (mm $day^{-1}$, color contours, top row), horizontal advection (mm $day^{-1}$, color contours, middle row), and vertical advection minus precipitation (mm $day^{-1}$, color contours, bottom row) for phases 3 (left) and 7 (right) of neutral intraseasonal periods and strong easterly waves. Vorticity contour interval is $1*10^{-6}$ $s^{-1}$. Zero relative vorticity contours are heavy solid lines, and positive (negative) contours are solid (dashed). Phase and number of days included in each composite are shown on the right above each panel.

maximum occurs in advance of the wave, as can be seen in phase 3. Peak moistening

over the life cycle of the wave first occurs ahead of the SW quadrant with values of 3.5

mm/day during phase 3 and in advance of the NE quadrant of developed waves at

approximately 4 mm/day during phases 1 and 2 (not shown). In the interim stages, maxima in moistening occur simultaneously both in advance of the SW and NE quadrants during phase 7 with values of 2.5 mm/day. For growing waves in phases 3 and 7, moisture tendency minima are located behind the wave axis, in the SE quadrant, indicating drying behind the wave.

Early in the wave's life cycle during neutral periods, evaporation opposes the positive moisture tendency by up to -0.7 mm/day in the SW quadrant (not shown). A similar evaporation tendency is observed for EWs during both westerly and easterly intraseasonal periods. The combination of vertical moisture advection and precipitation is described next. In general, separating cause and effect between condensational heating and vertical velocity in the tropics is complicated (e.g. Sobel and Bretherton 2000; Back and Bretherton 2009), and hence we choose to examine these two processes in tandem. Confidently calculating vertical advection minus precipitation using reanalysis data is difficult and as a result the difference is formulated as the residual of the other terms in the budget. Any analysis increments used to constrain the ERA-I moisture field in the assimilation process are also likely the result of errors in moist physics that would be included in the sum of vertical advection and precipitation (e.g. Wolding and Maloney 2015), and hence it makes sense to calculate this difference as a residual. We note that vertical advection minus precipitation calculated explicitly is qualitatively similar to vertical advection minus precipitation calculated as the residual of the other terms, however. In the difference between the vertical advection and precipitation (bottom row of Figure 3.5), positive regions indicate where vertical advection is moistening the atmosphere in opposition to drying by precipitation. Thus,

moistening during the incipient stages of the EW not counteracted by precipitation preferentially occurs ahead of the wave, with values of 0.5 – 1 mm/day. Anomalous drying resulting from precipitation that is stronger than vertical advection occurs behind the wave. Processes that might play a moistening role are adiabatic forcing and/or shallow non-precipitating convection. We explore the former possibility in section 6 by estimating Q vector divergence. However, the difference between vertical advection and precipitation is substantially smaller than the total moisture tendency.

Horizontal advection is the largest contributor to the positive tendency of column integrated moisture tendencies ahead of EW convection (middle row of Figure 3.5). Compared to the column integrated moisture tendency, the minima and maxima of column integrated horizontal advection are collocated and of comparable values. Since precipitation and vertical advection largely cancel and evaporation weakly opposes the positive moisture tendencies of incipient waves, the overwhelming majority of the moisture tendency is due to horizontal advection. The contributions by zonal and meridional advection, respectively, comparably contribute to the horizontal advection during neutral intraseasonal periods (not shown). The horizontal advection term can further be understood using the following decomposition of the horizontal advection to highlight the respective roles of the mean and perturbation flow and moisture gradients:

$$\left[ -v_h \bullet \nabla_h q \right]' = -\left[ u'' \frac{\partial \overline{q}}{\partial x} \right]' - \left[ v'' \frac{\partial \overline{q}}{\partial y} \right]' - \left[ \overline{u} \frac{\partial q''}{\partial x} \right]' - \left[ \overline{v} \frac{\partial q''}{\partial y} \right]' - \left[ u'' \frac{\partial q''}{\partial x} \right]' - \left[ v'' \frac{\partial q''}{\partial y} \right]'$$

(2)

where $-$ indicates a ten day running mean and $''$ indicates deviations from a ten day running mean. The first and second terms on the right hand side of equation (2) are the

zonal and meridional advection of mean moisture by the perturbation zonal and meridional winds, respectively. The third and fourth terms on the right hand side are the zonal and meridional advection of the perturbation moisture by the mean zonal and meridional winds, respectively. The fifth and six terms on the right hand side are the advection of perturbation moisture by perturbation winds.

Of the six terms on the RHS of equation (2), the advection of mean moisture by the perturbation meridional winds, $-\left[ v'' \dfrac{\partial \overline{q}}{\partial y} \right]'$, (bottom row of Figure 3.6) and the

advection of perturbation moisture by the mean zonal winds, $-\left[ \overline{u} \dfrac{\partial q''}{\partial x} \right]'$, (top row of

Figure 3.6) are the major contributors to the observed horizontal moisture advection seen in Figure 3.5. The moistening resulting from advection of mean moisture by the perturbation meridional winds occurs preferentially ahead of the wave in the region of the wave containing a strong northerly wind component (see Figure 3.4). This relationship reverses when the meridional moisture gradient flips sign as the wave is exiting the NW side of the warm pool near Baja California Sur. Figure 3.7 (bottom panel) shows the mean distribution of TPW during neutral intraseasonal periods. A zonally elongated strip of maximum precipitable water extends from the Panama Bight to the west-northwest until approximately 100°W where it continues to the west along 9°N. As the incipient wave grows, it preferentially advects high TPW southward toward regions of lower TPW, creating anomalously high TPW values in the SW quadrant of the wave. The meridional advection of mean moisture by perturbation meridional winds

contributes over 3 mm/day to the moisture tendency during the growing stages of the
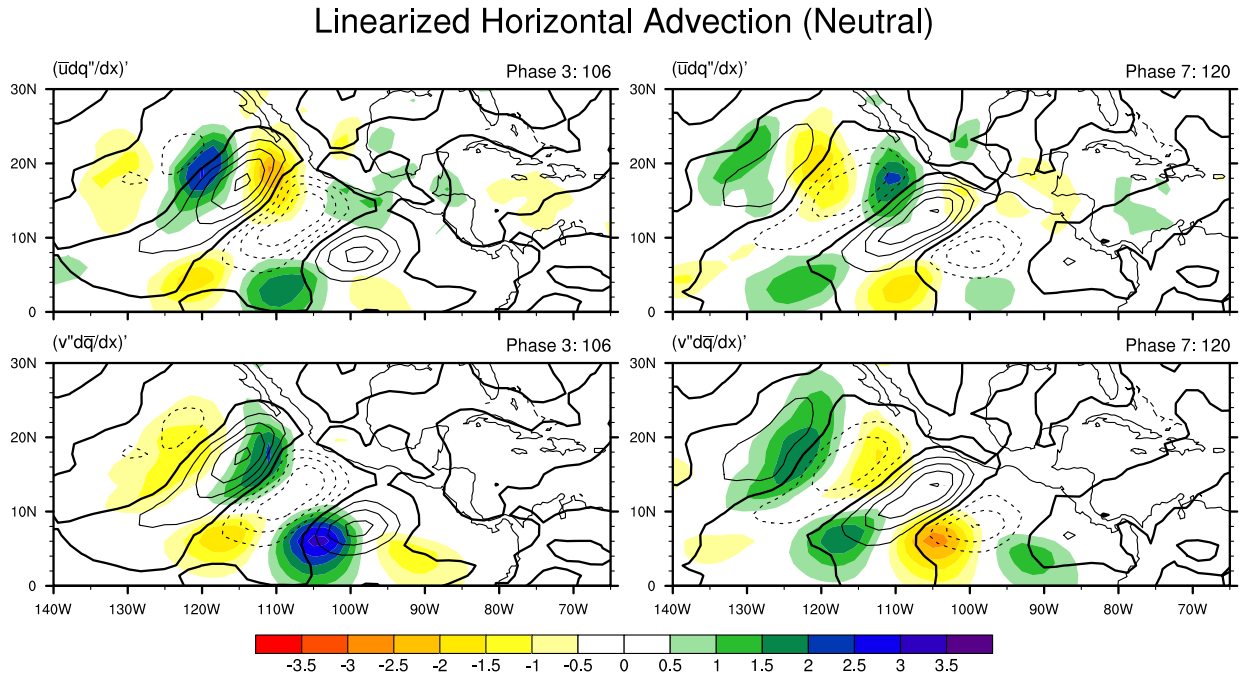
EW as seen in phase 3 of Figure 3.6.

## Linearized Horizontal Advection (Neutral)



Fig. 3.6 Composite overlay of 2.5 – 12 day bandpass filtered 700 hPa relative vorticity (*$10^{-6}$ s$^{-1}$, line contours) with easterly wave linearized horizontal

advection terms, $-\left[\overline{u}\dfrac{\partial q''}{\partial x}\right]'$ (mm day$^{-1}$, top row) and $-\left[v''\dfrac{\partial \overline{q}}{\partial y}\right]'$ (mm day$^{-1}$, bottom

row) for phases 3 (left) and 7 (right) of neutral intraseasonal periods and strong easterly waves. Vorticity contour interval is 1*$10^{-6}$ s$^{-1}$. Zero relative vorticity contours are heavy solid lines, and positive (negative) contours are solid (dashed). Phase and number of days included in each composite are shown on the right above each panel.

Zonal advection of perturbation moisture anomalies by the mean zonal winds

contributes over 1.5 mm/day to the moisture tendency increase in the SW quadrant of

nascent EWs. In mature EW stages, zonal advection of perturbation moisture by the

mean zonal winds moistens in excess of 2 mm/day ahead of convection in the NE

quadrant. Perturbation zonal winds acting on the mean zonal moisture gradient,

$-\left[\overline{u}\dfrac{\partial q''}{\partial x}\right]'$, also contribute to moistening in this region by 0.5 mm/day (not shown).

## Total Precipitable Water Composite
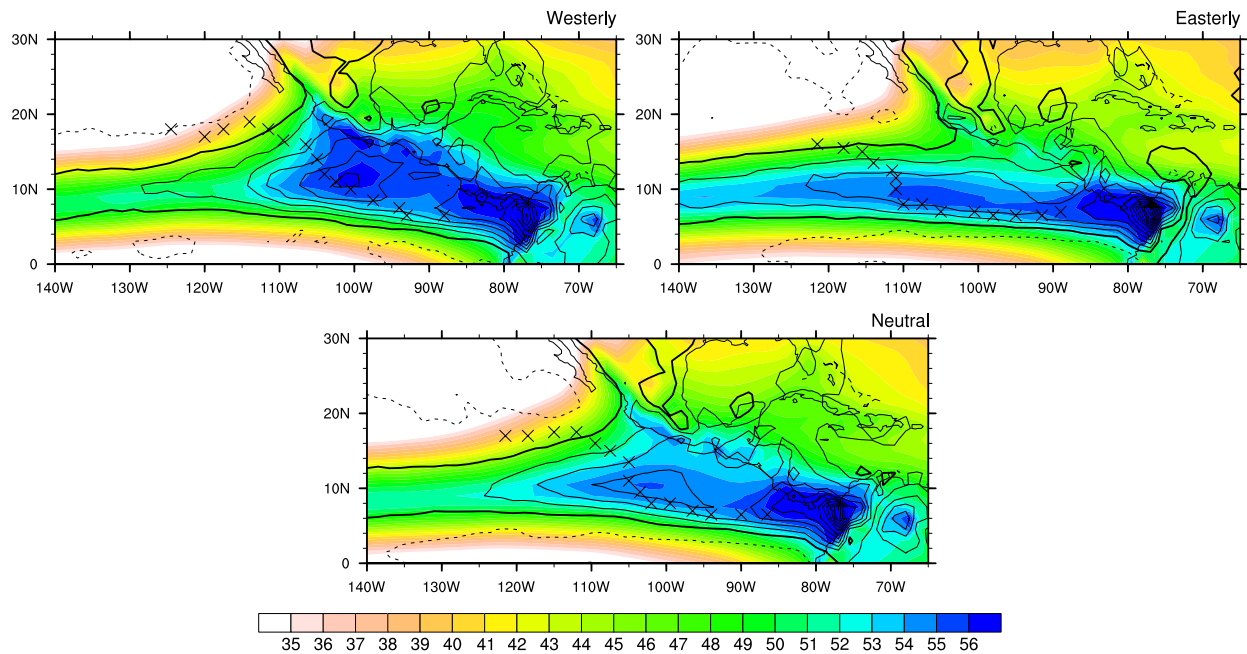


Fig. 3.7 Composites of 400 hPa vertical velocity (Pa s$^{-1}$, line contours) and total precipitable water (mm, color contours) for westerly (upper left), easterly (upper right), and neutral (bottom) intraseasonal periods. Vertical velocity contour interval is .025 Pa s$^{-1}$. Zero vertical velocity contours are heavy solid lines, and negative (positive) vertical velocity contours are solid (dashed). Tracks of easterly wave 700 hPa vortices are indicated with the symbol "X".

To summarize, TPW anomalies are in phase with OLR anomalies in EWs. Regions ahead of the EW convection are moistened largely as a result of horizontal advection. During the early stages of an EW, moisture increases occur in the SW quadrant due to EW meridional winds acting on the mean moisture gradient collocated with the mean ITCZ. As the wave intensifies and shifts northwestward away from the strong meridional moisture gradient on the equatorward side of the ITCZ, the positive moisture tendency in the SW quadrant weakens. At this time moistening in advance of convection in the NE quadrant of the wave intensifies due to the zonal advection of moisture anomalies.

**3.4.2 Westerly and Easterly Intraseasonal Periods**

The locations of column integrated moisture tendency maxima for EWs during westerly and easterly intraseasonal periods are similar to those in the neutral intraseasonal composite relative to the EW train (top row of Figures 3.8 and 3.9). However, differences exist in their magnitude, especially during westerly intraseasonal periods. For example the composite moisture tendency ahead of the mature EW in phase 7 during westerly intraseasonal periods is 40% stronger than the maximum during neutral intraseasonal periods. Likewise, the tendency of moisture in the SW quadrant of the nascent EW in phase 8 (not shown) is 40% stronger during westerly versus neutral intraseasonal periods. Figures 3.1 and 3.2 showed that the OLR anomalies during westerly intraseasonal periods increase more rapidly than those during neutral intraseasonal periods. Moisture tendencies acting to increase moisture anomalies that are supportive of the convection anomalies exhibit the same behavior.

EWs during easterly intraseasonal periods are characterized by weak and sometimes absent OLR anomalies during early stages of the EW life cycle compared to neutral and westerly intraseasonal periods (see Figure 3.3). Anomalous moisture tendencies and TPW are reduced as well during easterly intraseasonal periods. For example, the moisture tendency maximum during easterly intraseasonal periods is weaker by 20% in advance of the NE quadrant during phase 7 when compared to the similarly placed maximum during neutral intraseasonal periods. The TPW anomalies during easterly intraseasonal periods are likewise reduced by approximately 30% in the SW quadrant of phase 3 compared to neutral intraseasonal periods (see Figure 3.4). The sensitivity of anomalous convection to anomalous atmospheric moisture content is

explored by comparing variations in diluted convective available potential energy (CAPE) anomalies for different intraseasonal periods at the end of the section.

## Moisture Budget Terms (Westerly)
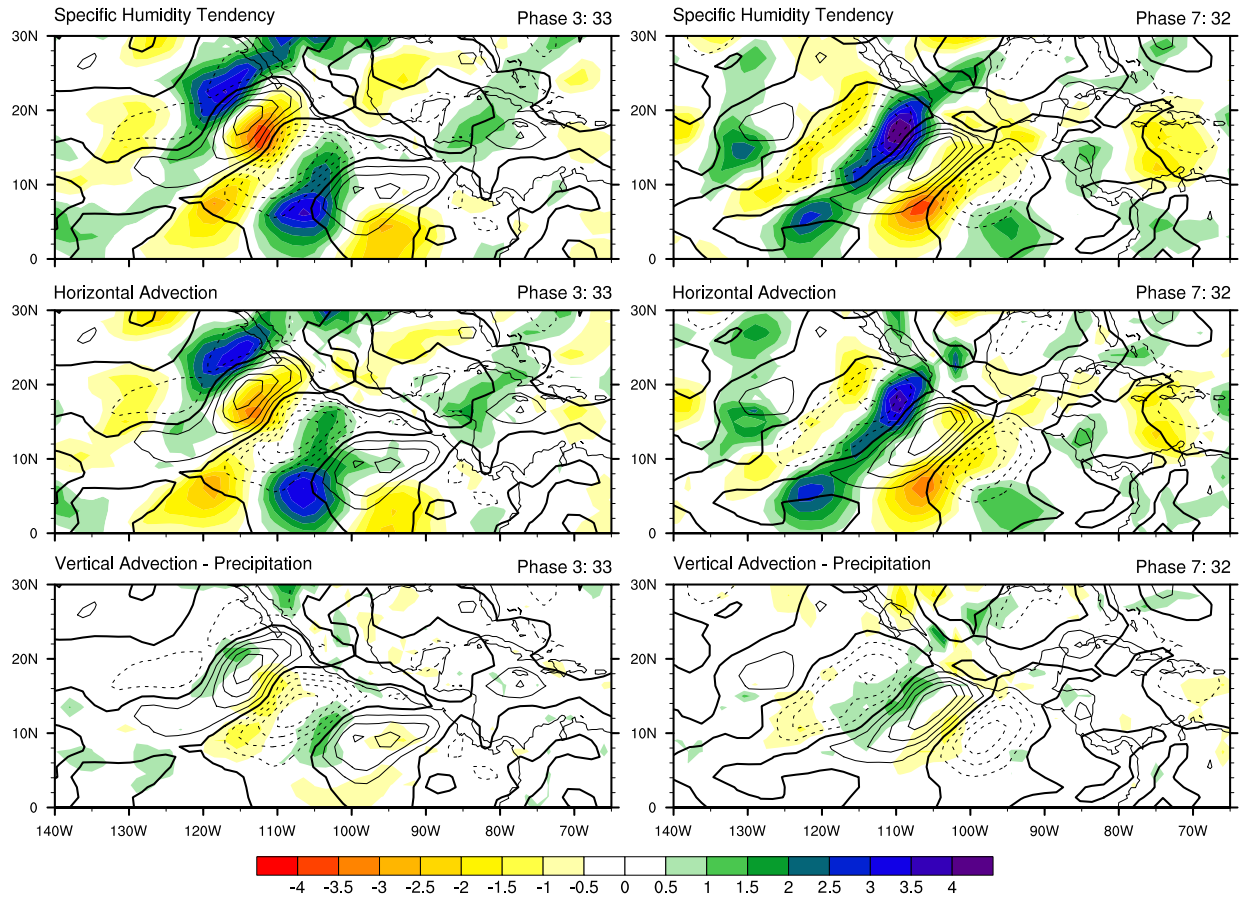


Fig. 3.8 Same as Figure 3.5 but for strong easterly waves during westerly intraseasonal periods.

Moistening of 1 mm/day and 0.5 mm/day, respectively, resulting from differences in vertical advection and precipitation occurs ahead of nascent and mature EWs during westerly and easterly intraseasonal periods (bottom row of Figures 3.8 and 3.9). Moistening by this term is stronger during westerly intraseasonal periods and not as consistent or robust throughout the wave's life cycle during easterly intraseasonal periods when compared to neutral periods.

Like neutral intraseasonal periods, horizontal advection is responsible for most of the EW column integrated moisture tendency during westerly and easterly intraseasonal

## Moisture Budget Terms (Easterly)
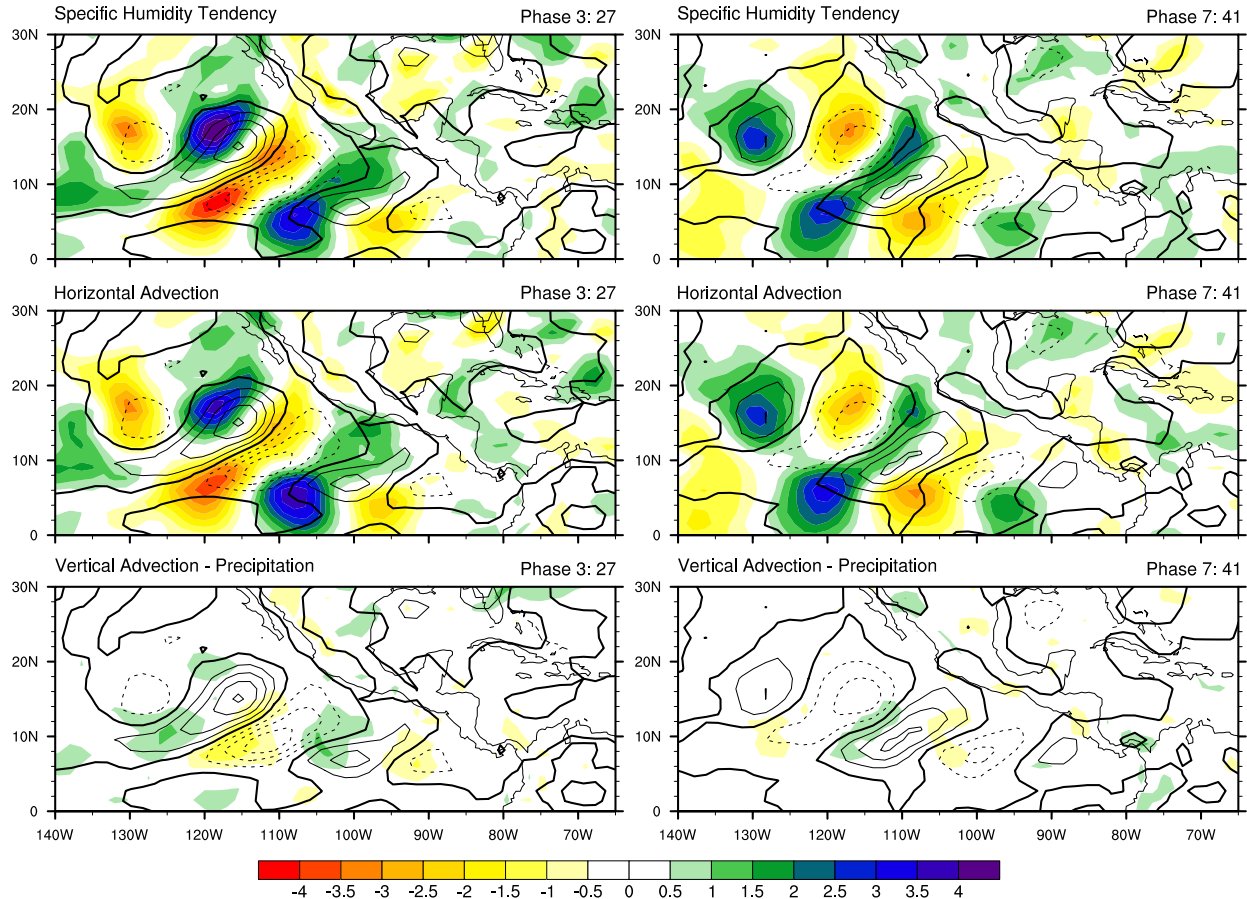


Fig. 3.9 Same as Figures 3.5 and 3.8 but for strong easterly waves during easterly intraseasonal periods.

periods (middle row of Figures 3.8 and 3.9). During westerly intraseasonal periods, total meridional advection contributes up to 40% more than the total zonal advection during the mature stages of the EW (not shown). During easterly intraseasonal periods, total zonal advection is up to 60% stronger than total meridional advection for the mature stages of the EW life cycle (not shown). Using equation (2) for westerly intraseasonal periods, horizontal moisture advection in the SW quadrant during the early stages of the EW is shown to be primarily supported by the perturbation meridional winds acting on

the mean meridional moisture gradient, $-\left[v''\dfrac{\partial \overline{q}}{\partial y}\right]'$, (bottom row of Figure 3.10) that are

approximately 15% stronger during phase 3 than those during neutral intraseasonal

periods. This result might be expected given the stronger EW circulations during

westerly intraseasonal periods (see Figure 3.4; Maloney and Hartmann 2001; Rydbeck

and Maloney 2014, Crosbie and Serra 2014). At the same phase and in the same

location, the maximum for $-\left[v''\dfrac{\partial \overline{q}}{\partial y}\right]'$, during easterly intraseasonal periods is 50%

weaker (bottom row of Figure 3.11).

### Linearized Horizontal Advection (Westerly)



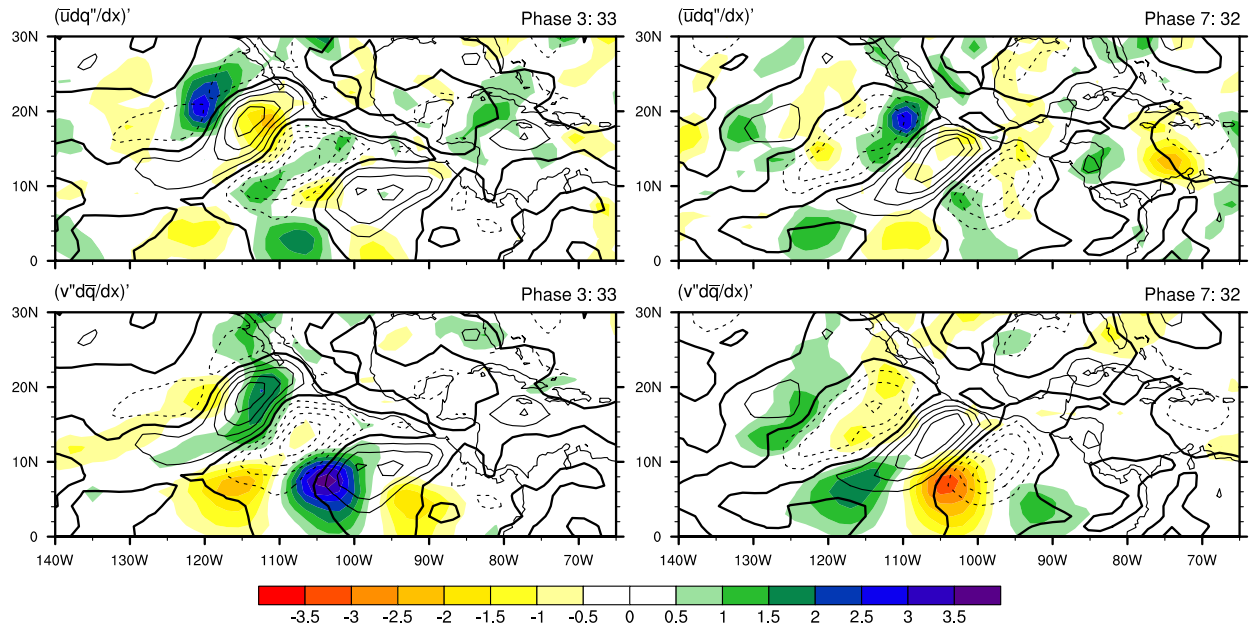Fig. 3.10 Same as Figure 3.6 but for strong easterly waves during westerly
intraseasonal periods.

The positive moisture tendency in the SW quadrant is reinforced by the mean

zonal winds acting on the perturbation zonal moisture gradient, $-\left[\overline{u}\dfrac{\partial q''}{\partial x}\right]'$, during both

westerly and easterly intraseasonal periods (top row of Figures 3.10 and 3.11). For

mature stages of the EW this term contributes up to 2.5 mm/day of the moisture tendency ahead of the wave during westerly intraseasonal periods and 3.5 mm/day during easterly intraseasonal periods . Although not as strong, in the western region of the EPAC warm pool, perturbation zonal winds acting on the mean zonal moisture gradient have a non-negligible contribution to the column moistening on the poleward side of a mature EW, up to 2 mm/day during westerly intraseasonal periods (not shown).

## Linearized Horizontal Advection (Easterly)
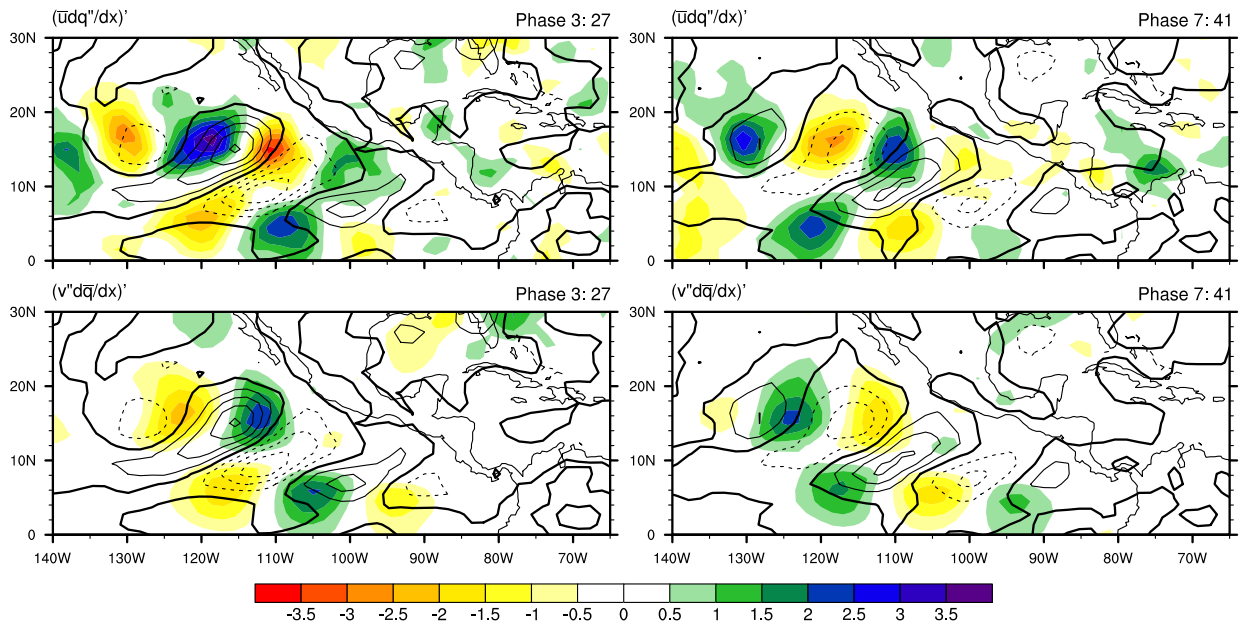


Fig. 3.11 Same as Figures 3.6 and 3.10 but for strong easterly waves during easterly intraseasonal periods.

The advection of mean moisture by the perturbation meridional winds, $-\left[v'' \dfrac{\partial \overline{q}}{\partial y}\right]'$, is a dominant term in the moisture budget for EWs during neutral and westerly intraseasonal periods. The mean moisture gradient is represented in Figure 3.7 by the mean TPW for each intraseasonal period. The mean 400 hPa pressure velocity is overlaid to indicate regions of deep rising motion indicative of the climatological ITCZ.

68

Also, the tracks of the 700 hPa EW vortex centers are shown. Compared to neutral intraseasonal periods, the background TPW in the EPAC warm pool during westerly intraseasonal periods is enhanced along the track of EWs, consistent with the findings of Crosbie and Serra (2014). TPW during easterly intraseasonal periods extends more continuously to the west and is narrower in latitude compared to neutral and westerly intraseasonal periods. Only slight variations in TPW occur near the Panama Bight among the different intraseasonal periods. Midlevel upward pressure velocities are also enhanced during westerly intraseasonal periods and suppressed during easterly intraseasonal periods compared to neutral intraseasonal periods. During all intraseasonal periods, EW tracks initially follow the equatorward side of the ITCZ. At these times, ahead of the wave, anomalous meridional winds are advecting the mean moisture equatorward. This process is particularly important when the anomalous meridional winds of the EW are strong (i.e. during westerly and neutral intraseasonal periods). Eventually, the tracks shift to the north and the gradient of background meridional moisture on which the EWs operate is reduced, thus shutting down the moisture advection into the SW quadrant of the wave (see bottom row of Figures 3.6, 3.10, and 3.11).

To examine why comparable EW moisture tendencies during various background intraseasonal states result in different convection anomalies, we examine the diluted CAPE anomalies calculated using a prescribed entrainment rate of .18 hPa$^{-1}$ in the atmospheric boundary layer (below 950 hPa) and .002 hPa$^{-1}$ in the free troposphere. Sahany et al. (2012) showed these entrainment rates (referred to as entrainment case "C2" in that paper) to produce a reasonable representation of tropical convective onset

in the Pacific. The plume is assumed to be saturated at 1000 hPa. In using diluted CAPE, the effects of environmental mixing with a saturated plume are included. Figure 3.12 shows diluted CAPE anomalies for phases 3 and 7 of EWs during neutral (top row), westerly (middle row), and easterly (bottom row) intraseasonal periods. During phase 3, the nascent EW during westerly intraseasonal periods contains strong positive CAPE anomalies of 200 J/kg in the SW quadrant of the composite wave. This is double
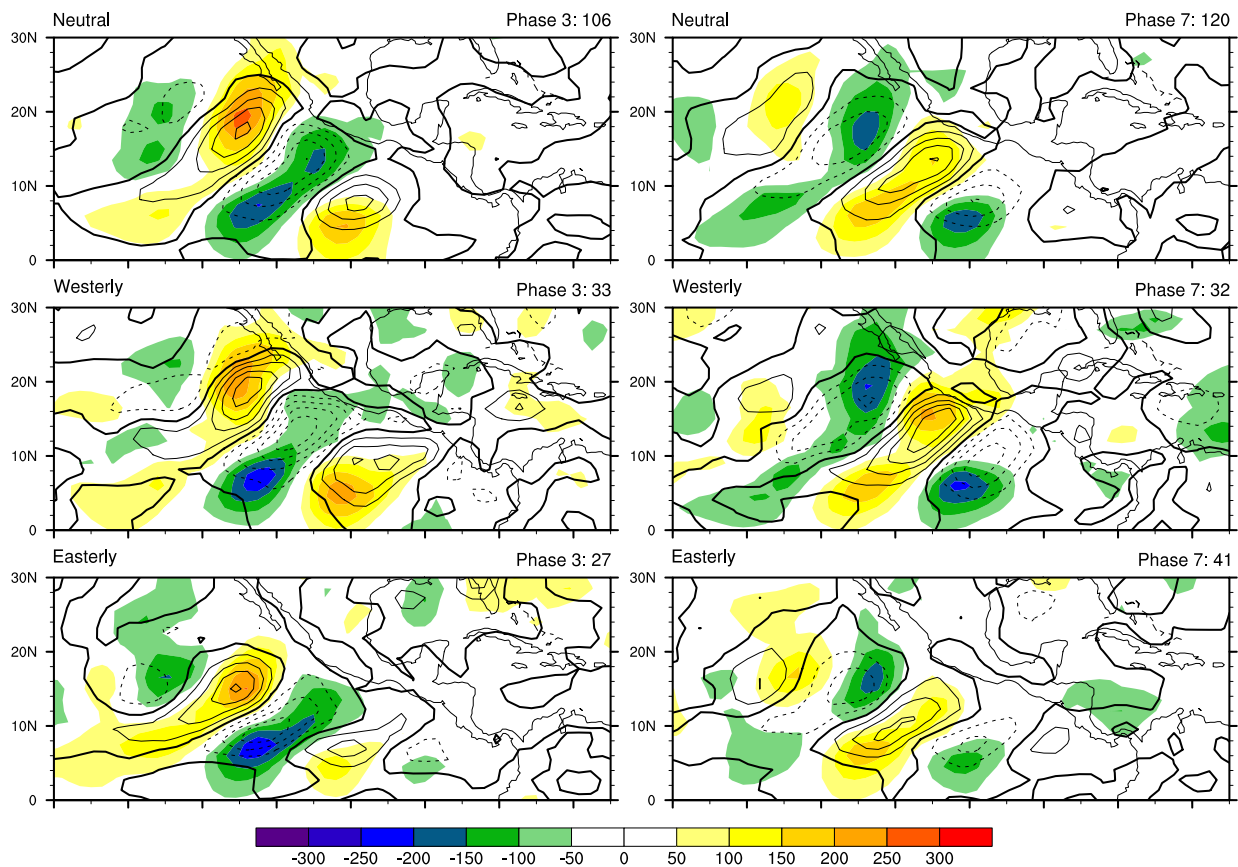


Fig. 3.12 2.5 – 12 day bandpass filtered 700 hPa relative vorticity (*$10^{-6}$ s$^{-1}$, line contours) and diluted CAPE (J kg$^{-1}$, color contours) anomalies composited for phases 3 (left) and 7 (right) of neutral (top row), westerly (middle row), and easterly (bottom row) intraseasonal periods and strong easterly waves. Vorticity contour interval is 1*$10^{-6}$ s$^{-1}$.  Zero vorticity contours are heavy solid lines, and positive (negative) contours are solid (dashed). Phase and number of days included in each composite are shown on the right above each panel.

the anomalous diluted CAPE that occurs in a similar region of the EW during easterly intraseasonal periods. As a result, moisture anomalies during easterly intraseasonal periods are less supportive of convection anomalies during the easterly intraseasonal period. For phase 7, the mature wave during westerly periods has a local maximum of diluted CAPE located in advance of the NE quadrant that is ill defined at that phase for neutral and easterly intraseasonal periods. Diluted CAPE anomalies build more rapidly during westerly intraseasonal periods throughout the EW lifecycle compared to other intraseasonal periods, providing a more favorable state for anomalous deep convection.

## 3.5 Adiabatic Forcing

As noted earlier, moistening due to differences between vertical advection and precipitation suggests a possible role for large-scale forcing of convection in advance of EWs, especially if it can be shown that a component of low-level vertical velocity (and hence vertical moisture advection) is forced by the dynamics of the EWs in isolation from convection. Differences in vertical advection and precipitation are most notable in neutral and westerly intraseasonal periods. We focus on neutral intraseasonal periods because of the larger sample size. To explore the possible role of adiabatic forcing of vertical motion, a simple approximation for Q vector divergence is presented. Vertical motions induced by adiabatic forcing are likely amplified by diabatic processes in EWs such that the vertical velocity fields suggested by the Q vector divergence analysis should only be qualitatively compared to the observed variability. Kiladis et al. (2006) analyzed the Q vector divergence of African EWs in the southern wave track. They found that the location of vertical motion associated with adiabatic forcing quantified by

the Q vector divergence was largely a result of the advection of perturbation vorticity by the mean thermal wind.

The approximate form of the Q vector divergence utilized in Kiladis et al. (2006) but expanded in this study to include both meridional and zonal advection of perturbation vorticity by the mean thermal wind is:

$$\frac{p}{R}\nabla_h \bullet Q_h'' \approx -\left(\frac{\partial \overline{T}}{\partial y}\frac{\partial \zeta_p''}{\partial x} + \frac{\partial \overline{T}}{\partial x}\frac{\partial \zeta_p''}{\partial y}\right) \quad (3)$$

where $Q_h''$ is the horizontal Q vector, $\overline{T}$ is the 10-day running mean temperature, $\zeta_p''$ is the deviation of the vertical vorticity from the 10-day running mean vertical vorticity, p is the pressure, and $R$ is the gas constant of dry air. The full Q vector equation as well as motivation for using the approximate form can be found in the appendix of Kiladis et al. (2006).

Similar to the results of Kiladis et al. (2006), the bulk of the adiabatic forcing calculated using equation (3) comes from the term representing the effect of perturbation vorticity advection by the mean thermal wind in the zonal direction, although the entire term will be shown. The Q vector divergence at 900 hPa associated with strong EWs for select phases during neutral intraseasonal periods is shown in Figure 3.13. Caution is taken when interpreting the results near the coast as the assumptions for Q vectors may not be well constrained there given the strong influence of the Sierra Madre. Away from the coast, Q vector forcing associated with upward vertical motion is located ahead of maturing waves during phases 1, 3, 5, and 7. Q vector forcing associated with downward motion is located behind the wave. Thus, adiabatic forcing of vertical motion is favored ahead of the wave while descending

Easterly Wave Q Vector Divergence (Neutral)
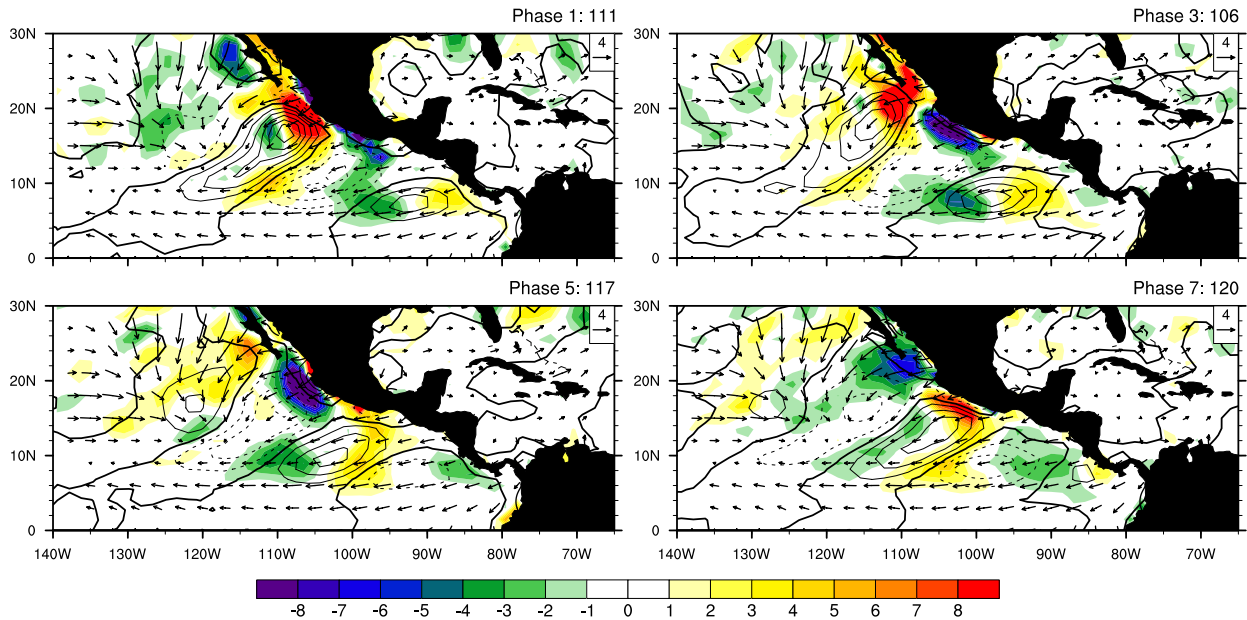


Fig. 3.13 2.5 – 12 day bandpass filtered 900 hPa relative vorticity anomalies ($*10^{-6}$ $s^{-1}$, line contours), 900 hPa Q vector divergence ($*10^{-17}$ K m$^{-2}$ s$^{-1}$, color contours), and vectors of $-\left(\dfrac{\partial \overline{T}}{\partial y}, \dfrac{\partial \overline{T}}{\partial x}\right)$ ($*10^{-6}$ K m$^{-1}$) composited for neutral intraseasonal periods and strong easterly waves. Vorticity contour interval is $1*10^{-6}$ $s^{-1}$. Zero vorticity contours are heavy solid lines, and positive (negative) contours are solid (dashed). Phase and number of days included in each composite are shown on the right above each panel. Reference vector is in the upper right of each panel.

motion is forced behind the wave. The horizontal temperature gradient vectors, $-\left(\dfrac{\partial \overline{T}}{\partial y}, \dfrac{\partial \overline{T}}{\partial x}\right)$, at 900 hPa show the advection of positive perturbation 900 hPa vorticity in advance of the wave during early and growing stages. The regions of Q vector convergence at 900 hPa and moistening resulting from the difference of vertically integrated vertical advection and precipitation (Figure 3.5) are located in very similar regions of the wave during early stages indicating possible roles for moistening of the lower and middle troposphere by adiabatic forcing. While this analysis is suggestive, the total EW vertical motion anomaly field is complicated by influence from diabatic

73

heating and difficult to compare to the vertical velocity field implied by the Q-vector analysis. Consistent with this, the 2.5 – 12 day bandpass filtered 900 hPa omega anomalies are nearly in phase with OLR anomalies (not shown).

## 3.6 Forcing of Vorticity by Convection

As can be seen from the EW composites in Figures 3.1, 3.2, and 3.3, EPAC EWs begin as quasi-axisymmetric disturbances and evolve into waves with distinct SW to NE tilts. These horizontal tilts permit the wave to draw energy via barotropic conversion from the background cyclonic shear. The horizontal tilt of EWs and attendant barotropic conversions occur at both low- and midlevels (Rydbeck and Maloney 2014). We hypothesize that the anomalous convective centers in the SW and NE quadrants produce a favored SW to NE tilt by locally generating vorticity in those quadrants through vertical stretching. Vertical stretching has been shown to be important in the vorticity budget of EWs in the west Pacific (Yanai 1961, Lau and Lau 1992) and Caribbean (Yanai and Nitta 1967), particularly at low levels.

The vertically integrated EW vorticity budget can be expressed as:

$$\left[\frac{\partial \zeta_p}{\partial t}\right]' = -\left[v_h \bullet \nabla_h(\zeta_p + f)\right]' + \left[(\zeta_p + f)\frac{\partial \omega}{\partial p}\right]' + \left[\nabla_h \bullet (\zeta_h \omega)\right]' + R \quad (4)$$

where the local change of the vertical component of vorticity on the left hand side results from horizontal vorticity advection, vorticity stretching/horizontal convergence of vertical vorticity, and effects of vertical motion on horizontal vortex lines, respectively, on the right hand side. The residual, R, includes processes that affect vorticity that are not represented in the other terms in equation (4) such as boundary layer friction, cumulus convection, other subgrid-scale processes, and any errors in the calculation of the

74

terms. The vorticity budget is integrated from 1000 hPa to 700 hPa to better capture the mechanisms modulating vorticity at low-levels, specifically the low-level convergence induced by convection that may lead to vorticity stretching. All terms are anomalies obtained by applying a 2.5 – 12 day bandpass filter to the total terms.

In investigating the vorticity budget terms for neutral intraseasonal periods, we focus on the processes that perturb the initially quasi-axisymmetric vortex into one with a distinct SW to NE horizontal tilt, and processes that help to maintain a tilted disturbance. Similar to previous studies on the vorticity budget of EWs in the Pacific and Caribbean (Yanai 1961, Yanai and Nitta 1967, Lau and Lau 1992), horizontal vorticity advection (top right panel of Figure 3.14) is the leading contributor to the overall tendency of EW vorticity anomalies (top left panel of Figure 3.14). The strong quadrature relationship of the vorticity tendency resulting from horizontal advection with the vorticity anomalies suggests that advection is largely responsible for the wave's northwestward propagation but does not maintain or grow vorticity anomalies.

The contribution of the vorticity tendency not resulting from horizontal advection is shown in the bottom left panel of Figure 3.14. Processes included in this term are stretching, tilting, vertical advection, and processes not explicitly resolved in the budget. These processes maximize approximately 1/8 wavelength ahead of the EW and thus contribute both to the propagation and amplification of the wave. Grid-scale stretching of the vertical component of vorticity is shown in the bottom right panel of Figure 3.14. Unlike the horizontal advection of vorticity, the positive portions of the vertically integrated stretching term are largely in phase with the wave, directly support vorticity anomalies, and help to maintain a tilted wave structure. Stretching integrated below 700

hPa during phase 7 maximizes in the SW and NE quadrants of the wave and is greater than .018 s$^{-1}$ 12hrs$^{-1}$. The dotted solid line along the EW indicates the location of the vorticity stretching cross-section averaged over a 1.5° width that is shown in Figure 3.15.
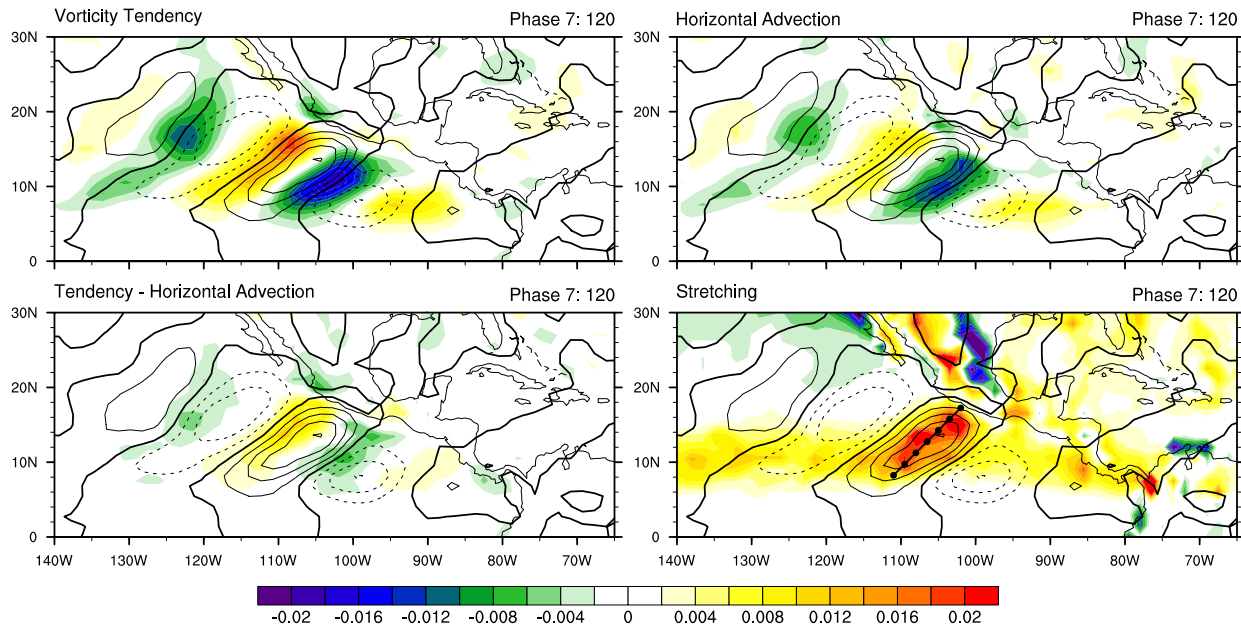


Fig. 3.14 Composite overlay of 2.5 – 12 day bandpass filtered 700 hPa relative vorticity (*10$^{-6}$ s$^{-1}$, line contours) with easterly wave vorticity tendency (s$^{-1}$ 12 hours$^{-1}$, top left), horizontal vorticity advection (s$^{-1}$ 12 hours$^{-1}$, top right), vorticity tendency – horizontal vorticity advection (s$^{-1}$ 12 hours$^{-1}$, bottom left), and vorticity stretching (s$^{-1}$ 12 hours$^{-1}$, bottom right) for phase 7 of neutral intraseasonal periods. Zero relative vorticity contours are heavy solid lines, and positive (negative) contours are solid (dashed). Phase and number of days included in each composite are shown on the right above each panel. Solid dotted black line in the bottom right panel indicates where the vertical cross-section is taken.

Stretching in the mature wave of phase 7 is strongly preferred in low-levels of the SW and NE quadrants (Figure 3.15). Whereas stretching located in the center of the wave leads to a more axisymmetric growth of the vorticity, the stretching in the NE and SW peripheries of the wave supports a horizontal elongation of the wave. The stretching in phase 7 is collocated with regions of strong negative OLR anomalies representative

of deep convection. We propose that local low-level vorticity stretching (also may be referred to as local vorticity convergence) resulting from deep convection preferentially occurring in the SW and NE quadrants of EWs supports the observed horizontal tilt of the wave. The preferred horizontal tilt initializes when the wave is weak with the OLR maximum located in the SW quadrant (see phases 3 and 4 of Figure 3.1), and the tilt intensifies as a complimentary OLR maximum develops in the NW quadrant (see phases 5 and 6 of Figure 3.1). Such tilts are critical for the wave to derive energy from the background horizontal wind shear via barotropic conversion.
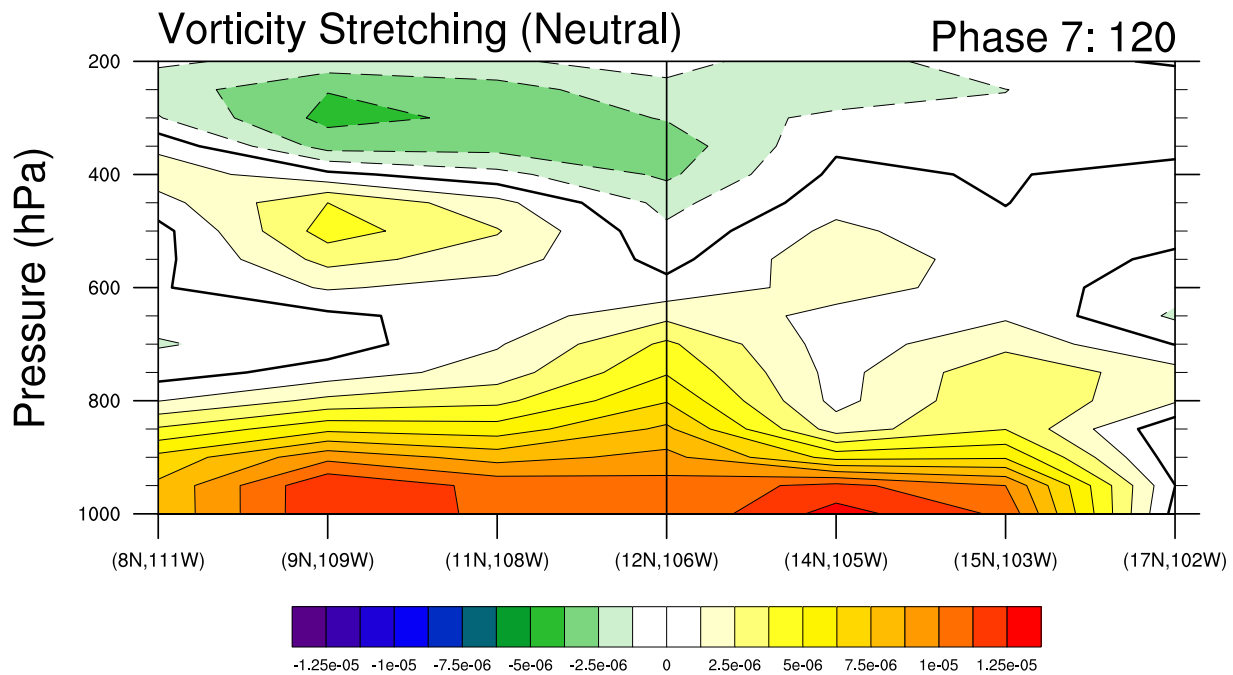


Fig. 3.15 Vertical cross-section composite of easterly wave vorticity stretching ($s^{-1}$ 12 hours$^{-1}$) for phase 7 of neutral intraseasonal periods along the line shown in bottom right panel of Figure 3.14. Phase and number of days included are shown on the right above the panel.

EW barotropic conversions and attendant tilts are known to occur at midlevels as well as low-levels. The effects of vertical motion on horizontal vortex lines during phase 7, along the same cross-section shown for vertical stretching, have local maxima exceeding $1.5*10^{-6}$ s$^{-1}$ 12hr$^{-1}$ in the middle and upper troposphere in both the SW and

NE quadrants and thus result in EW horizontal tilts in regions above the strongest vorticity stretching (not shown). Lastly, the residual of the budget in the lower troposphere is overwhelmingly negative. The exclusion of boundary layer friction in the vorticity budget is likely the leading contributor to the residual there. A budget residual maximum in the middle troposphere of $1.2 *10^{-6}$ $s^{-1}$ $12$ $hr^{-1}$ suggests a possible role for unresolved processes, such as cumulus convective effects, for increasing middle tropospheric vorticity (not shown).

## 3.7 Conclusions

EWs in the EPAC have preferred areas of convection that evolve as the wave grows. Beginning as quasi-axisymmetric disturbances, the waves obtain strong SW to NE tilts by maturation. In this study, we hypothesize that preferred regions of EW convection located in the SW and NE quadrants of the wave force local vorticity stretching and elongate the wave horizontally in those directions.

Regions of anomalous convection are supported by collocated column integrated moisture anomalies. While evaporation opposes the buildup of moisture early in the wave's life cycle, horizontal advection overwhelmingly dominates the moisture budget of the waves. EWs propagating along the mean moisture gradient of the ITCZ advect moist air into the SW quadrant of the waves. The resulting column moisture anomaly maximum in that quadrant early in the wave's life is supportive of coincident OLR anomalies. Later in the life cycle as the wave moves northwestward, convection in mature waves is supported by moisture anomalies resulting from the advection of perturbation moisture anomalies by the mean zonal wind. At the same time, advection of mean moisture by the perturbation meridional winds in the SW quadrant declines as

the wave moves away from the strong moisture gradient on the equatorward side of the ITCZ. In the moisture budget, vertical advection and precipitation largely cancel at the wave axis, but moistening by vertical advection exceeds drying by precipitation ahead of the wave. Behind the wave, precipitation exceeds vertical advection resulting in drying, similar to easterly waves observed during GATE (Thompson et al. 1979). This signal is consistent with adiabatic forcing of rising motion ahead of the wave axis and sinking motion behind.

EWs are strongly modulated by the background fields through which they propagate. Previous studies have shown that EW kinetic energy and available potential energy are a strong function of the intraseasonal background state of the atmosphere (Maloney and Hartmann 2001, Aiyyer and Molinari 2008, Rydbeck and Maloney 2014, Crosbie and Serra 2014). In this study, we suggest that intraseasonal variations of EW moisture that influence convective instability, as shown with a diluted CAPE calculation of a saturated plume, regulate the convective intensity of EWs. EW diluted CAPE anomalies during easterly intraseasonal periods are reduced by half compared to westerly intraseasonal periods and as a result stifle EW convection anomalies. Regardless of intraseasonal phase, the spatial relationship between EW convection and circulation anomalies exhibits strong variations as a function of EW phase.

EW vorticity anomalies are propagated by horizontal advection and intensified by vertical stretching. The vertical stretching is coincident with regions of strong OLR anomalies suggesting that deep convection modifies the vorticity structure of the EW, namely an elongation of the wave's circulation from the SW to the NE. The tilt of the wave from the SW to the NE is critical to the increase of EW kinetic energy by

barotropic conversion cited in Rydbeck and Maloney (2014). EWs during easterly intraseasonal periods are, at times, not strongly convectively coupled and much slower to develop favorable horizontal tilts and corresponding EW kinetic energy increases. The local vorticity increases at low levels in the SW and NE quadrants of maturing waves suggests a role for shallow and deep convective heating profiles while vorticity increases at midlevels are likely produced by stratiform heating profiles.

More vigorous synoptic-scale vortices have been shown to favor enhanced tropical cyclogenesis in the EPAC (Davis et al. 2008). Hence, in agreement with previous work, EWs during low-level westerly (easterly) periods that develop more (less) quickly are associated with enhanced (suppressed) periods of tropical cyclogenesis (Maloney and Hartmann 2000, Davis et al. 2008). The vast majority of perturbation available potential energy generation within EPAC EWs and subsequent conversion to perturbation kinetic energy is associated with convective diabatic heating (e.g. Serra et al. 2010, Rydbeck and Maloney 2014). Because of this relationship, strongest considerations are typically placed on convective intensity when forecasting EW strengthening. The results presented herein suggest that a secondary and previously unidentified effect of convection is to tilt the wave in the horizontal, allowing the wave to draw energy from the background cyclonic wind shear. The tilt of the wave results from the distribution of convection within the envelope of EW vorticity. As a result, emphasis should likewise be placed on the horizontal arrangement as well as the intensity of convection within EPAC EWs when considering EW growth patterns.

**CHATPER 4 In-situ Initiation of East Pacific Easterly Waves in a Regional Model**

**4.1 Introduction**

Tropical cyclones observed in nature always originate from pre-existing atmospheric disturbances. In the east Pacific (EPAC), the most prevalent precursor disturbances are easterly waves (EWs) that have previously been hypothesized to propagate from Africa (Simpson et al. 1969; Frank 1970; Shapiro 1986; Avila and Pasch 1992; Molinari et al. 1997). This study proposes a new mechanism by which EWs are initiated locally in the EPAC. Mechanisms of in-situ initiation of EWs and tropical cyclones (TCs) in the EPAC have previously been suggested, such as ITCZ breakdown (Ferriera and Schubert 1997), barotropically unstable gap wind jets (Mozer and Zehnder 1996), inertial instabilities arising from cross-equatorial pressure gradients (Toma and Webster 20010a,b), and growth of vortices by barotropic conversion in the presence of a suitable EPAC basic state (Maloney and Hartmann 2001; Hartmann and Maloney 2001). African EWs have also been suggested as being responsible for remotely forcing a large number of EPAC EWs (i.e. Blake and Pasch 2010, Blake and Kimberlain 2013). The mechanism proposed herein is distinct from these previous ideas, but not exclusive of them since they may compliment one another. We hypothesize that diurnal convective forcing originating in the Panama Bight (Mapes et al. 2003a) is able to seed EWs in the EPAC through a process of upscale vorticity organization.

EWs are off-equatorial low-pressure convective regions that migrate westward in tropical easterlies between 5 – 11 m/s. EWs have been characterized by maximum meridional wind anomalies near 600 – 850 hPa, wavelengths of 2000 – 4400 km, and

periods of 3 – 5 days (Tai and Ogura 1987, Serra et al. 2008). Rydbeck and Maloney (2014, Chapter 2 of this dissertation) showed that EWs in the EPAC are strongly energized in the middle and lower troposphere due to conversions of perturbation available potential energy to perturbation kinetic energy and barotropic conversions. Rydbeck and Maloney (2015, Chapter 3 of this dissertation) also showed that the distribution of convection around the EW favored a southwest to northeast horizontal tilt of the wave that is necessary to support barotropic conversions that energize the wave. In building on this previous work, the present study investigates the origins of EW vorticity anomalies in the EPAC.

EWs have been actively identified and recorded near and through the Intra-Americas Seas since at least 1887 (Dunn 1933). However, the salient dynamical and convective features of EWs are often difficult to track across the tropics. When the convective signals and wind circulations of EWs are undetectable, as often occurs over the dry and hostile Caribbean, many observational studies have used subjective measures to track EWs. For example, some studies have assumed a continuous EW trajectory across the Atlantic and Caribbean, even when the wave is not observable (e.g. Avila and Pasch 1995, Beven et al. 2005).

However, Molinari et al. (1997) questioned the existing paradigm of the EW continuum across the tropical Atlantic into the EPAC, suggesting that EWs can be characterized as dispersive Rossby wave packets. Under this consideration, EWs would dissipate in the absence of deep convection before reaching the Caribbean, Gulf of Mexico, or EPAC. The western tropical Atlantic and the western Caribbean are regions of significant EW lysis (Thorncroft and Hodges 2001, Serra et al. 2010). Although some

EWs do clearly traverse the Atlantic into the EPAC (i.e. Shapiro 1986), many studies have suggested that the primary energy sources for EWs in the EPAC are local to the EPAC (Maloney and Hartmann 2001, Aiyyer and Molinari 2008, Serra et al. 2010, Rydbeck and Maloney 2014). If a large number of EWs do fully decay in the Atlantic and Caribbean in the absence of deep convection, the initiation of in-situ EWs would be necessary to support the observed number of EPAC TCs.

Correlations of tropical cyclogenesis between the EPAC and Atlantic do not suggest a strong relationship between precursor disturbances, predominantly EWs, in the two basins. Frank and Young (2007) showed that enhanced TCs activity in the Atlantic is not compensated by significantly reduced activity in the EPAC. The insignificant correlations suggest that a reduction in precursor disturbances due to their role in Atlantic tropical cyclogenesis does not limit EPAC cyclogenesis due to a dearth of disturbances, a result also corroborated by Collins (2010). To note, EWs have been shown to seed storms in the Atlantic and effectively separate from the TCs after genesis and continue independently propagating westward (Tyner and Aiyyer 2012). However, instances of EWs separating from the parent TCs are rare.

Hartmann and Maloney (2001) suggested that EPAC EWs could be generated in-situ using a simple barotropic model forced with vorticity noise. In the model, the EWs generated are similar in horizontal structure, amplitude, and eddy kinetic energy distributions to those from reanalysis. Their results suggest that in-situ EW initiation and growth in the EPAC is possible given sufficient noise forcing and a favorable background state. The EW energy budget analysis of Rydbeck and Maloney (2014) suggested that a finite amplitude disturbance could develop into a robust EW in

approximately 1.5–2.5 days from barotropic and perturbation available potential energy to perturbation kinetic energy conversions, supporting the contentions of Hartmann and Maloney (2001).

Compared to other global regions of TCs development, EPAC tropical cyclogenesis is not strongly dependent on precursor disturbances propagating into the region (Schreck et al. 2012). This is highlighted by the modeling study of Toma and Webster (2010b) wherein synoptic frequency variability, including EWs, was filtered from the lateral boundaries of a regional model situated over the EPAC. In their study EPAC EWs developed in-situ in the absence of EW signals propagating westward from the Atlantic Ocean and Caribbean Sea. The local development of EPAC EWs resulted from inertial instabilities of the ITCZ generated by the advection of anticyclonic vorticity from the southern hemisphere into the northern hemisphere.

Velasco and Fritsch (1987) note a direct relationship between several EPAC tropical cyclogenesis occurrences and mesoscale convective vortices associated with mesoscale convective complexes originating over South America. As an example, TC Elida formed in the EPAC on July 11, 2008 approximately 315 nautical miles south-southeast of Puerto Angel, Mexico and eventually reached hurricane strength on July 14, 300 nautical miles southwest of Manzanillo, Mexico. TC Elida eventually reached a peak intensity of 90 knots on July 16 and gradually weakened to below hurricane strength on July 18 (Blake and Pasch 2010). As previously mentioned, most TCs in the EPAC are said to form in association with waves propagating from Africa. TC Elida did not support this paradigm in that the cyclone formed in association with a tropical wave that originated locally near Central America.

As can be seen in a time-longitude diagram of EPAC 700 hPa vorticity and precipitation in Figure 4.1, no strong predecessor vorticity or precipitation signals existed outside the EPAC prior to the formation of TC Elida. The tropical wave that led to the formation of TC Elida is only traceable back to the coast of Central and South America, in the region known as the Panama Bight. Westward propagating mesoscale convective systems with diurnal periods are well known to routinely occur in the Panama Bight (Mapes et al. 2003a.) and are evident in both precipitation and vorticity fields in Figure 4.1. Some of these diurnal pulses are stronger than others. The precise origin of the EW responsible for seeding TC Elida is unknown, but a hypothesis on the formation of EWs near the Panama Bight is presented in this paper.
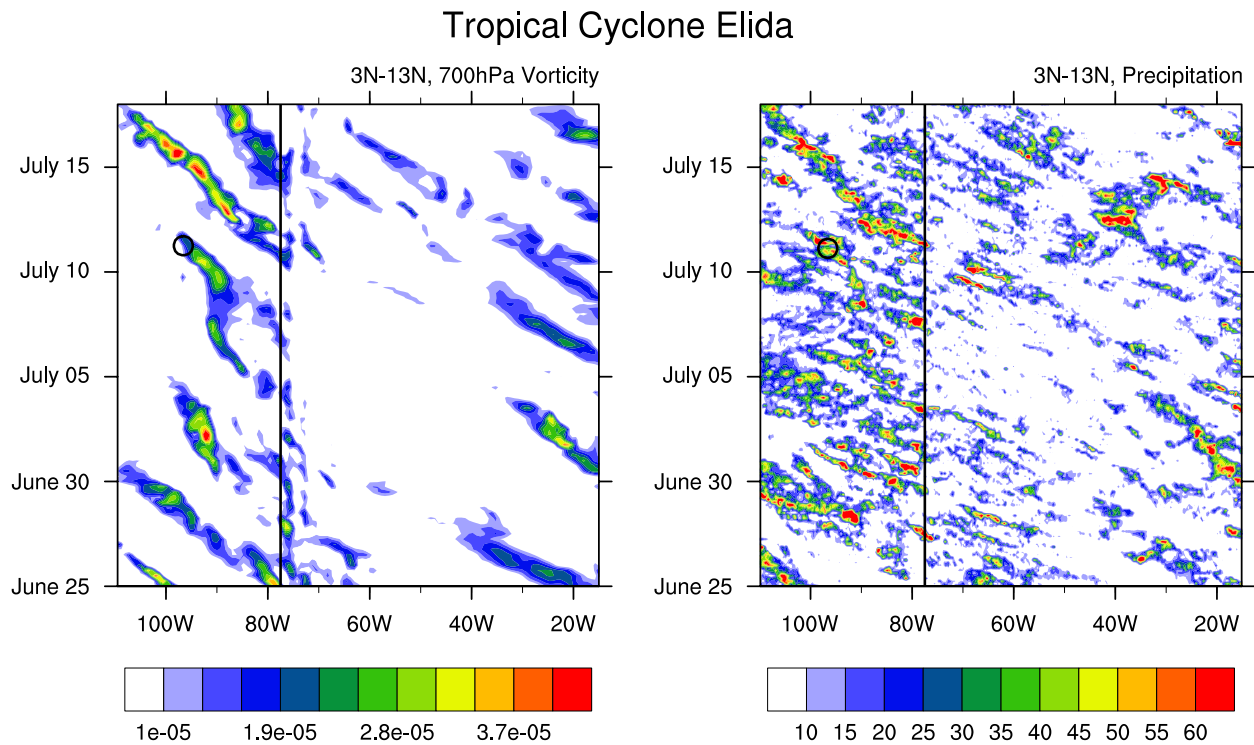
## Tropical Cyclone Elida



Fig. 4.1 Time-longitude sections of 700-hPa relative vorticity (s$^{-1}$; left panel) and precipitation (mm day$^{-1}$; right panel) averaged from 3N-13N are shown. The vertical black line indicates the longitude of the Pacific coast of South America. The black circle shows the location and time of genesis for tropical cyclone Elida.

One goal of the current study is to investigate the robust forcing associated with the diurnal pulsing of convection near the Panama Bight and its role in EW formation. We hypothesize that westward propagating diurnal variability originating near the Panama Bight helps to initiate and grow EPAC EWs. Many previous studies have noted that EPAC EWs appear to originate near the coasts of Panama and Columbia, with little to no preceding signals located in the Atlantic Ocean (Nitta and Takayabu 1985, Tai and Ogura 1987, Serra et al. 2008, Toma and Webster 2010b, Serra et al. 2010, Rydbeck and Maloney 2014). In that same region (i.e. the coastal region just west of the Columbian Andes), a large number of mesoscale convective complexes are known to occur during boreal summer (Velasco and Fritsch, 1987). In fact, that same region has been shown to have the highest occurrence of organized deep convection on the planet based on the Highly Reflective Cloud dataset (Mapes et al. 2003a), where convective clusters found in the Panama Bight propagate westward diurnally (Mapes et al. 2003a). In a regional model, convection is initiated when temperature anomalies associated with westward propagating gravity waves cool a warm capping layer near 850mb, allowing the convective available potential energy of the column to be realized (Mapes et al. 2003b, Warner et al. 2003). The gravity waves and attendant convection were found to be strongly dependent on the presence of the Andes Mountains in Columbia in a regional model. The westward propagating mesoscale convective systems in the Panama Bight ceased when the mountains were removed, a fact of which we will take advantage in sensitivity tests in the current study.

This study will use a regional model to test the remote versus local forcing of EPAC EWs. First, we examine the roles of EWs propagating from West Africa and the

Atlantic to the tropical synoptic variability of the EPAC. In suppressing external EW variability, insights into the magnitude and regularity of the in-situ generation of EPAC EWs are gained. Next, the degree to which strong diurnal and westward propagating mesoscale convective systems in the Panama Bight seed EWs is investigated by suppressing the diurnal precipitation variability in the model.

The difficulty in objectively tracking EWs, particularly waves devoid of deep convection, in observational case studies and the coarseness of global reanalyses in studying the physical processes that regulate EWs motivate the use of a regional model to study the climatology of EWs in the EPAC under various prescribed conditions. Section 4.2 describes the regional model used for this study, the methods for suppressing remote and local forcing of EWs from the model, and the reanalysis and observed data used for model comparison. Section 4.3 examines the model simulations to better understand the sensitivity of EPAC EWs to local and remote forcings. Section 4.4 expands on this process-level investigation of in-situ EW generation by analyzing the middle tropospheric EW vorticity budget, with emphasis on the upscale organization of diurnal anomalies. Section 4.5 presents some discussion and conclusions on this chapter.

## 4.2 Model Setup and Simulations

The Advanced Research WRF (WRF) version 3.4.1 (Skamarock and Klemp 2008) is used to investigate EWs in this study. Previous studies have successfully employed WRF to study tropical phenomena in regional climate simulations (e.g. Tulich et al. 2011, Mallard et al. 2013, Jin et al. 2013, Alaka 2014, Kim et al. 2015). By using a regional model, we have the capability to modify the boundary forcing. Specifically, the

boundary forcing of the model can be modified to remove variability associated with EWs from propagating into the domain. The sensitivity of the model to the modified boundary forcing proves insightful to our understanding of the local development of EWs in the EPAC.

Many different model settings were tested in WRF to find the most suitable set to properly simulate tropical synoptic variability and the mean atmosphere in the EPAC. The settings that performed this best and are utilized in all model simulations include the Kain-Fritsch cumulus parameterization (Kain 2004), WRF Single Moment 6-class microphysics scheme (Lim and Hong 2006), Community Atmosphere Model (CAM) (Collins et al. 2004) shortwave and longwave radiation, Noah land surface model, and the Yonsei University (YSU) (Hong et al. 2006) planetary boundary layer parameterization with modified surface bulk drag and enthalpy coefficients. Month long sensitivity simulations were performed utilizing various combinations of parameterizations, land surface models, and input data to determine the best representation of the EPAC mean state and tropical synoptic variability. These sensitivity tests included the utilization of the Grell 3 cumulus parameterization, WRF double moment 6-class microphysics scheme (Lim and Hong 2010), Thompson microphysics scheme (Thompson et al. 2008), rapid update cycle land surface model, National Centers for Environmental Prediction (NCEP) real-time global hi res sea surface temperatures, and NCEP's global forecast system final tropospheric analyses boundary forcing (Thiébaux et al. 2003). Many of the combinations of parameters generated excessive amounts of mean precipitation or underrepresented EPAC EW activity.

Model simulations are conducted for the summer seasons (May – November) of 2000-2009 using lateral and boundary forcings from the 0.75° ERA Interim reanalysis dataset (Dee et al. 2011). SSTs and lateral boundary conditions are updated every 6 hours. The outer and inner nest grid spacings are 54 km and 18 km, respectively, and encompass much of the Caribbean, Gulf of Mexico, and EPAC warm pool, as shown in Figure 4.2. Similar grid spacing has been shown to adequately resolve tropical convective variability using the Kain-Fritsch cumulus parameterization in other studies (i.e. Tulich et al. 2011 and Mallard et al. 2013). The model has 31 vertical levels with the top at 50 hPa. The inner domain is one-way nested within the parent domain.
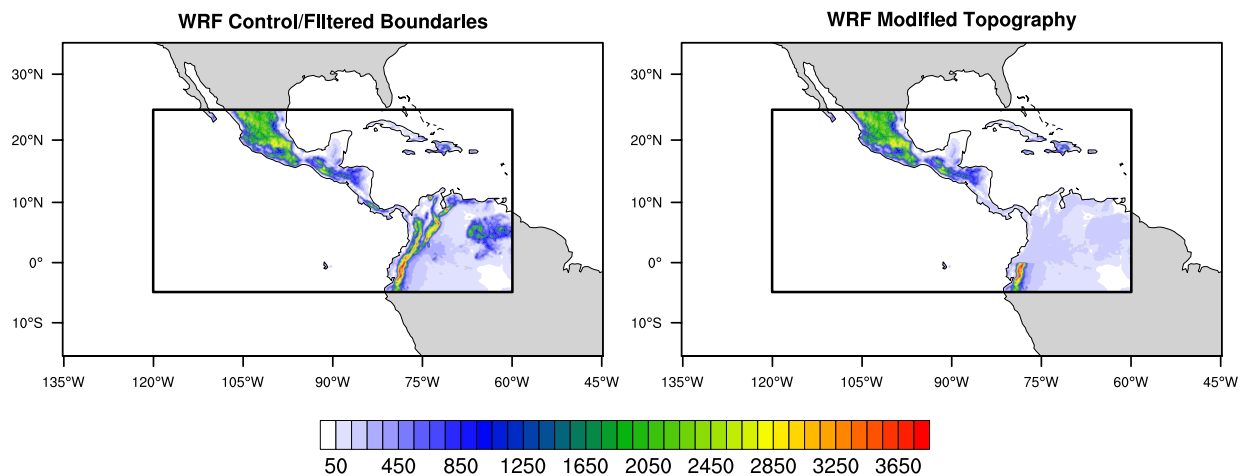


Fig. 4.2 Parent and nested domains of the WRF control/filtered boundaries (left panel) and the WRF modified topography (right panel) simulations are shown. Terrain height (m; color contours) of the nested domain is shown for the respective simulations.

Three sets of simulations are performed using the WRF-ARW: control, filtered boundary, and modified topography simulations. The control simulation is run as previously described, with no modifications. For the filtered boundary simulation, the lateral boundary forcing of the parent domain are filtered to remove easterly propagating synoptic variability in the 2.5 – 12 day frequency band that includes EWs propagating

89

across the Atlantic from west Africa. Geopotential height, temperature, horizontal wind, and moisture anomalies located in the wavenumber-frequency domain defined by 2.5 to 12 day frequencies and negative wavenumbers are removed at the boundaries throughout the atmospheric column along with surface pressure anomalies. By not allowing these anomalies to enter the model domain, the tendency of EWs to initiate in-situ can be evaluated.

In the modified topography simulation, topography associated with the forcing of westward propagating diurnal mesoscale convective systems in the Panama Bight is modified such that elevations do not exceed 400 meters over particular areas in the nested domain. The terrain height for the control and modified topography simulations are shown in Figure 4.2. Modifying the topography is similar to the approach used in Mapes et al. (2003) to reduce the diurnal rainfall variability in the Panama Bight. The success of this approach at minimizing diurnal variability in this region is examined later. The modified topography simulation is not sensitive to reasonable changes in the terrain height threshold. However, it is sensitive to the areal extent of the flattened terrain. Diurnal convective systems are present in both northern South America and portions of Central America in the model and require the flattening of terrain in both regions to sufficiently suppress diurnal convective activity to the east of the EPAC warm pool.

Many of the model simulations are compared with 6-hrly 0.75° ERA Interim reanalysis fields as well as 6-hrly 0.25° 3B42 TRMM precipitation data from the same summer seasons as the model integrations.

**4.3 Modeling Results**

EPAC EWs have been observed to be sensitive to changes in the background state of the atmosphere (e.g. Molinari and Vollaro 2000, Maloney and Hartmann 2001, Aiyyer and Molinari 2008, Rydbeck and Maloney 2014,2015, Crosbie and Serra 2014). Therefore, in order to properly simulate EPAC EWs, the background state must be reasonably represented in the model. Examples of important background features include the Caribbean low-level jet and its extensions into the north EPAC through the mountain gaps of Central America, location and intensity of the ITCZ, low-level westerly winds in the EPAC warm pool, and meridional shear of the mean zonal winds. These features of the mean state have been suggested to be dynamically and thermodynamically important to the initiation and maintenance of EWs as well as TCs in the EPAC, and some aspects are discussed here to confirm the model's suitability for simulating EWs.

The mean precipitation and 10 meter surface winds for all model simulations and ERA Interim /TRMM data are shown in Figure 4.3. In ERA Interim reanalysis and TRMM observations (top left panel of Figure 4.3), a precipitation maximum of 16 mm/day is located near the Panama Bight region (3-7°N, 76-79°W), just off the Pacific coasts of Columbia and Panama. The maximum extends to the west-northwest and defines the boreal summer Intertropical Convergence Zone (ITCZ) in the EPAC. Much of the ITCZ is embedded within a westerly component of the surface flow. The westerly component is generally stronger near the Central and South American coasts. A weakening of the ITCZ on its northern flank is apparent near the Costa Rica dome (11°N, 88°W), a region of strong ocean upwelling due to Ekman divergence forcing on the cyclonic shear side

of the Papagayo jet that results in anomalously cooler SSTs (Chelton et al. 2000a,b). The Papagayo jet is often referred to as an extension of the easterly Caribbean low-level jet across Lake Nicaragua that is still well defined in the surface winds.

## Mean Precipitation and Surface Winds
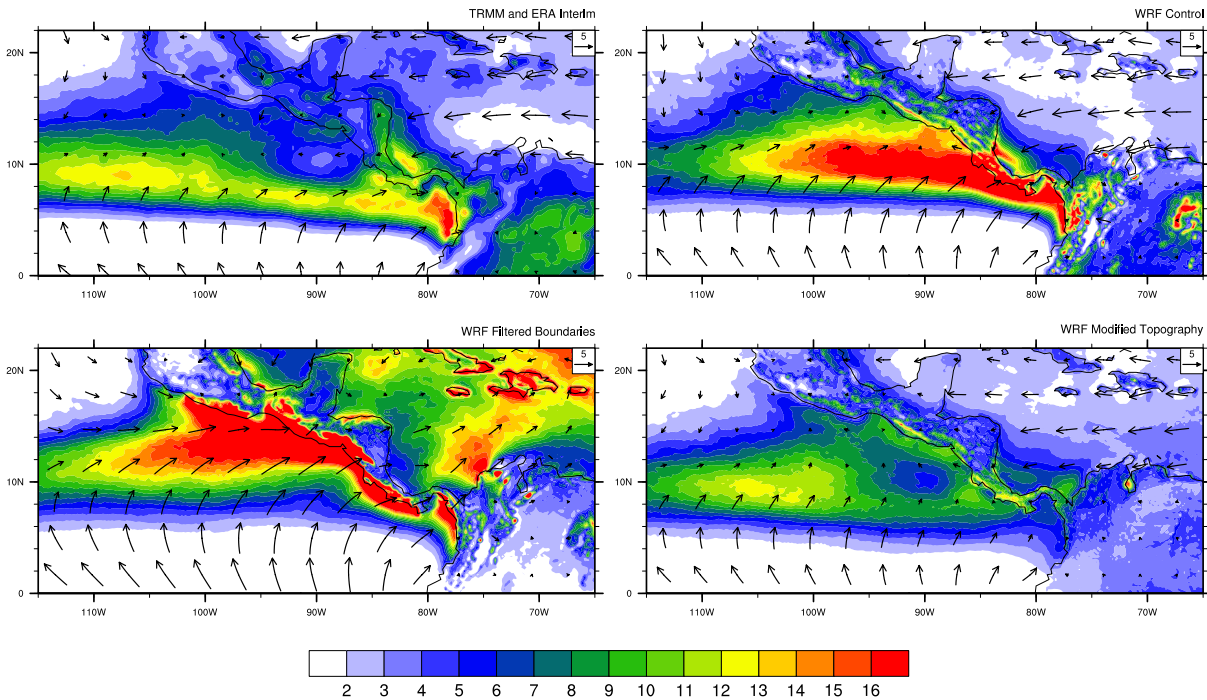


Fig. 4.3  Mean precipitation (mm day$^{-1}$; color contours) and 10m surface winds (m s$^{-1}$; wind vectors)  for the May-Nov 2000-2009 period for ERA Interim and TRMM (top left), WRF control (top right), WRF filtered boundaries (bottom left), and WRF modified topography (bottom right) are shown. Reference wind vector is located in the upper right corner of each panel.

The surface winds and precipitation for the WRF control (top right panel of Figure 4.3), filtered boundary (bottom left panel of Figure 4.3), and modified topography simulations (bottom right panel of Figure 4.3) are shown as well. The control simulation well represents some basic features of the large-scale precipitation and circulation such as the westerly component of the low-level winds, Caribbean low-level jet, west northwest orientation of the ITCZ, and a local maximum of precipitation in the Panama Bight. However, precipitation rates associated with the ITCZ are 1.5 to 2 times greater

than observed, shifted to the north by a few degrees, and associated with stronger surface winds. In other studies utilizing regional models to study the climatology of the EPAC, similar biases to the ones show herein have been noted (Small et al. 2011, Rydbeck et al. 2013). These biases are more exaggerated in the boundary filter simulation in which precipitation maxima more strongly follow the western coasts of Central America and Mexico. Moreover, the Caribbean low-level jet is no longer well represented in the filtered boundary simulation, as the winds in that region are weak westerlies and southwesterlies. Holton et al. (1971) suggested that the climatological ITCZ was the "locus of the cloud clusters associated with a train of westward propagating wave disturbances". By suppressing westward propagating synoptic variability in this simulation, the climatological ITCZ is consequentially altered. To note, changes in the mean state, including the low-level winds, were also observed in a regional modeling study in which intraseasonal variability was removed from the boundary forcing (Rydbeck et al. 2013). This may point to the sensitivity of the climatologically ITCZ in the EPAC to various scales of remote forcing.

Another possibility for the dramatic change of the mean state in the filtered boundary simulation is that by removing westward propagating synoptic variability from the model boundary forcing, the climatological Bermuda High has been modified, resulting in deviations of EW tracks in the region. Moreover, observational studies have shown that submonthly eddies act to dry the tropical EPAC (i.e. Peters et al. 2008). By removing EWs in the filtered boundary simulation, a sink of tropical moisture is also removed. As a result, the Intra-Americas Seas might be expected to have anomalously large amounts of total precipitable water supportive of enhanced precipitation. The

climatological state in the control and filtered boundary simulations do show departures from the observed climatology. However, because they share many of the same biases and their basic states in the EPAC are not too dissimilar, we feel that there is still value in contrasting the generation and maintenance of EWs in the EPAC between the two simulations.

Perhaps the best representation of the EPAC mean state is captured in the WRF modified topography simulation in which the topography through portions of Central and South America are capped at 400m (see right panel of Figure 4.2). The Caribbean low-level jet is well represented, the precipitation rates are comparable to those observed from TRMM, and the precipitation hole near the Costa Rica dome is resolved. A prominent difference between TRMM and the WRF modified topography simulation is that the local precipitation rate maximum in the Panama Bight is absent. This is an expected result from modifying the topography and eliminating much of the diurnal convective activity in the region (see Figure 4.4).

The suppression of diurnal convective activity is further confirmed by analyzing composite time-longitude plots of the diurnal cycle of precipitation averaged from 3° – 9°N in Figure 4.4. The dashed line in each panel indicates the 15 m s$^{-1}$ phase speed. The WRF control simulation captures the westward propagating and diurnally oscillating rain rates observed in TRMM (top left and bottom panel of Figure 4.4), although of smaller magnitude. The diurnal cycle of precipitation in the Panama Bight for the WRF control simulation shares a similar gravity wave propagation speed to that of observations. However, the most intense rain rates occur between midnight and noon local time in observations while in the WRF control simulation the most intense rain

rates occur between midnight and the early afternoon. The regional modeling simulation of Warner et al. (2003) used to analyze the diurnal patterns of rainfall in northwest South America also underestimates the magnitude of the precipitation rates in the Panama Bight while still capturing the overall pattern of diurnal rainfall. In the WRF modified boundary simulation, composite precipitation rates are dramatically reduced when compared to the control simulation and TRMM. There is no evidence of precipitation propagation in the WRF modified topography simulation.
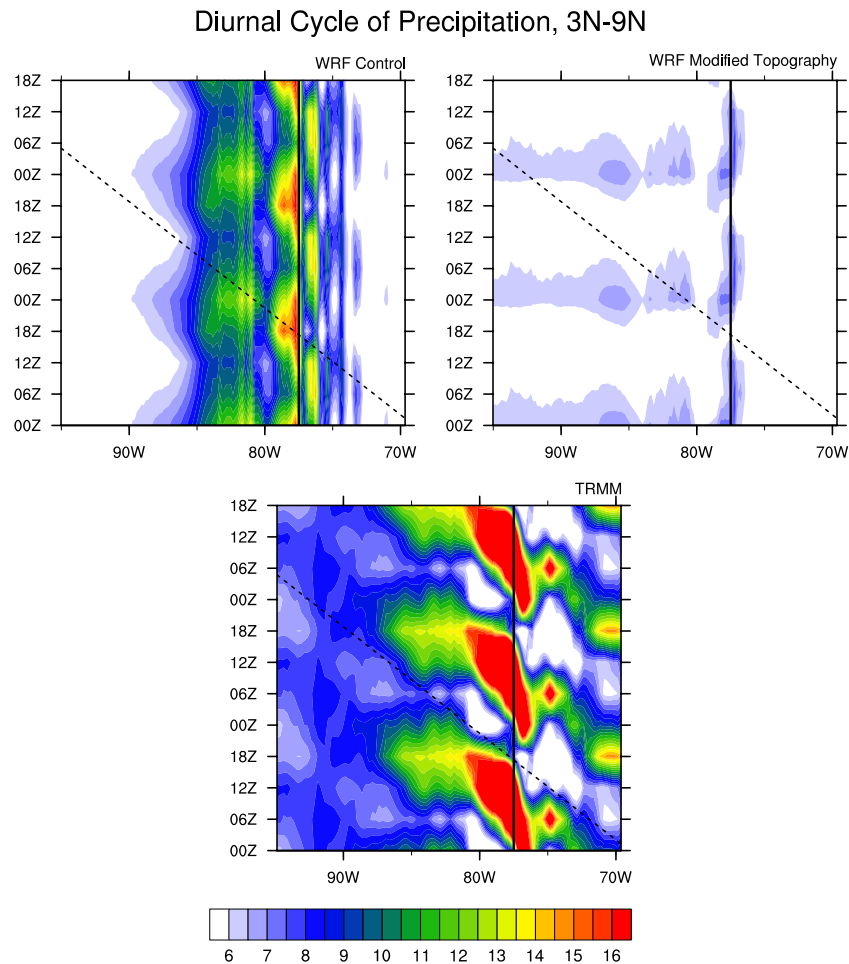


Fig. 4.4 Time-longitude sections of mean precipitation rate (mm day$^{-1}$) for the diurnal cycle averaged from 3° – 9°N for the WRF control simulation (top left), WRF modified topography simulation (top right), and TRMM (bottom). Solid black line indicates Pacific coast of South America. Dashed lined indicates a phase speed of 15 m s$^{-1}$. The plots are repeated three times for clarity.

The WRF control simulation shows EPAC westward propagating synoptic variability with comparable or higher amplitude to observations, as can be seen in a plot of 550hPa relative vorticity averaged from 3°N -11°N during the summer (May-Nov) of 2008 (top row of Figure 4.5). Model winds have been fitted to the reanalysis grid before relative vorticity is computed such that the vorticity magnitudes may be uniformly compared. Synoptic waves including both EWs and TCs with similar phase speeds and durations are easily seen when comparing the control simulation and ERA Interim. Similar behavior is consistently observed when comparing others summer seasons. The synoptic waves in the WRF control simulation are stronger than those in ERA Interim, both intensifying more quickly and maintaining their intensity for longer periods.

A contributing factor to the hasty intensification of EWs in the WRF control simulation is that the waves are associated with much stronger convective anomalies than in observations (figure not shown), especially near the coasts of Central America and Mexico. The downstream development of EWs over Africa has been strongly linked to the intensity of upstream convective anomalies (Thorncroft et al. 2008). In the WRF control simulation, convective anomalies associated with developing EWs are stronger earlier in the life cycle than in observations, possibly leading to a more sudden intensification and greater amplitude than observed waves (see also Fig. 4.7).

Relative vorticity averaged from 3°-11°N for the filtered boundary and modified topography simulations are shown, respectively, in the bottom row of Figure 4.5. In the filtered boundary simulation, synoptic-scale activity is dramatically reduced during the middle of the May-Nov 2008 period, although strong vorticity signals are still prominent in the early and late stages of the simulation. These results suggest that while EW

activity is reduced in the filtered simulation when African EW activity is filtered from the

boundaries, strong synoptic-scale disturbances are still able to form in their absence. In
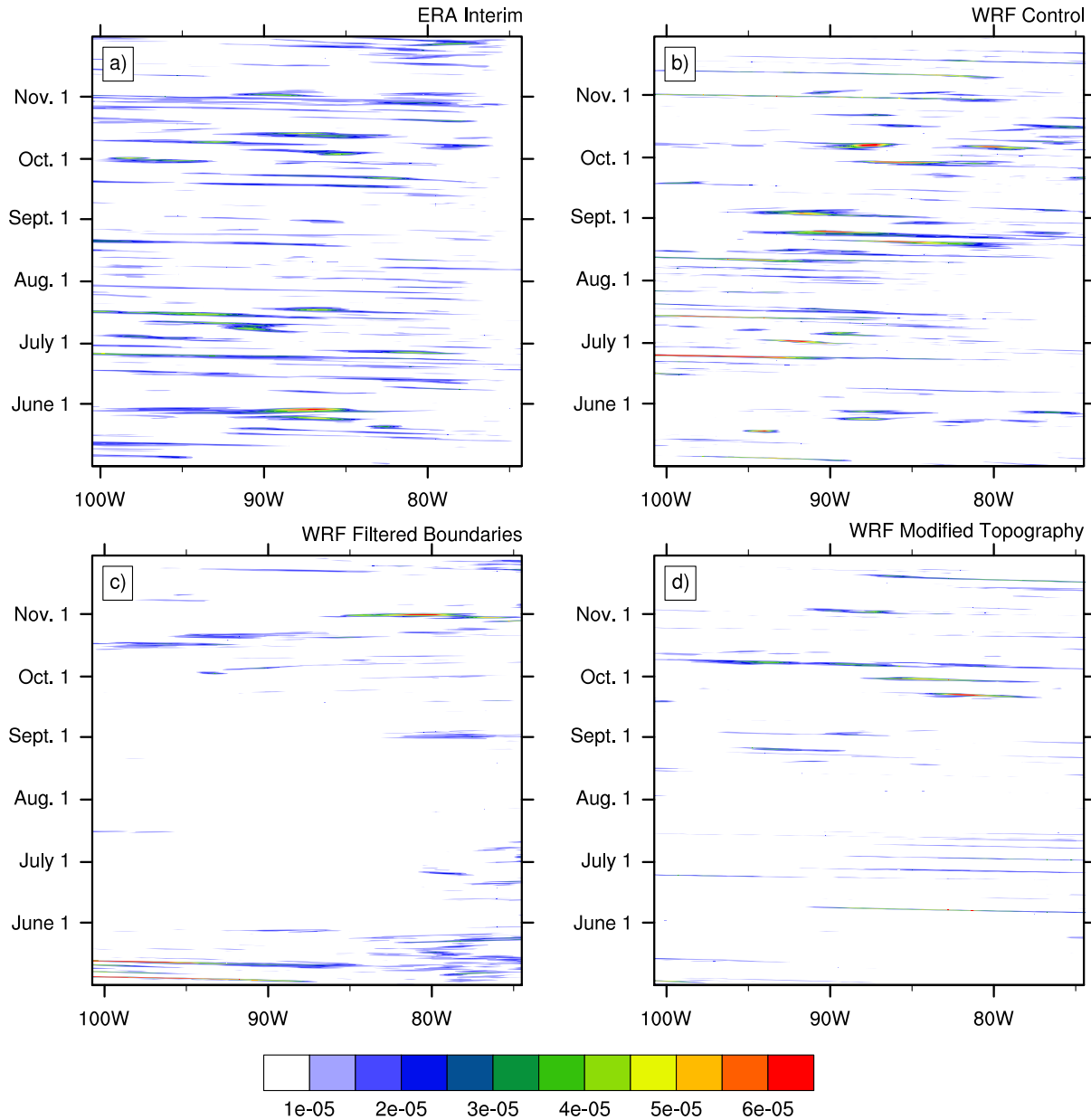
## 550hPa Vorticity, 3N-11N



Fig. 4.5 550-hPa relative vorticity averaged from 3°N – 11°N is shown as a function of time versus longitude for ERA Interim (top left), WRF control (top right), WRF filtered boundaries (bottom left), and WRF modified topography (bottom right) for May-Nov of 2008. Vorticity in all WRF simulations has been interpolated to the same grid as ERA Interim data.

other words, EWs propagating from Africa are important to the initiation of EWs in the EPAC, particularly when such outside variability is most robust during the heart of boreal summer, but not essential to EW formation, supporting similar conclusions made by Toma and Webster (2010 a,b). When local diurnal rainfall variability near the Panama Bight is suppressed, EW and TC activity in the EPAC is reduced in amplitude and regularity (bottom right panel of Figure 4.5), suggesting that the diurnal variability is important to EPAC EW initiation and maintenance. Thus, in the absence of local diurnal variability and forcing, EWs and TCs in the EPAC are dramatically reduced. The EWs that are present appear to be associated with preexisting disturbances entering from the Caribbean, as can be seen around July 1 and October 1. The bottom row of Figure 4.5 suggests that both remote and local forcings are important to EPAC EWs. The results presented in Figure 4.5 are consistent with the other summer seasons not shown.

The association of EPAC EWs with those in the Caribbean is further examined by performing a lag correlation of 2.5 – 12 day bandpass filtered 550hPa vorticity anomalies between the Caribbean and EPAC over all summer seasons (Figure 4.6). The filtered vorticity anomalies are averaged over a 5°x5° box centered at 9°N, 87°W in the EPAC and 9°N, 64.5°W in the Caribbean. The results are not sensitive to reasonable changes in the longitude but are sensitive to changes in latitude, particularly when only one of the averaging boxes is moved north or south. In the control simulation, positive correlations significant at the 95% confidence threshold are present at -2.25 days, when EW vorticity in the Caribbean leads that in the EPAC. The correlation at lag -2.25 days in the control simulation is weaker than that in ERA Interim suggesting that the control simulation is not as sensitive to remote forcing by preexisting EWs as

observations. As expected no significant correlations are present at any lag in the filtered boundary simulation. Significant positive correlations are present in the modified topography simulation between lags -2 and -3 days. These correlations are approximately twice the value of those occurring at similar lags in the control simulation, suggesting that EWs in the Caribbean are responsible for forcing EWs in the EPAC to a much greater degree when diurnal variability in the Panama Bight is suppressed.



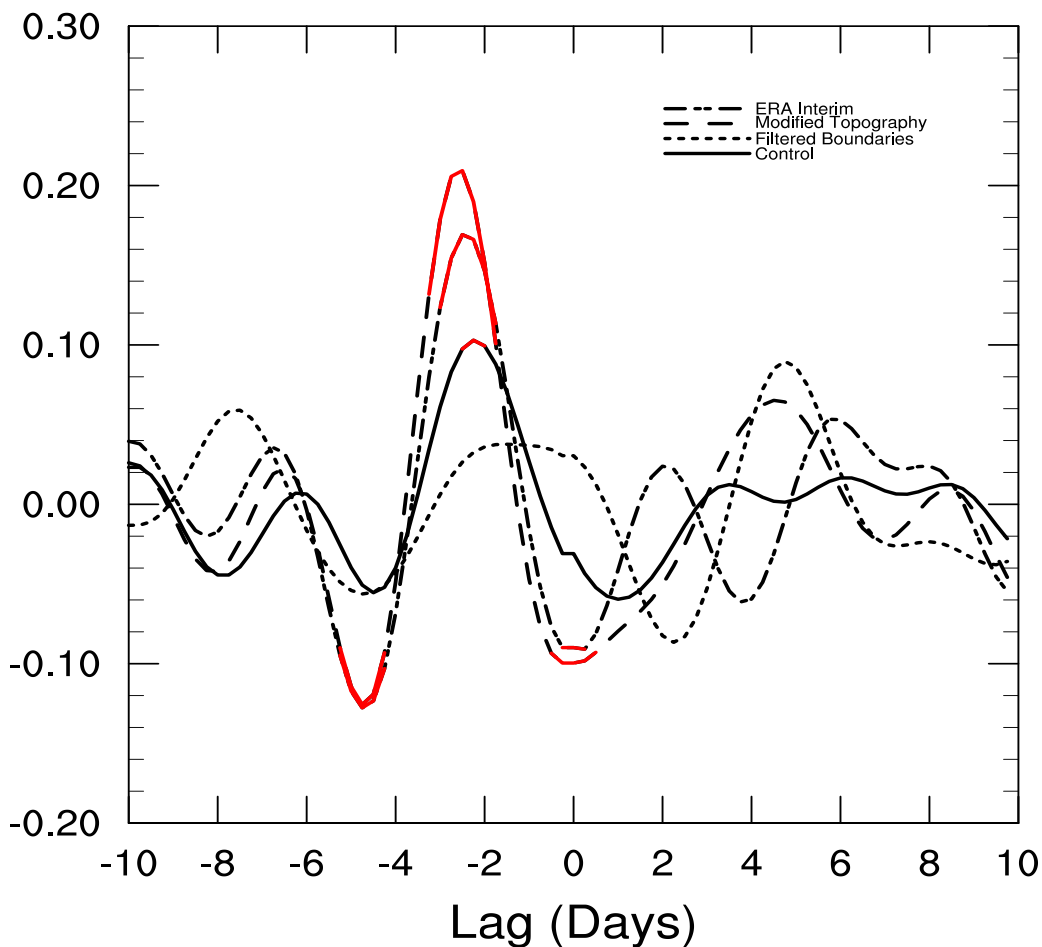Fig. 4.6 Lag correlation of 2.5 – 12 day bandpass filtered vorticity at 550hPa between a 5°x5° box centered in the east Pacific at 9°N, 87°W and a 5°x5° box centered in the Caribbean at 9°N, 64.5°W for ERA Interim, WRF modified topography simulation, WRF filtered boundaries simulation, and WRF control simulation is shown. Red lines indicate correlations that are not independent at the 95% confidence threshold.

The reduction in EW variability in the WRF modified topography simulation compared to the control simulation is further confirmed by examining the 2.5 – 12 day bandpass filtered relative vorticity variance at 550 hPa (top and bottom right panels of Figure 4.7). The contour interval used for ERA Interim is different than that used for the WRF simulations. Model winds are interpolated to the reanalysis grid before the vorticity variance is calculated. EW vorticity variance for all ten summer seasons of the modified topography simulation is significantly reduced over much of the EPAC EW track compared to that of the control simulation, even though EWs propagating from west Africa are still permitted to enter the model domain. The trail of EW variance that leads back towards the Panama Bight in the control simulation and ERA Interim (top left panel

Filtered Vorticity Variance
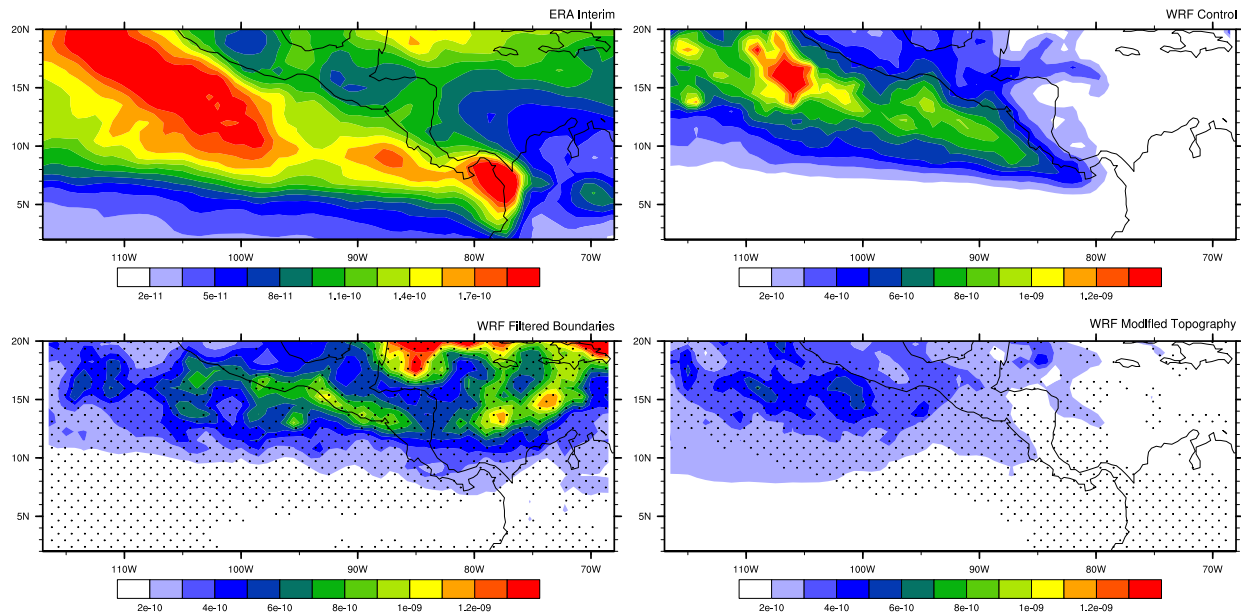


Fig. 4.7  2.5 – 12 day bandpass filtered 550-hPa relative vorticity variance ($s^{-2}$, color contours) is shown for ERA Interim (top left), WRF control (top right), WRF filtered boundaries (bottom left), and WRF modified topography (bottom right) for May-Nov. of 2000-2009. Stippling in the WRF filtered boundaries and WRF modified topography indicates variance values that reject the null hypothesis that they are of the same population as WRF control at the 95% confidence level using the two-tailed f-test. Vorticity in all WRF simulations has been interpolated to the same grid as ERA Interim data.

of Figure 4.7) is absent in the modified topography simulation. The filtered vorticity variance is likewise significantly reduced over much of the EPAC warm pool for the filtered boundaries simulation compared to the control simulation (bottom left panel of Figure 4.7). However, the magnitude of the variance decrease is not as dramatic as that in the modified topography simulation. Also, the variance in the filtered boundary simulation is somewhat shifted towards the coasts of Central America and Mexico compared to the control simulation and not necessarily absent as in the modified topography simulation. The shift in EW and TC tracks is likely the result of the strong changes to the mean state when tropical synoptic variability is removed from the boundary forcing (see bottom left panel of Figure 4.3).

To examine the variability as a function of year, Figure 4.8 shows the 2.5 – 12 day bandpass filtered variance averaged from 5°N-15°N, 80°W–100°W for the May – October period in the WRF simulations. Discarding the month of November in the calculation slightly reduces the magnitude of vorticity variance in the filtered boundary simulation owing to the stronger intrusion of midlatitude variability into the averaging domain observed in animations of winds and precipitation (not shown). Surprisingly, the filtered boundary simulation contains some years with similar amounts of vorticity variance as the control simulation, emphasizing that the variance during some years is spatially shifted and not necessarily reduced compared to the control simulation. The filtered variance in the modified topography simulation is consistently lower than the other WRF simulations suggesting that suppressing diurnal variability is more detrimental to the initiation and development of EPAC EWs than suppressing African EWs.

The sensitivity tests using WRF support the hypothesis that both EWs propagating from west Africa and those initiated locally, associated with strong diurnal convective pulses in the Panama Bight, are important to the number and intensity of EWs in the EPAC. The next section examines a process by which diurnal variability is able to organize vorticity onto EW timescale thus leading to the local initiation and growth of EPAC EWs.

## EW Vorticity Variance (5N-15N,80W-100W)
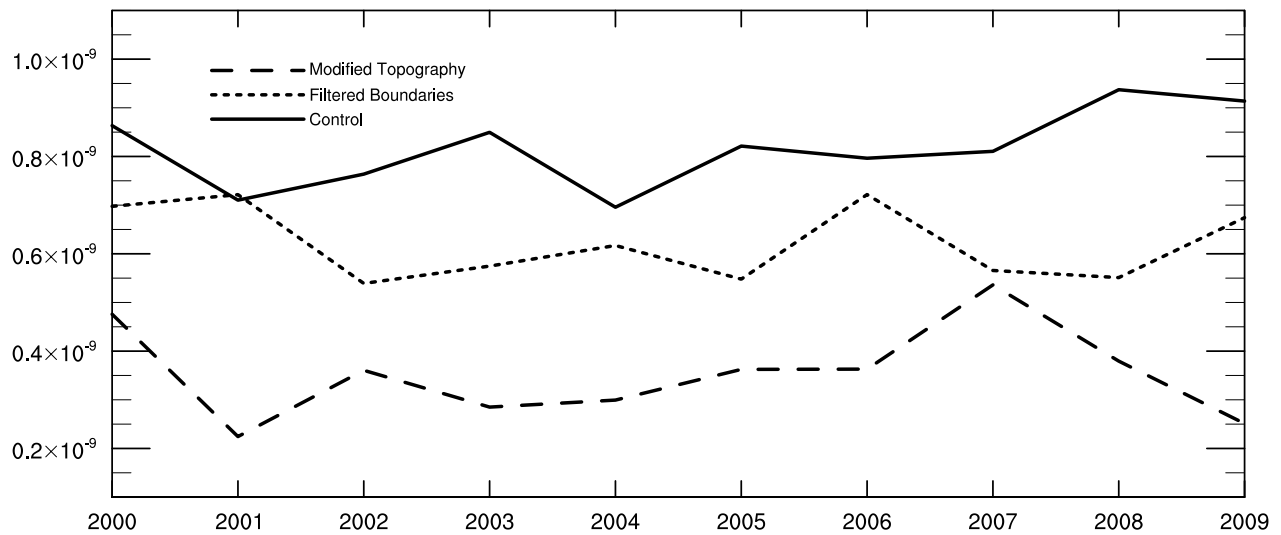


Fig. 4.8 2.5 – 12 day bandpass filtered 550-hPa relative vorticity variance (s$^{-2}$) averaged from 5°N-15°N, 80°W-100°W for each May – October season is shown for ERA Interim, WRF control, WRF filtered boundaries, and WRF modified topography simulation.

**4.4 Easterly Wave Vorticity Initiation and Amplification in the Panama Bight**

Synoptic vorticity variability is significantly reduced across the EPAC in WRF when diurnal variability near the Panama Bight is suppressed. In this section, we investigate mechanisms through which strong transient disturbances emerging from the Panama Bight are able to initiate and amplify EW mid-level vorticity anomalies. To examine the evolution of the vorticity field associated with EWs, lag composites of EWs are shown. The composites are based on a local index of standardized 2.5 – 12 day bandpass

102

filtered 550 hPa vorticity anomalies averaged over a 5°x5° box centered off the coast of Costa Rica (9°N, 87°W). Local maxima greater than 1.0 standard deviations in the index are defined as EW events. Lag composites are then generated based on the peak of the index at lag 0. The general evolution of the vorticity composites is not sensitive to reasonable variations in the box size, location, or index threshold.

Figure 4.9 shows the EW vorticity composites as a function of lag for ERA Interim 550hPa vorticity anomalies defined as deviations from a 10-day running mean. This calculation of anomalies includes those at diurnal and EW timescales, in order to better document the transition of strong Panama Bight disturbances into downstream EWs. Two days prior to the maximum vorticity anomaly amplitude off the coast of Costa Rica, vorticity anomalies at 550hPa maximize along the northwest coast of Columbia, the same region where strong diurnal rainfall variability is well known to occur (i.e. Mapes et al. 2003). This maximum strengthens and stretches westward off the southern coast of Panama twelve hours later. At lag -24 hours, multiple vorticity maxima are present along the southern coast of Central America and provide a broad east-west oriented envelope of vorticity extending from the northwest coast of Columbia to the west coast of Costa Rica. The multiple vorticity maxima may be the result of various propagation speeds associated with phenomena spanning multiple timescales and their interactions, such as the interactions of diurnal and EW vorticity anomalies. Analyzing the vorticity budget later in this section further develops this hypothesis that diurnal variability in this region is critical to EW initiation in the EPAC. At lag -12 hours, a single maxima in the vorticity composite is present in the EPAC with a ½ wavelength of ~1500 km that is comparable to EWs observed in the EPAC using other EW compositing methods (i.e. Serra et al.

# Easterly Wave Vorticity Composite (ERA Interim)



Fig. 4.9 Lag composites of 550-hPa relative vorticity anomalies defined as deviations from a 10-day running mean (s$^{-1}$, color contours) from ERA Interim are shown. Number of EW events in the composites is shown above the top left panel.

2008, Serra et al. 2010, Crosbie and Serra 2014, Rydbeck and Maloney 2014, 2015). At the peak of the event and the following 12 hours, the vorticity maximum develops a southwest to northeast horizontal tilt and propagates to the northwest. Both the tilt and propagation direction are analogous to EW evolution in the EPAC as shown in previous

studies (i.e. Serra et al. 2008, Serra et al. 2010, Crosbie and Serra 2014, Rydbeck and Maloney 2014, 2015).

Using the same methods for compositing ERA Interim data, composite evolution of 550hPa vorticity anomalies for the WRF control simulation is shown in Figure 4.10. Model data has been interpolated to the same grid as ERA Interim. Two days prior to

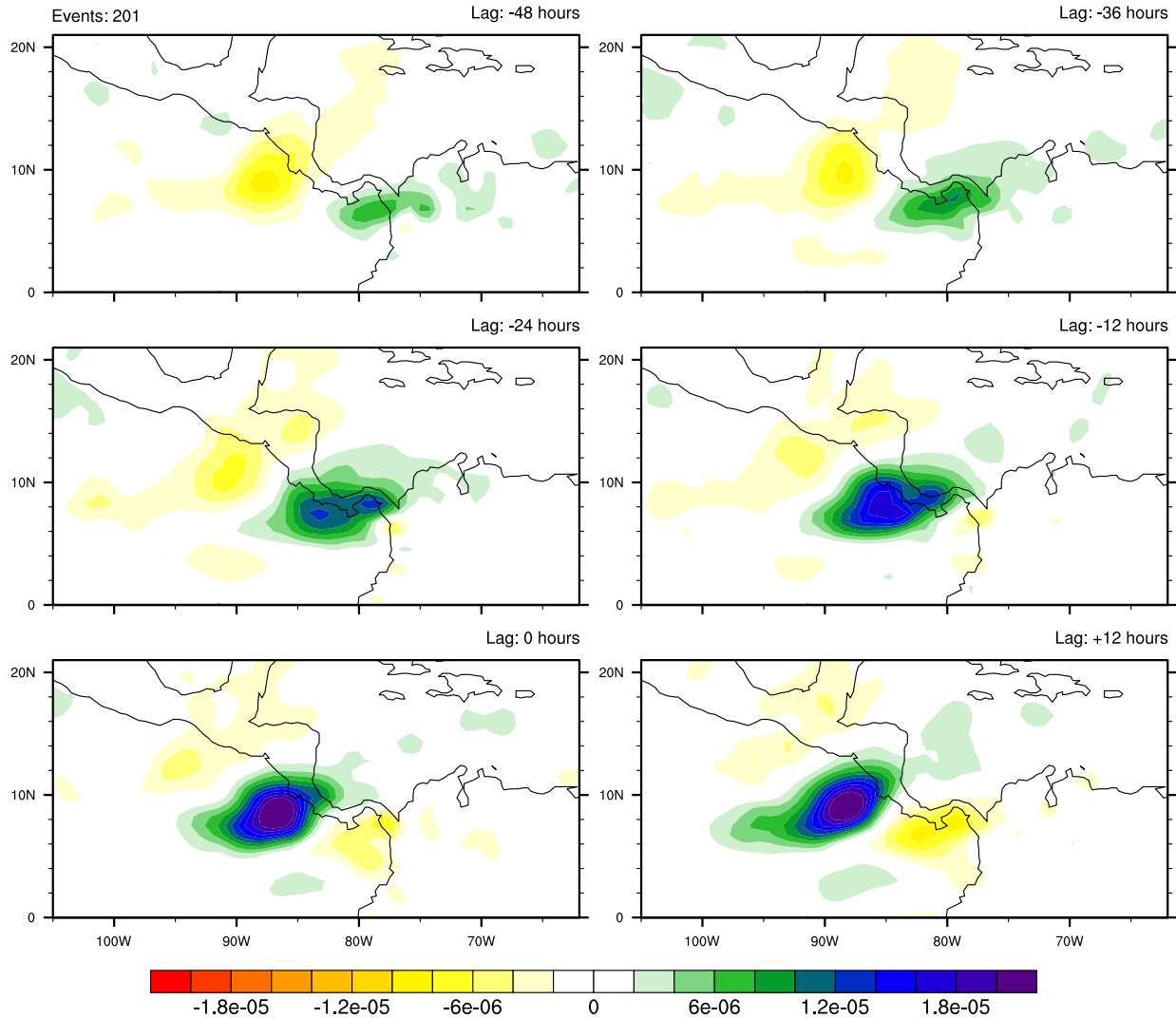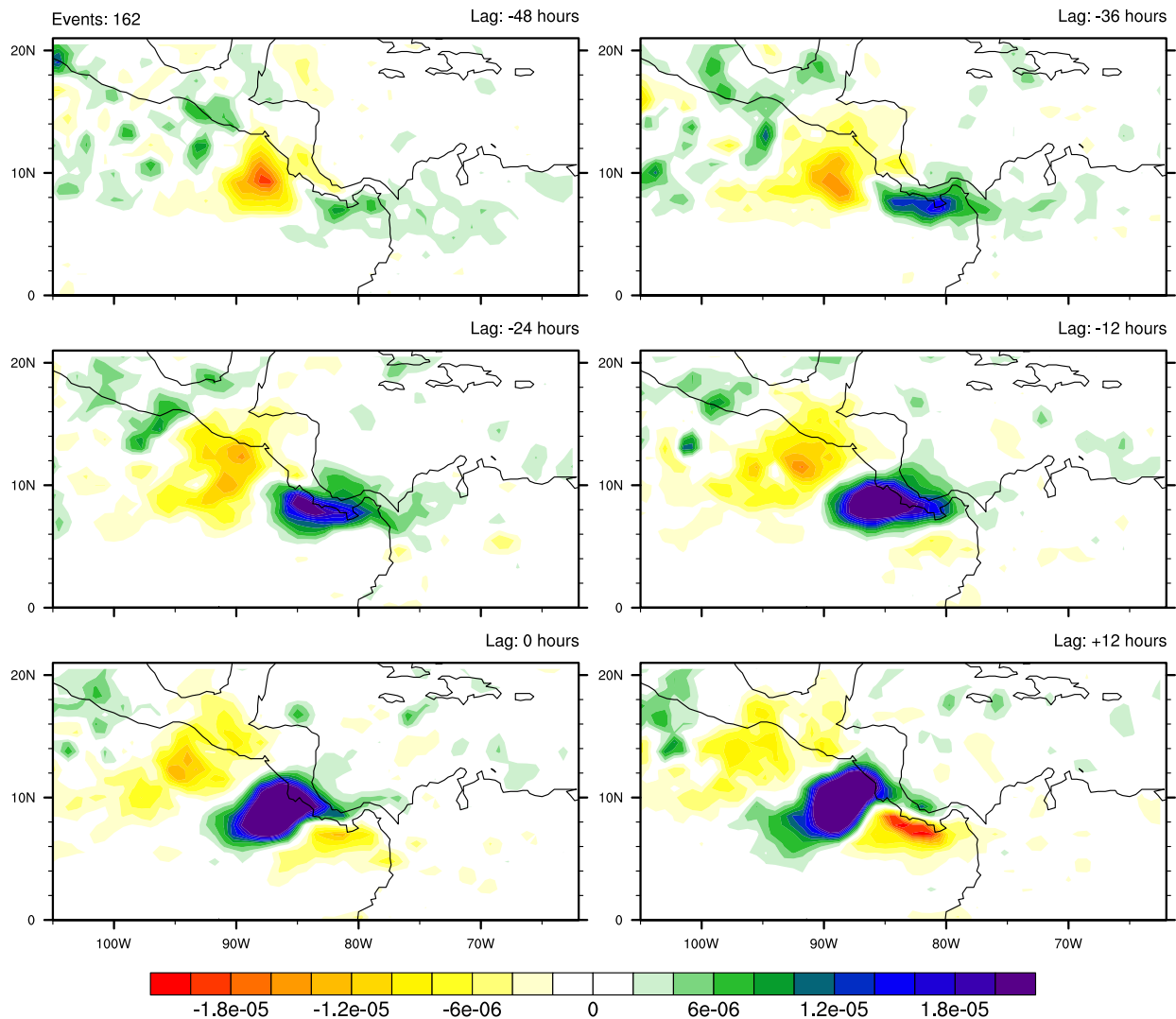## Easterly Wave Vorticity Composite (WRF Control)

Fig. 4.10 Lag composites of 550-hPa relative vorticity anomalies defined as deviations from a 10-day running mean (s$^{-1}$, color contours) from WRF (Control) are shown. Number of EW events in the composites is shown above the top left panel.

the peak in EW 550hPa vorticity, a string of positive vorticity anomalies are present across the Panama Bight. These vorticity anomalies intensify and zonally broaden while migrating westward over the following day and a half, similar to the evolution of vorticity anomalies observed in ERA Interim. At lag 0, a robust positive vorticity envelope has developed off the coast of Central America. 12 hours later, the wave has propagated to the west northwest as anticyclonic vorticity anomalies have developed and intensified behind the EW. At most lags, the EW vorticity composites are greater in magnitude in the WRF control simulation than in observations. In general, the evolution of midlevel vorticity anomalies in the WRF control simulation strongly mirrors the composites in ERA Interim, suggesting that important features of the EWs are well represented in the model. Next, the contribution of strong convective disturbances leaving the Panama Bight to the EW vorticity budget is investigated using the model output.

### 4.4.1 Easterly Wave Vorticity Balance

Rydbeck and Maloney (2015) previously looked at the vertically integrated vorticity budget of the lower troposphere for EPAC EWs using ERA Interim reanalysis data and found that the most important contributions to the local change of EW vertical vorticity are horizontal advection and vertical stretching. The present vorticity budget expands on this analysis to more specifically examine EWs in their formative stages and the importance of diurnal anomalies to the wave's vorticity tendency in WRF. The vertical vorticity tendency at a particular pressure level may be expressed as:

$$\left(\frac{\partial \zeta}{\partial t}\right)_{EW} = -(V \bullet \nabla \eta)_{EW} + \left(\eta \frac{\partial \omega}{\partial p}\right)_{EW} + (\nabla \bullet (\zeta_h \omega))_{EW} + R$$

(1)

where $\eta$ is the absolute vorticity, $\partial \omega / \partial \mathrm{p}$ is the divergence, $\zeta$ is the vertical relative vorticity, $\zeta_\mathrm{h}$ is the horizontal relative vorticity, and the subscript "EW" represents 2.5–12 day bandpass filtered terms. This equation is a form of the vorticity equation presented in Haynes and McIntyre (1987). The term on the left hand side (LHS) of equation 1 represents the local time rate of change of EW vorticity. The local change of the vertical component of EW vorticity on the LHS results from horizontal advection and the effects of stretching and tilting, respectively, on the right hand side (RHS). The residual R is calculated as the difference between the vorticity tendency on the LHS and the sum of the first three terms on the RHS. Contributions to the residual include processes not represented in the terms on the RHS such as the effects of cumulus convection, other subgrid-scale processes, and friction. The residual term also includes any calculation errors in the terms comprising the vorticity budget. All variables are interpolated to a 1.5°x1.5° grid before budget terms are calculated.

### 4.4.2 Easterly Wave Vorticity Tendency

Composites of EW the vorticity tendency and 2.5-12 day bandpass filtered vorticity anomalies at 550hPa are shown in Figure 4.11. All composites shown in the vorticity analysis are based on the same EW index used in Figure 4.10, unless noted otherwise. EW vorticity is interpolated to the same grid as the vorticity budget terms. We are interested in the process occurring during the early "spinup" stages of EWs, so composites of terms in the vorticity budget are shown for lags -36, -12, and 0 hours. At lag -36 hours, a weak vorticity maximum is present in the Panama Bight with a vorticity tendency maximum that is 90° out of phase to the west northwest of the EW vorticity maximum. East of the wave center, near the coast of South America, the vorticity

Fig. 4.11 Lag composites of 2.5 -12 day bandpass filtered 550-hPa relative vorticity anomalies ($s^{-1}$, line contours) and 2.5 -12 day bandpass filtered vorticity tendency ($s^{-1}$ $day^{-1}$, color contours) for the WRF control simulation are shown. Vorticity contour interval is $5*10^{-6}$ $s^{-1}$. The thick solid line is the zero vorticity contour. Number of EW events in the composites is shown above the top panel.

tendency is weak and below the contour color scale. By lag -12 hours, the EW has

become zonally elongated resulting from the leading edge being rapidly propagated to

the west northwest while the trailing edge of the EW is propagated in the same direction much more slowly. The vorticity tendency maximum is 1/8 wavelength ahead of the vorticity maximum at lag -12 hours, indicating the EW is both intensifying and propagating. The vorticity tendency minimum to the east is only 35-45% of the magnitude of the tendency maximum to the west, thus enhancing the zonally elongated structure of the wave. By lag 0 hours, the vorticity tendency minimum has intensified to 65-75% of the magnitude of the tendency maximum, largely halting the zonal elongation of the EW observed at earlier lags. Next, terms on the RHS of (1) that set the zonal wavelength of the EW and contribute to its growth are assessed.

### 4.4.3 Easterly Wave Vorticity Advection

The horizontal advection of vorticity is shown in Figure 4.12 (left column). The advection is of comparable magnitude and mostly collocated with the vorticity tendency, suggesting that the majority of the vorticity tendency is due to advection, as in the findings of Rydbeck and Maloney (2015). The advection maximum is in quadrature with the EW vorticity field at lag -36 hours, but is between ¼ and 1/8 wavelength ahead of the maximum at lags -12 and 0 hours. Although difficult to see in Figure 4.10 (left column), this was confirmed using a different plotting scale and is apparent when analyzing the components of the advection term shown later (see middle column of Figure 4.12 and left column of Figure 4.13). The advection minimum is 1/8 wavelength to the east of the EW vorticity maximum at lags -12 and 0 hours. The ratio of magnitudes between the advection maximum to the west and minimum to the east at each lag is comparable to that of the tendency. This suggests that advection is the major contributor to the zonal elongation of EWs during their formative stages, helping

109

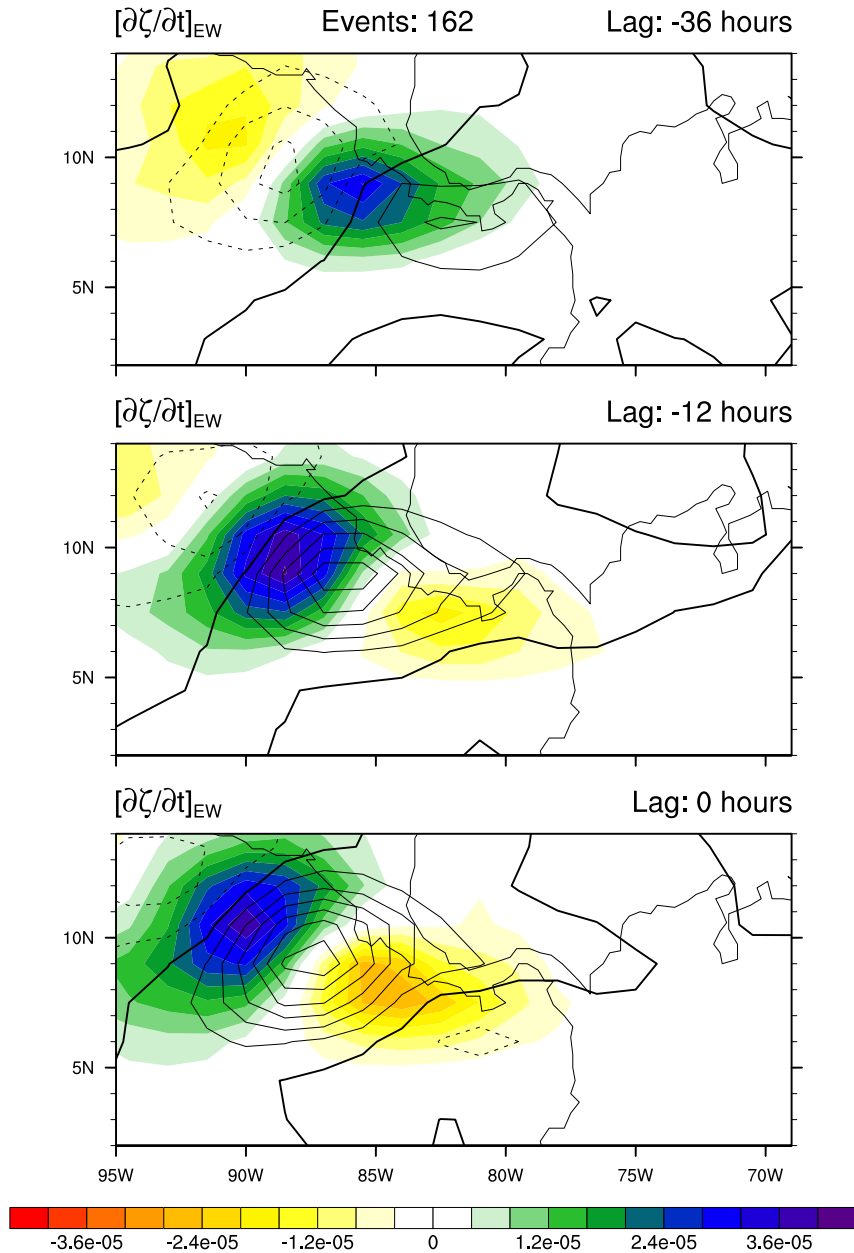## Horizontal Vorticity Advection Composite (WRF Control)



Fig. 4.12 Lag composites of 2.5 -12 day bandpass filtered 550-hPa relative vorticity anomalies (s$^{-1}$, line contours) and 2.5 -12 day bandpass filtered vorticity advection anomalies (s$^{-1}$ day$^{-1}$, color contours; left column), relative vorticity anomalies by the mean wind (middle column), and relative vorticity anomalies by the wind anomalies (right column) for the WRF control simulation are shown. Vorticity contour interval is $5*10^{-6}$ s$^{-1}$. The thick solid line is the zero vorticity contour. Number of EW events in the composites is shown above the top left panel.

to increase the EW zonal wavelength. To further examine this behavior, the horizontal advection term in the vorticity budget is linearly decomposed into variables consisting of 10 day running means (variables with overbars) and deviations from those 10 day running means (primed variables) such that the advection can be expressed as:

$$-\left(\mathbf{V}\bullet\nabla\eta\right)_{EW} \approx -\left(\overline{\mathbf{V}}\bullet\nabla\zeta'\right)_{EW} - \left(\mathbf{V}'\bullet\nabla\overline{\eta}\right)_{EW} - \left(\mathbf{V}'\bullet\nabla\zeta'\right)_{EW}$$

(2) .

Thus the horizontal advection of vorticity on the left hand side of equation (2) is approximated as the sum of the mean winds acting on the anomalous relative vorticity

gradient, the anomalous winds acting on the mean absolute vorticity gradient, and the anomalous winds acting on the anomalous relative vorticity gradient. The first two terms on the RHS of equation (2) are larger than the last term at each lag and describe the majority of the horizontal advection. All terms on the RHS are shown in Figures 4.12 and 4.13. The lag composite of the first term on the RHS of (2), $-\left(\overline{\mathbf{V}} \bullet \nabla \zeta'\right)_{\mathrm{EW}}$ , is shown in the middle column of Figure 4.12. The mean winds acting on the anomalous vorticity gradient strongly mirrors the total advection term (see left column of Figure 4.12) and is the largest of the three terms on the RHS of (2). This suggests that EPAC EWs are predominantly advected by the mean flow. The last term on the RHS of (2), $-\left(\mathbf{V}' \bullet \nabla \zeta'\right)_{\mathrm{EW}}$, opposes the west northwestward propagation and intensification of the wave (left column of Figure 4.12), consequently reducing the net effect of the other two terms (see middle column of Figure 4.12 and left column of Figure 4.13).

The general effect of the wind anomalies acting on the mean absolute vorticity gradient, $-\left(\mathbf{V}' \bullet \nabla \overline{\eta}\right)_{\mathrm{EW}}$ , is to intensify and propagate the wave to the west northwest(right column of Figure 4.13). This term can further be separated into the advection of mean relative vorticity by the wind anomalies, $-\left(\mathbf{V}' \bullet \nabla \overline{\zeta}\right)_{\mathrm{EW}}$ (middle column of Figure 4.13), and the beta effect produced by the meridional wind anomalies, $-\left(v'\beta\right)_{\mathrm{EW}}$ (right column of Figure 4.13). The advection of mean relative vorticity by the wind anomalies is the larger of the two terms. A map of 550 hPa mean relative and absolute vorticity is shown in Figure 4.14. As the waves track along the southern periphery of the monsoon trough, advection of positive mean relative vorticity by the

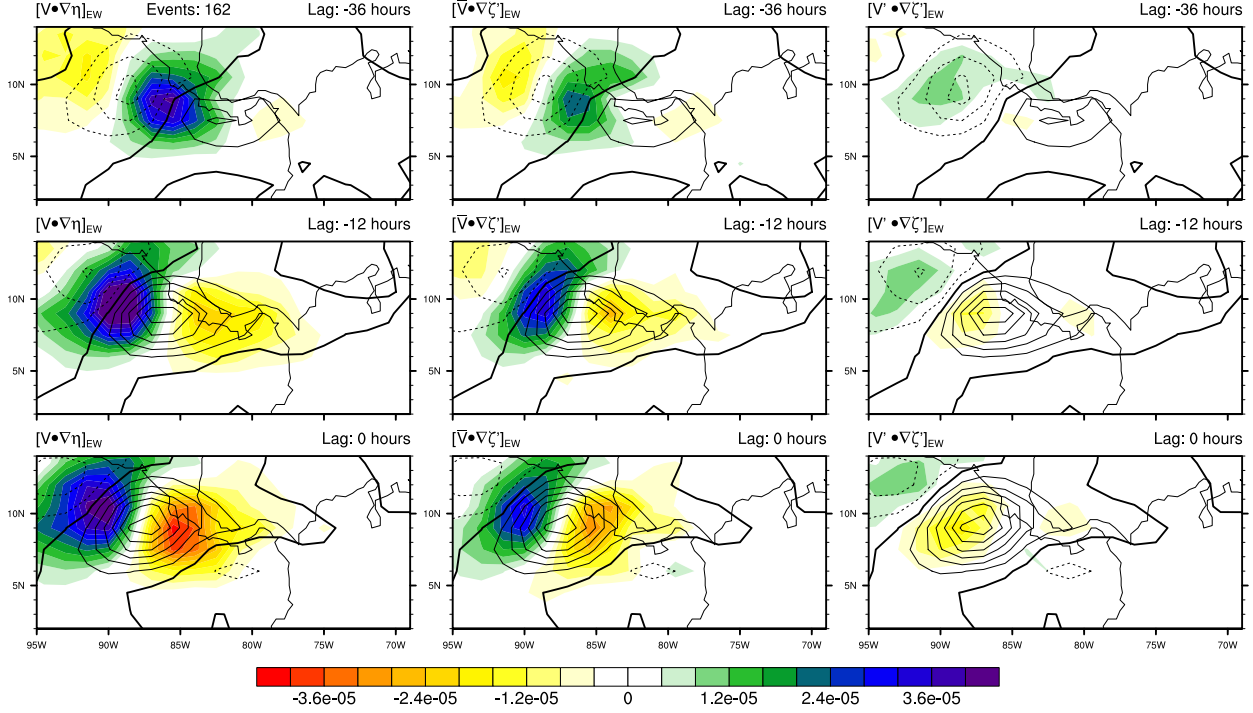## Horizontal Vorticity Advection Composite (WRF Control)
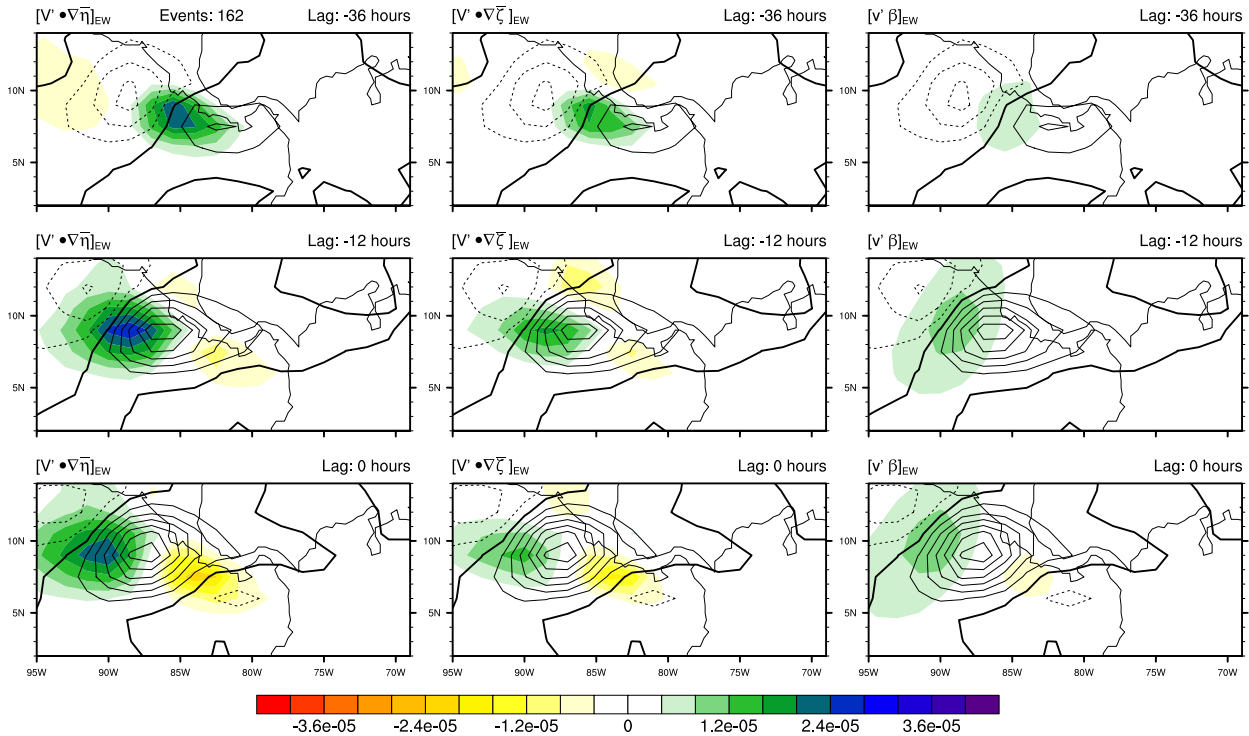


Fig. 4.13 Lag composites of 2.5 -12 day bandpass filtered 550-hPa relative vorticity anomalies (s$^{-1}$, line contours) and 2.5 -12 day bandpass filtered advection of mean absolute vorticity by the wind anomalies (s$^{-1}$ day$^{-1}$, color contours; left column), mean relative vorticity by the wind anomalies (middle column), and planetary vorticity by the meridional wind anomalies (right column) for the WRF control simulation are shown. Vorticity contour interval is 5*10$^{-6}$ s$^{-1}$. The thick solid line is the zero vorticity contour. Number of EW events in the composites is shown above the top left panel.

wind anomalies preferentially occurs ahead of the wave, in the region of anomalously northerly flow. The sign of this term flips along the axis of the monsoon trough, creating a north-south dipole structure ahead of the wave as the wave moves northward as seen at Lag -12 hours. Similar behavior has been observed in TD-disturbances in the west Pacific (Lau and Lau, 1992). Beta advection has a simpler structure with positive advection in front of and negative behind the wave. Because the planetary vorticity gradient does not change, the differences in meridional advection forward and aft of the wave result from differences in the magnitude of the meridional wind anomalies which

have been shown to be stronger on the western periphery of maturing waves (Rydbeck and Maloney 2015).
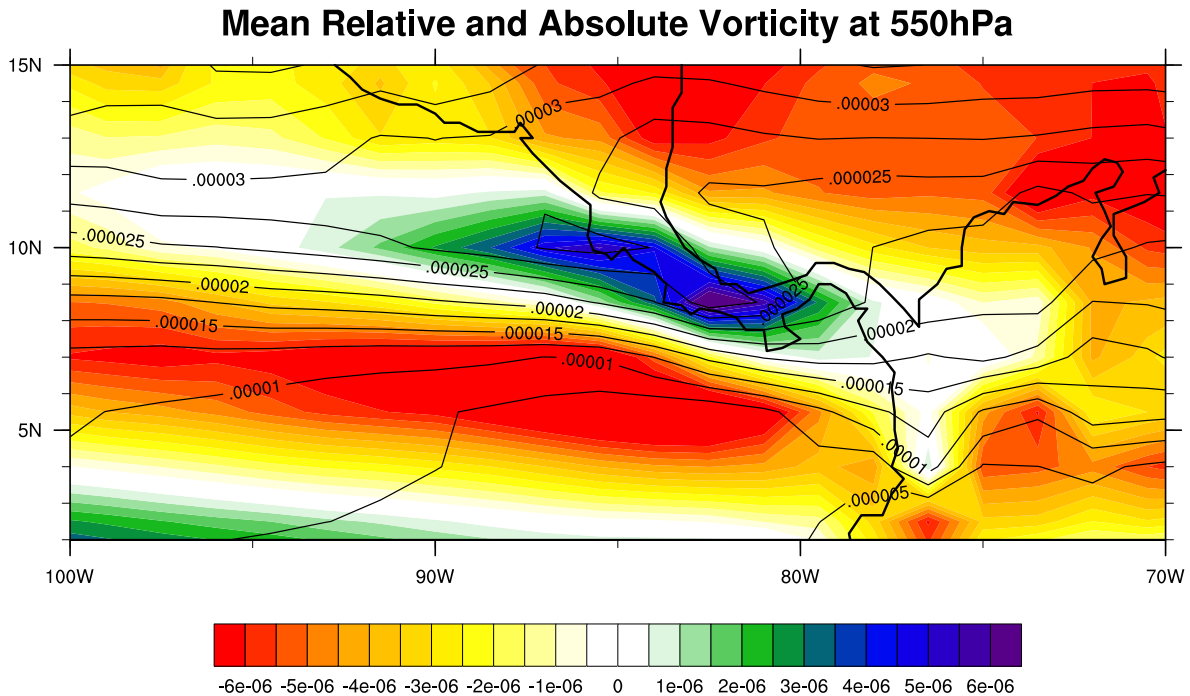


Fig. 4.14 550-hPa mean relative (s$^{-1}$; color contours) and absolute vorticity (s$^{-1}$; line contours) averaged over the 2000-2009 summer season (May-Nov) are shown.

### 4.4.4 Easterly Wave Vorticity Stretching, Tilting, and Residual

The vertical vorticity stretching term of the vorticity budget is shown in Figure 4.15 (left column). Stretching is the largest term in the vorticity budget composite at lag 0 and is approximately 1/8 wavelength behind the EW, leading to amplification in EW intensity but reduction in westward phase speed. Retarding the phase speed of the wave on its eastern side leads to a zonal elongation of the wave that helps increase the EW's zonal wavelength. As will be discussed later, the residual is largely in phase with and of opposite sign to the stretching, reducing confidence in the net effect of the stretching term. The evolution of the stretching term in the composite shows a strong diurnal signal. At lag -36 hours, a singular stretching maximum is present to the east of the

vorticity maximum in the Panama Bight. One day later at lag -12 hours, the local stretching maximum has propagated to the west northwest with the vorticity maximum. This is confirmed by examining the stretching at lag -24 hours (not shown). In addition to the stretching maximum that has propagated westward, another local maximum is present in the Panama Bight in a similar location as the maximum that occurred 24 hours earlier (near 7°N, 81°W). From this it appears that sequential diurnal convective systems propagating westward in the Panama Bight region are partly responsible for creating divergence anomalies in the presence of positive vorticity anomalies that lead to a local spin up of EW vorticity.

To further explore the roles of vorticity and divergence anomalies at various frequencies, the stretching term is first linearized into 10 day running mean variables and deviations from the 10 day running mean, as in equation (2), and written as:

$$\left(\eta\frac{\partial\omega}{\partial p}\right)_{EW} \approx \left(\overline{\eta}\frac{\partial\omega'}{\partial p}\right)_{EW} + \left(\zeta'\frac{\partial\overline{\omega}}{\partial p}\right)_{EW} + \left(\zeta'\frac{\partial\omega'}{\partial p}\right)_{EW} \quad (3).$$

The first two terms on the RHS of (3) are shown in Figure 4.15 (middle and right columns, respectively). The anomalous stretching of the mean absolute vorticity, $\left(\overline{\eta}\frac{\partial\omega'}{\partial p}\right)_{EW}$, is positive 1/8 wavelength behind the EW vorticity maximum at lags -12 and 0 hours, similar to the total stretching term. The maxima of the anomalous stretching of the mean absolute vorticity is collocated with regions where the mean vorticity maxima in the monsoon trough (see Figure 4.14) overlaps regions of anomalous horizontal convergence at and to the east of the EW axis (not shown). These regions of anomalous horizontal convergence are collocated with regions of anomalous upward vertical velocities at 550hPa, suggesting that the stretching is occurring in association

114

## Vorticity Stretching Composite (WRF Control)



Fig. 4.15 Lag composites of 2.5 -12 day bandpass filtered 550-hPa relative vorticity anomalies (s$^{-1}$, line contours) and 2.5 -12 day bandpass filtered vorticity stretching anomalies (s$^{-1}$ day$^{-1}$, color contours; left column), 2.5 – 12 day bandpass filtered stretching of mean absolute vorticity by the anomalous divergence (middle column), and 2.5 – 12 day bandpass filtered stretching of relative vorticity anomalies by the mean divergence (right column) for the WRF control simulation are shown. Vorticity contour interval is 5*10$^{-6}$ s$^{-1}$. The thick solid line is the zero vorticity contour. Number of EW events in the composites is shown above the top left panel.

with deep convection. Maxima of the stretching of anomalous vorticity by the mean

divergence, $\left( \zeta' \dfrac{\partial \bar{\omega}}{\partial p} \right)_{EW}$, (right column of Figure 4.15) slightly lags the EW vorticity

maximum and also contributes to the intensification and slowing of the west

northwestward propagation of the EW. Because both these terms oppose the west

northwestward propagation of the EW predominantly on the EW eastern flank, they

increase the zonal wavelength of the wave by zonally elongating the vorticity field.

115

The last term on the RHS of (3), $\left( \zeta' \dfrac{\partial \omega'}{\partial p} \right)_{EW}$ , is shown in the left column of Figure

4.16. This anomalous stretching term is the strongest of all the vorticity stretching

components on the RHS of (3). Similar to the other terms, the anomalous stretching

term lags the EW vorticity maximum by approximately 1/8 wavelength. The anomalous

winds and relative vorticity in this term may be further decomposed as linear sums of

diurnal and EW anomalies.  High frequency, including diurnal, anomalies are 2 day high

pass filtered and indicated by the subscript "<2". EW anomalies are deviations from the

10 day running mean less the diurnal anomalies and indicated by the subscript "2-10".

The last term on the RHS of equation (3) can written as:

$$\left( \zeta' \frac{\partial \omega'}{\partial p} \right)_{EW} \approx \left( \zeta'_{2-10} \frac{\partial \omega'_{2-10}}{\partial p} \right)_{EW} + \left( \zeta'_{2-10} \frac{\partial \omega'_{<2}}{\partial p} \right)_{EW} + \left( \zeta'_{<2} \frac{\partial \omega'_{2-10}}{\partial p} \right)_{EW} + \left( \zeta'_{<2} \frac{\partial \omega'_{<2}}{\partial p} \right)_{EW} \quad (4).$$

Figure 4.16 (center column) shows the first term on the RHS of (4), that is the

term composed of EW anomalies only. The sum of the last three terms on the RHS of

equation (4) is also shown in Figure 4.16 (right column). The sum describes the

stretching of vorticity owing to interactions of high frequency vorticity anomalies with EW

and high frequency divergence anomalies as well as the interaction of EW vorticity

anomalies with high frequency divergence anomalies. The first term on the RHS of (4) is

predominantly in phase with the EW vorticity thus leading to intensification of the wave.

The sum of the terms that include high frequency anomalies is of comparable

magnitude to the first term on the RHS of (4), suggesting that high frequency anomalies

are as important as EW anomalies to the amplification of the wave by anomalous

stretching. Unlike the first term on the RHS of (4), the sum of the terms involving high

frequency anomalies is 1/8 wavelength behind the wave, indicating that the role of high

116

frequency anomalies is to intensify and zonally elongate the wave. In light of these findings, we hypothesize that serial diurnal convective events in the Panama Bight are partly responsible for the amplification and elongation of EW voricity.
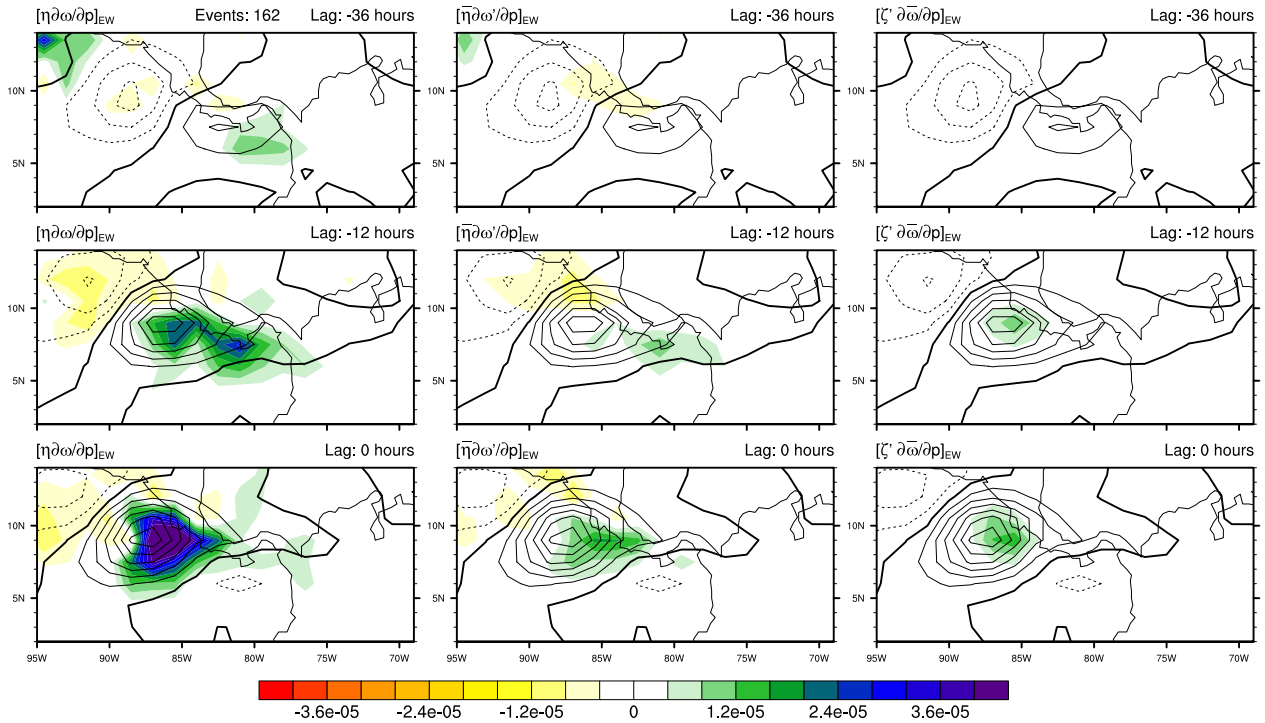
## Vorticity Stretching Composite (WRF Control)



Fig. 4.16 Lag composites of 2.5 -12 day bandpass filtered 550-hPa relative vorticity anomalies (s$^{-1}$, line contours) and 2.5 -12 day bandpass filtered vorticity stretching of relative vorticity anomalies by divergence anomalies (s$^{-1}$ day$^{-1}$, color contours; left column), 2.5 – 12 day bandpass filtered stretching of EW relative vorticity anomalies by EW divergence anomalies (middle column), and 2.5 – 12 day bandpass filtered stretching associated with high frequency vorticity/stretching anomalies (right column) for the WRF control simulation are shown. Vorticity contour interval is 5*10$^{-6}$ s$^{-1}$. The thick solid line is the zero vorticity contour. Number of EW events in the composites is shown above the top left panel.

The contribution to stretching by high frequency anomalies only is shown in Figure 4.17. This term, i.e. the last term on the RHS of (4), is included in the sum of terms in the right column of Figure 4.16 but shown separately here to clarify the role of high frequency anomalies to the local generation of EW vorticity. To note, the scale and contour interval in Figure 4.17 is reduced by 75% compared to Figure 4.16. This term is

interesting because it describes the effect of upscale vorticity organization from short timescales to EW timescales. Much like the sum of terms shown in the right panel of Figure 4.16, the contribution by just high frequency anomalies acts to amplify EW vorticity and slow the west northwestward propagation on the eastern side of the wave. The zonally asymmetric propagation resulting from this term increases the EW zonal wavelength. Perhaps most importantly, this term generates EW vorticity even in the absence of a preexisting EW and provides a mechanism of in-situ EW generation.
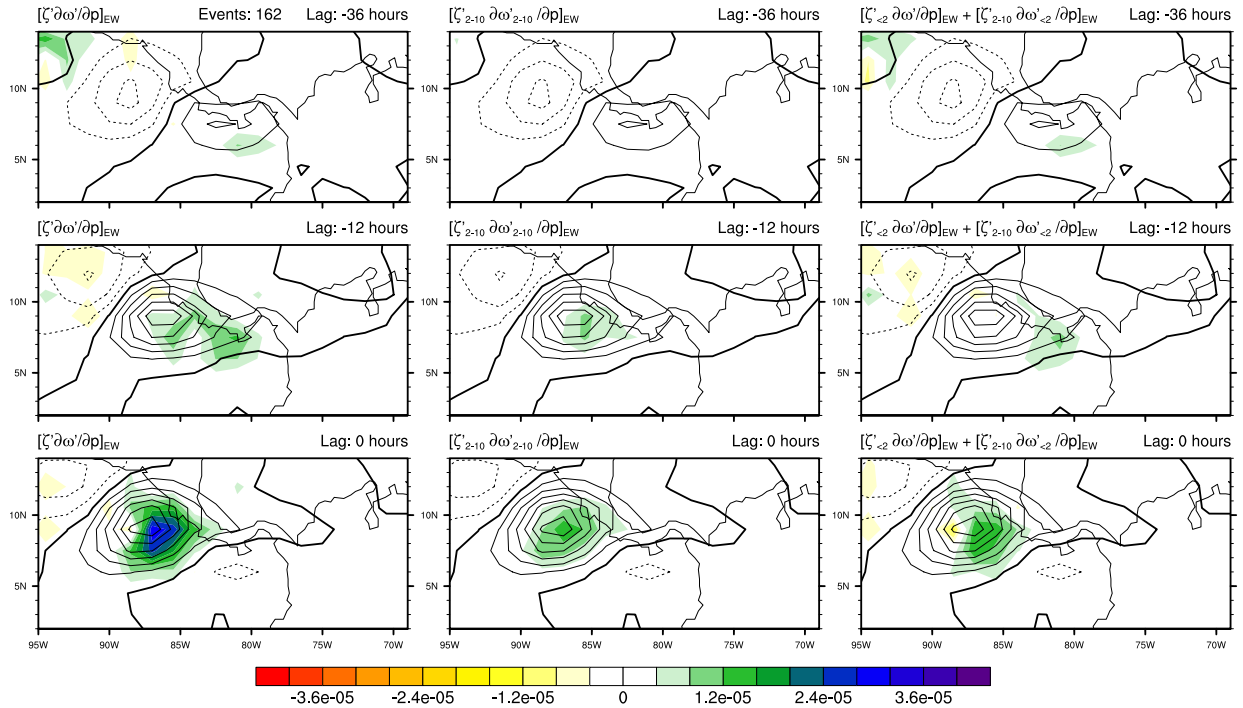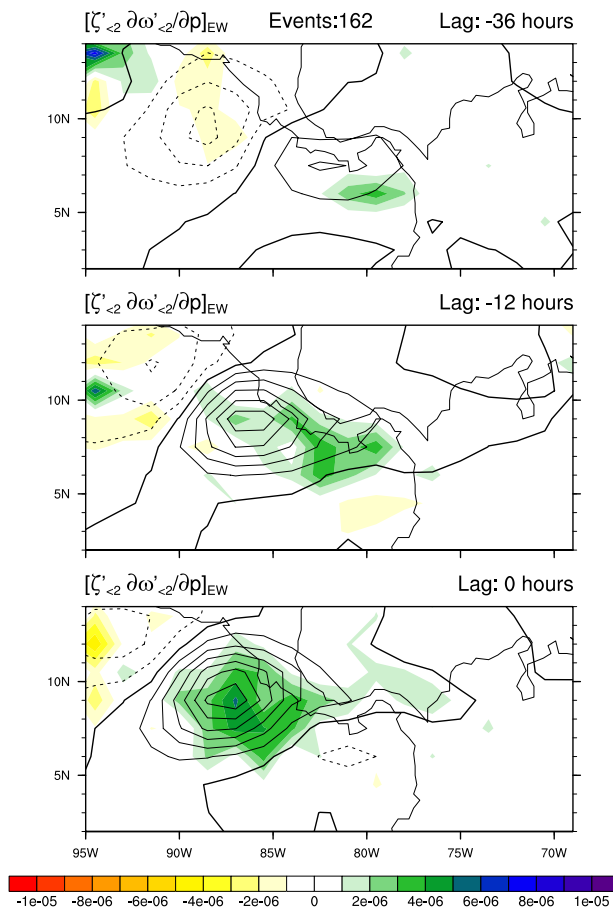


Fig. 4.17 Lag composite of 2.5 - 12 day bandpass filtered 550-hPa relative vorticity anomalies ($s^{-1}$, line contours) and 2.5 -12 day bandpass filtered vorticity stretching by high frequency anomalies ($s^{-1}$ $day^{-1}$, color contours) for the WRF control simulation are shown. Vorticity contour interval is $5*10^{-6}$ $s^{-1}$. The thick solid line is the zero vorticity contour. Number of EW events in the composites is shown above the top panel.

To understand how the interaction of high frequency vorticity and divergence anomalies conspire to initiate EW vorticity in the Panama Bight, Figure 4.18 shows a composite time-longitude diagram of high frequency vorticity and divergence anomalies at 550hPa for the WRF control simulation (left panel) and ERA Interim (right panel). The composite is based on a diurnal index that is constructed by averaging high frequency vorticity anomalies over a 5°x5° box in the Panama Bight centered at 7°N, 82.5°W. Like the EW index, local maxima of the diurnal time series that exceed 1.0 standard deviations are considered diurnal events and used to construct the diurnal composites for the WRF control simulation and ERA Interim, respectively. Both the control simulation and ERA Interim display westward propagating vorticity anomalies with phase speeds near 15 m/s. Model data are interpolated to the same grid as ERA
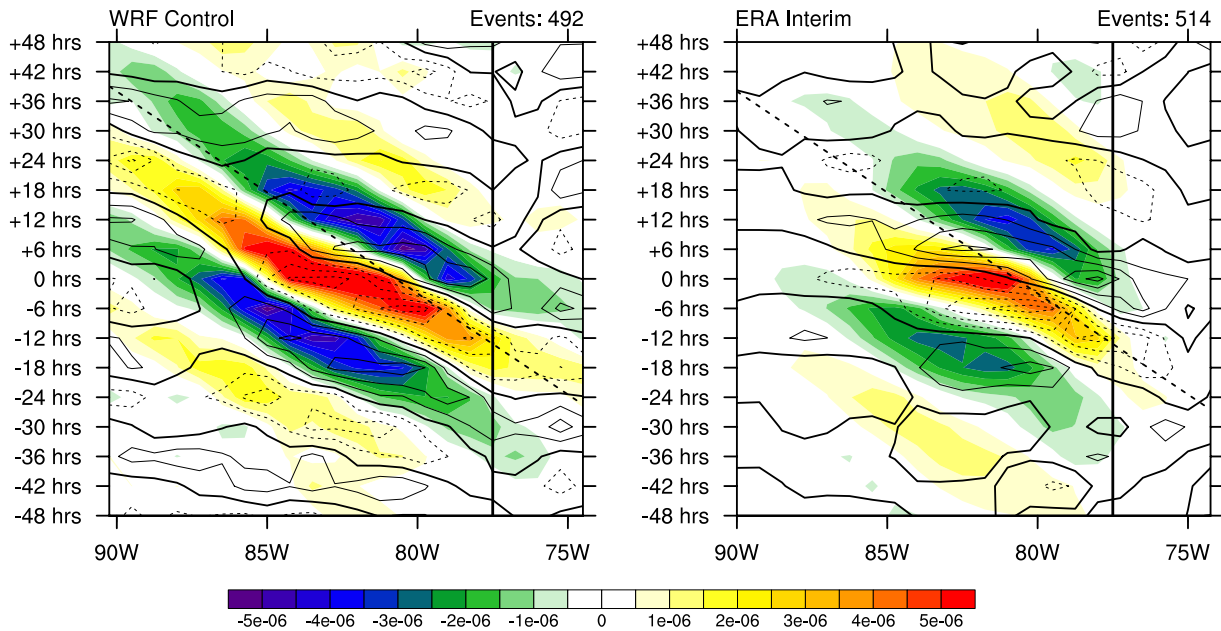


Fig. 4.18 2-day high pass filtered 550-hPa relative vorticity anomalies (s$^{-1}$, color contours) and 550-hPa divergence anomalies (s$^{-1}$, line contours) averaged from 5°N – 9°N are shown as a function of lag versus longitude for WRF control (left) and ERA Interim (right). Divergence contour interval is 5*10$^{-7}$ s$^{-1}$. Vorticity in all WRF simulations has been interpolated to the same grid as ERA Interim. Number of diurnal events in the composites is shown above each panel.

Interim. In the model, positive (negative) vorticity anomalies are largely collocated with horizontal convergence (divergence) anomalies. As a result, the positive vorticity anomalies are locally increased and negative vorticity anomalies are locally decreased. The net effect of this process is to shift the vorticity tendency spectrum to lower frequencies (i.e. from diurnal to two day frequencies) by preferentially reducing negative vorticity anomalies and increasing positive vorticity anomalies in the Panama Bight region. A similar relationship between divergence and vorticity anomalies is seen in ERA Interim, but the phase relationship switches as the anomalies propagate to the west. The process of upscale vorticity organization appears to have a geographical preference in observations while being largely zonally consistent in the model.

The process of upscale vorticity organization by diurnal anomalies is important because it suggests that in the absence of external easterly wave forcing, a seed of easterly wave vorticity can be generated by high frequency anomalies, namely diurnal anomalies. Maloney and Hartmann (2001) and Rydbeck and Maloney (2014) showed that easterly waves could grow from a finite amplitude disturbance into a robust EW in just a couple of days from strong barotropic and perturbation available potential energy to perturbation kinetic energy conversions. The interactions of diurnal vorticity and divergence anomalies in the Panama Bight region support the generation of finite amplitude disturbance at EW timescales that can subsequently develop into a robust EW even in the absence of external EW forcing such as African EWs.

The tilting term in equation (2) is much weaker than the stretching and horizontal advection terms, but does contribute to the zonal elongation of the wave during lags -36, -12, and 0 hours (Figure 4.19) with values of $0.8*10^{-6} - 2.4*10^{-6}$ $s^{-1}$ $day^{-1}$. The

## Vorticity Tilting Composite (WRF Control)

$[\nabla \bullet (\zeta_h \omega)]_{EW}$  Events: 162  Lag: -36 hours

$[\nabla \bullet (\zeta_h \omega)]_{EW}$  Lag: -12 hours

$[\nabla \bullet (\zeta_h \omega)]_{EW}$  Lag: 0 hours

-3.6e-05  -2.4e-05  -1.2e-05  0  1.2e-05  2.4e-05  3.6e-05
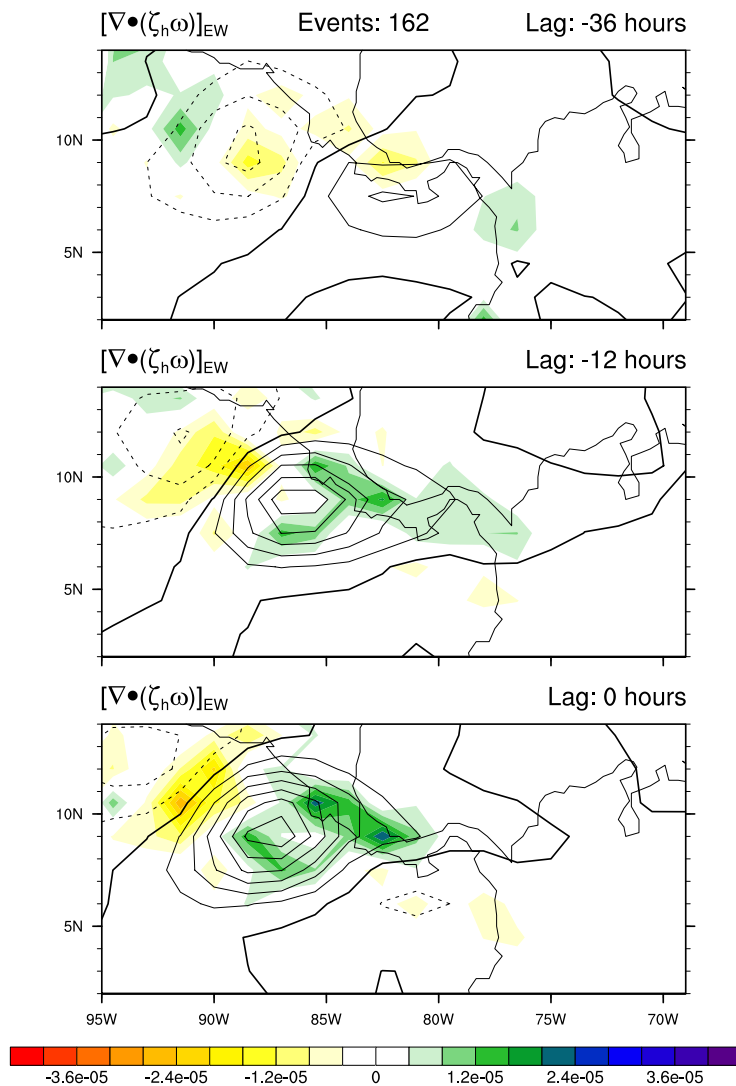
Fig. 4.19 Lag composites of the 2.5 -12 day bandpass filtered 550-hPa relative vorticity anomalies ($s^{-1}$, line contours) and 2.5 -12 day bandpass filtered tilting ($s^{-1}$ $day^{-1}$, color contours) for the WRF control simulation are shown. Vorticity contour interval is $5*10^{-6}$ $s^{-1}$. The thick solid line is the zero vorticity contour. Number of EW events in the composites is shown above the top panel.

positive maxima in the tilting term are confined to regions over land, suggesting that either sea-breeze type deep convection or the mechanical tilting effects of the terrain are important. The residual of the budget is positive on the northern edge of the wave and negative at and to the south of the wave with magnitudes on the order of the leading terms of the budget (see figure 4.20). At 550 hPa and away from high terrain,

turbulent drag likely does not contribute much to the residual. EWs are convectively coupled phenomena that derive much of their energy from latent heating. While the grid spacing of the vorticity budget includes the effects of cloud clusters, the effects of cumulus convection at the meso- and cloud scale are not included. Subgrid-scale processes involving the bulk transport and tilting of vorticity that are missing from equation (2) have been shown to be important to the vorticity budget of EWs in the eastern Atlantic and west Pacific (e.g. Reed and Johnson 1974, Stevens 1979, Esbensen et al. 1982). Esbensen et al. (1982) showed that near 600mb, processes involving small-scale motions were as important as processes involving cloud clusters to the vorticity budget of EWs in the eastern Atlantic. The subgrid-scale vorticity tendency was also of opposite sign to that of the cloud cluster scale vorticity tendency at this level, consistent with the largely opposing signs of the residual and grid scale stretching terms in the vorticity budget presented here. As a result, we suspect that omitting processes at meso- and cloud scales accounts for much of the residual and suggest interpreting the grid-scale stretching and tilting terms with caution.

Because of the residual's large magnitude, it is useful to examine the combined effects of grid scale and subgrid scale processes in a singular term. Figure 4.20 shows the sum of grid scale stretching, grid scale tilting, and the residual that includes subgrid scale effects for lags -36, -12, and 0 hours. The sum of terms shown in 4.20 are largely collocated with maxima of midlevel vertical velocity anomalies, suggesting that the net vorticity tendency resulting from stretching, tilting, and residual are strongly determined by convection. At lag -36 hours, the net effect of convection is to elongate the wave to the east and oppose the effects of horizontal advection to the west of the wave. At lags -

12 and 0 hours, convection mainly results in a positive vorticity tendency in the northeast quadrant of the wave. This pattern of vorticity tendency leads to a southwest to northeast horizontal tilt of the wave that is favorable for barotropic conversions that lead to increased EW kinetic energy. This finding affirms the main conclusions of Rydbeck and Maloney (2015).
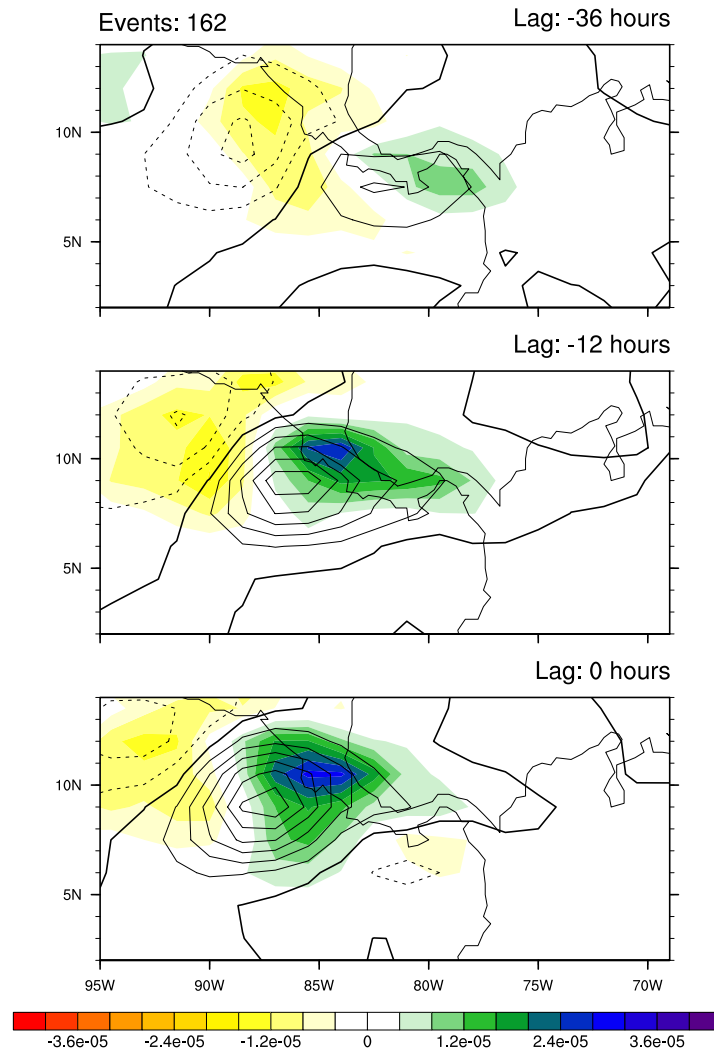


Fig. 4.20 Lag composites of the 2.5 -12 day bandpass filtered 550-hPa relative vorticity anomalies ($s^{-1}$, line contours) and sum of the 2.5 -12 day bandpass filtered stretching, tilting, and residual tendency ($s^{-1}$ day$^{-1}$, color contours) for the WRF control simulation are shown. Vorticity contour interval is $5*10^{-6}$ $s^{-1}$. The thick solid line is the zero vorticity contour. Number of EW events in the composites is shown above the top right panel.

**4.5 Discussion and Conclusions**

Many previous studies have suggested that the majority of EWs in the EPAC form in association with preexisting EWs propagating from west Africa. There are obvious cases in which robust EWs with considerable convection are able to propagate from west Africa and across the Caribbean with strong signatures in satellite imagery. However, EWs routinely weaken over the Caribbean, a region of strong EW lysis (Serra et al. 2010). Thus, understanding mechanisms of EW formation and/or reenergizing are critical to forecasting EPAC EWs as well as the TCs they produce.

The sensitivity of EPAC EWs to mechanisms of local and remote forcing are investigated in WRF sensitivity test. In the first sensitivity test, westward propagating synoptic variability is removed in the boundary forcing. In this filtered boundary simulation, EW variance in EPAC is significantly reduced compared to the control simulation suggesting that external forcing, namely EWs originating near west Africa, is important to the distribution of EPAC EWs. In the second simulation, diurnal convective variance in the Panama Bight that propagates westward at gravity wave speeds is suppressed. This is accomplished by reducing the model terrain height in northern South America and portions of Central America. Similar to the first sensitivity simulation, EPAC EW variance is significantly reduced in the EPAC warm pool. The significant reduction in EW variance by suppressing diurnal variability in and around the Panama Bight in WRF indicates that mechanisms of EW formation and intensification are likewise suppressed. In this simulation, extant EPAC EWs are significantly correlated to EWs in the Caribbean 2-3 days earlier. This result suggests that in the absence of local mechanisms of EW initiation and intensification, EPAC EWs are more strongly

dependent on remote forcing. The overall findings of the WRF sensitivity simulations indicate that remote forcing and in-situ mechanisms of EW forcing are important to the distribution and amplitude of EPAC EWs. In this study, we focus on the processes by which diurnal anomalies are able to initiate and amplify EW vorticity anomalies.

In the WRF control simulation, local vorticity tendencies during the formative stages of EWs are most strongly regulated by horizontal vorticity advection and vertical vorticity stretching, similar to the findings of Rydbeck and Maloney (2015) using reanalysis. Horizontal advection of positive vorticity anomalies preferentially occurs on the western side of the wave, with weaker advection of negative vorticity anomalies occurring on the eastern side. The zonally unbalanced advection leads to a zonal elongation of the wave. Additionally, vertical stretching of vorticity anomalies largely occurs 1/8 wavelength to the east of the wave's center. Stretching to the east of the wave's center helps anchors vorticity anomalies there, further supporting the zonal elongation of the EW such that the EW zonal wavelength is increased. The strongest contribution to vorticity stretching is the anomalous vorticity stretching term, $-\left(\zeta'\dfrac{\partial\omega'}{\partial p}\right)_{EW}$.

This term can be further decomposed into two categories: stretching by EW anomalies only and stretching involving high frequency anomalies. The stretching involving high frequency anomalies is of comparable value to stretching by EW anomalies only and contributes to the intensification and zonal elongation of EPAC EWs.

Of most importance is the interaction of high frequency vorticity and divergence anomalies. Near the Panama Bight, positive vorticity anomalies are collocated with horizontal convergence anomalies, and negative vorticity anomalies are collocated with horizontal divergence anomalies. The resulting effect is to reduce the amplitude of

negative diurnal vorticity anomalies and increase the amplitude of positive diurnal vorticity anomalies. The interaction of these diurnal anomalies leads to a vorticity tendency that extends to longer timescales. The positive vorticity tendency created by the diurnal anomalies is able to either amplify background vorticity noise in the easterly wave frequency band or intensify preexisting easterly waves that have significantly atrophied on their westward transit across the Atlantic and Caribbean. We hypothesize that this effect generates a seed of EW vorticity that is necessary for further EW growth to take place in the absence of remote EW forcing. This process is described as an upscale vorticity organization by high frequency anomalies in which vorticity at EW timescales is generated in-situ. This vorticity can subsequently grow into a robust EW via barotropic and perturbation available potential energy to perturbation kinetic energy conversions in just a couple of days (Rydbeck and Maloney 2014). Transitions of diurnal mesoscale convective features to longer timescales have also been observed west of Sumatra and Borneo (Johnson et al. 2013). Thus, mechanisms of upscale organization in the east Pacific may be shared with other tropical regions containing localized and intense diurnal forcing of precipitation.

Tilting is weaker in magnitude but important to the increase of the EW zonal wavelength. Sub-grid scale bulk transport and tilting of vorticity appear to be as important as other terms in the vorticity budget at midlevels and generally oppose the effects of the grid-scale stretching.  Horizontal advection, stretching, and tilting, both at the grid scale and sub-grid scale, increase the EWs zonal wavelength by approximately 30% in 1.5 days. The presumed impact of subgrid-scale processes on the residual of

the vorticity budget motivates the use of model setups capable of explicitly resolving convection in future studies.

EPAC EWs have been shown to be sensitive to variations in the background atmosphere, particularly on intraseasonal timescales. Rydbeck and Maloney (2015) note that convective intensity in the Panama Bight remains unchanged when averaged over respective intraseasonal phases, suggesting that the seeding mechanism proposed herein might be resistant to changes in the background atmospheric environment. This requires further investigation. From examining the vorticity budget, the tendency of EW vorticity anomalies appears sensitive to the distribution of mean relative vorticity, commonly referred to as the monsoon trough. EPAC intraseasonal variability is well known to modulate the EPAC monsoon trough and might also modulate those processes involved with EW vorticity tendencies during their formative stages in the Panama Bight. Examining these sensitivities are a focus of future work. Also, the effects of diurnal anomalies on EW vorticity stretching are perhaps not exclusive to EW formation but could also apply to the reenergizing of atrophied EWs propagating across the Caribbean Sea from West Africa. It is possible that pre-existing EWs entering the EPAC provide a favorable environment for contributions by diurnal anomalies to occur. Alternatively, anticyclonic vorticity anomalies to the east of an EPAC EW might suppress diurnal convective variability in the Panama Bight. The interaction of pre-existing EWs and diurnal anomalies is a topic of future work.

EPAC EWs seed the majority of TCs in the EPAC. Most of the EWs associated with TCs genesis in the EPAC are said to originate in Africa even when the waves have deteriorated so much that they are unidentifiable as they cross the Atlantic Ocean and

Caribbean Sea. In this paper, we propose a new mechanism of in-situ generation and amplification that does not necessarily assume a continuous propagation of EWs from West Africa. In light of these results, diurnal mesoscale convective activity that leads to strong midlevel diurnal vorticity anomalies are hypothesized to function as nucleuses for EPAC EW formation in the absence of any preexisting EWs entering the EPAC from the Caribbean Sea. In this framework, better understandings and simulations of diurnal convective systems near the Panama Bight and their interactions with the background atmospheric state will enhance forecast skill of EPAC EWs.

**CHAPTER 5 Conclusions**

**5.1 Primary Findings**

The purpose of this study is to better understand the mechanisms by which easterly waves (EWs) in the east Pacific (EPAC) are initiated and intensify. Holton et al. (1971) hypothesized that EWs are the building blocks of the climatological Intertropical Convergence Zone and, by extension, improving our understanding of EWs in the EPAC helps to improve our understanding of the general circulation of Earth's atmosphere. The EPAC is also the densest region of tropical cyclones (TCs) in the world, with the majority of TCs there seeded by EWs. The findings of this study include an improved understanding of the processes and variability of easterly wave energetics, patterns of convective coupling within EWs and their impacts on EW intensification, and local versus remote forcings of EW initiation in the EPAC which involve a novel mechanism of in-situ EW generation.

The mechanism, magnitude, location, and vertical structure of east Pacific easterly wave energetics strongly vary on intraseasonal time scales. Intraseasonal variability in the EPAC warm pool is characterized by alternating periods of westerly and easterly low-level winds. Westerly periods are associated with enhanced latent heat fluxes and precipitation. Easterly periods are associated with suppressed latent heat fluxes and precipitation. During westerly periods, the conversion of perturbation available potential energy to perturbation kinetic energy is enhanced by 25% compared to neutral periods in the EPAC. The same conversion term is substantially weaker as EWs develop during easterly intraseasonal periods. In the middle troposphere during

129

westerly intraseasonal periods, the generation of perturbation kinetic energy by barotropic conversions is as strong as those conversions occurring in the lower troposphere. Under these conditions, strong midlevel vortices associated with mesoscale convective systems are able to grow into EWs capable of seeding tropical cyclones. Many studies have stressed the importance of midlevel vorticity generation to the subsequent genesis of tropical cyclones (Bister and Emanuel 1997; Raymond et al. 1998, 2014; Davis 2015). The leading terms of the perturbation kinetic energy budget suggest that robust easterly waves are able to mature from trivial disturbances in just 1.5 – 2.5 days. Unraveling mechanisms responsible for generating trivial disturbances at EW timescales in the EPAC is the focus of the fourth chapter of this study and described at the end of this section.

Preferred regions of EW convection located in the southwest and northeast quadrants of EWs are supported by collocated column-integrated moisture anomalies. Convection in these quadrants forces the vertical stretching of positive vorticity that acts to increase the local vorticity there. The local increase of vorticity in the southwest and northeast quadrants elongates the wave horizontally in those same directions. The horizontal tilt of the wave that results from the asymmetric distribution of convection and attendant local vorticity generation is necessary for the EW to be energized by the cyclonic wind shear of the background zonal wind, often referred to as a component of the barotropic conversion term. Thus, convection not only energizes the wave directly through the conversion of perturbation available potential energy to perturbation kinetic energy, but also tilts the wave horizontally such that barotropic conversions may occur. The convective coupling of EWs shows dramatic variation on intraseasonal timescales.

Westerly intraseasonal periods are more strongly convectively coupled when compared to neutral intraseasonal periods. Easterly intraseasonal periods are less convectively coupled versus neutral periods and, as a result, EWs are much slower to intensify.

In a regional model, EPAC EWs are sensitive to the removal of local and remote forcing mechanisms. When EWs propagating from West Africa and the Atlantic are suppressed in the boundary forcings of a regional model, significant decreases in EW variance are observed in the EPAC. Similarly, when diurnal convective activity in the Panama Bight is strongly dampened in the model, EW variance in the EPAC is significantly reduced. These modeling results support the paradigm that both remote forcing and in-situ generation of EWs are critical to the distribution and amplitude of EWs in the EPAC.

In the model, diurnal divergence and vorticity anomalies in the Panama Bight interact such that vorticity tendencies on easterly wave timescales are produced. Diurnal oscillations in the Panama Bight are structured such that positive vorticity anomalies are collocated with horizontal convergence anomalies and negative vorticity anomalies are collocated with horizontal divergence anomalies. Amplifying positive vorticity anomalies and weakening negative vorticity anomalies produces an anomalous positive vorticity tendency with timescales longer than the diurnal oscillation. This process locally generates a nucleus of EW vorticity that is zonally elongated by horizontal advection and vertical stretching to wavelengths commonly observed in EWs. Even in the absence of remote forcing, EPAC EWs are able to initiate and intensify in-situ in a regional model by this mechanism.

## 5.2 Applications

Perhaps one of the most important applications of these results is to improve forecasts of TC genesis. In the EPAC, more vigorous synoptic-scale vortices are associated with a greater likelihood of tropical cyclogenesis (Davis et al. 2008). This is not necessarily the case in other basins such as the Atlantic. This study has made great strides in understanding the processes by which vortices associated with EWs in the EPAC intensify. Moreover, a novel mechanism of in-situ generation of EWs in the EPAC has been proposed. Some basic application of these results to practical forecasts of EW development and intensification as well as ideas for evaluating a model's efficacy at simulating EPAC EWs are suggested.

The majority of TCs in the EPAC are generated in association with EWs. However, the responsible EWs have been traditionally thought to originate near West Africa and propagate westward across the Atlantic and Caribbean, eventually arriving in the EPAC. This trajectory of EWs across the Western Hemisphere is assumed to occur even when the waves deteriorate and become unobservable over the western Atlantic and Caribbean. Because EWs propagate westward at 8 m s$^{-1}$, it takes approximately 1 week for a wave to propagate from the lesser Antilles to the EPAC. Alternatively, Rydbeck and Maloney (2014) showed that trivial disturbances in the EPAC are capable of developing into a robust EW in a matter of days. It is possible that the assumed continuous trajectory of EWs by forecasters leads to an assumed, and potentially false, confidence in the amount of time required for robust EWs capable of seeding TCs to develop in the EPAC. Occam's razor states that among competing hypotheses that predict equally well, the hypothesis with the fewest assumptions should be selected. We

are not convinced that the hypotheses of remote and local forcing of EPAC EWs tested in this study are competing; nonetheless, the proposed mechanism of in-situ generation of EPAC EWs contains fewer assumptions and should be further considered in observations and various models to determine its validity. For example, during periods of dormant EW activity in the Atlantic, an emphasis should be placed on the intensity and routineness of mesoscale convective systems propagating westward from the Panama Bight when forecasters are contemplating downstream EW development in the EPAC. If the proposed mechanism of in-situ generation is valid, then forecast skill should increase under conditions of weak remote forcing.

The conclusions of this study also suggest that emphasis should be placed on the intraseasonal phase of the EPAC when considering the intensification of EWs capable of seeding TCs, similar to the conclusions of earlier studies. Westerly intraseasonal periods are much more favorable than other intraseasonal periods for spinning up and increasing the convective activity of EPAC EWs. Easterly intraseasonal periods are associated with much more slowly developing EWs that tend to have weaker convective anomalies.

When evaluating the representation of EPAC EWs in models, we would encourage researchers to place an emphasis on properly resolving the background state through which easterly waves propagate and are energized. These changes include those that are associated with strong intraseasonal oscillations in the EPAC. Variations in the background moisture profile, horizontal winds, ITCZ intensity, and shear can strongly influence the growth (or decay) of EPAC EW vorticity and kinetic energy. The horizontal distribution of convection within the EW vorticity envelope should

also be emphasized when evaluating a model's efficacy at simulating EPAC EWs. The distribution of convection within EWs vorticity envelopes has been shown to modulate the horizontal tilt of the wave and subsequent perturbation kinetic energy changes by barotropic conversion.

## 5.3 Future Work

The bulk of future work focuses on further determining the importance of the proposed mechanism of in-situ EW initiation, referred to as the tendency to organize vorticity upscale (TOVU). The sensitivity of TOVU to variations in model parameters (and models) requires further exploration. In the future, we propose to run an ensemble composed of various model parameterizations for a case study in which diurnal mesoscale convective systems originating near the Panama Bight are accompanied by the development of a TC, such as TC Elida (2008). An ensemble with at least 8 members will be run for a two-week period to capture the genesis of the EW and resulting TC. Similar to the sensitivity experiments performed in Chapter 4, remote forcing will be suppressed in one set of ensembles and local forcing associated with diurnal mesoscale convective systems in the Panama Bight region will be suppressed in another set of ensembles. The latter will be achieved by modifying the topography as in Chapter 4. The ensemble sets (i.e. the control ensemble, the filtered boundary ensemble, and the modified topography ensemble) will be used to determine the sensitivity of remote and local forcing mechanisms to the model arrangement. Because resolving small scale cloud features were suggested as being important to the redistribution of vorticity within EWs in Chapter 4, we recommend that that these model studies be performed at grid spacing able to explicitly capture convective process and

the attendant transport of vorticity at those scales. Also, a reasonable next step in understanding the in-situ generation of EPAC EWs from diurnal transients in the Panama Bight is to examine the vertical heating profiles that preferentially drive the convergence of positive vorticity and divergence of negative vorticity that organizes on EW timescales.

# REFERENCES

## CHAPTER 2

Aiyyer, Anantha, Ademe Mekonnen, Carl J. Schreck, 2012: Projection of Tropical Cyclones on Wavenumber–Frequency-Filtered Equatorial Waves. *J. Climate*, **25**, 3653–3658.

Avila, Lixion A., Richard J. Pasch, 1992: Atlantic Tropical Systems of 1991. *Mon. Wea. Rev.*, **120**, 2688–2696.

Avila, Lixion A., Richard J. Pasch, 1995: Atlantic Tropical Systems of 1993. *Mon. Wea. Rev.*, **123**, 887–896.

Avila, Lixion A. and J. L. Guiney, 2000: Eastern North Pacific hurricane season of 1998. *Mon. Wea. Rev.*, **128**, 2990–3000.

Avila, Lixion A., Richard J. Pasch, Jack L. Beven, James L. Franklin, Miles B. Lawrence, Stacy R. Stewart, Jiann-Gwo Jiing, 2003: Eastern North Pacific Hurricane Season of 2001. *Mon. Wea. Rev.*, **131**, 249–262.

Beven, John L., Lixion A. Avila, James L. Franklin, Miles B. Lawrence, Richard J. Pasch, Stacy R. Stewart, 2005: Eastern North Pacific Hurricane Season of 2003. *Mon. Wea. Rev.*, **133**, 1403–1414.

Bister, Marja, Kerry A. Emanuel, 1997: The Genesis of Hurricane Guillermo: TEXMEX Analyses and a Modeling Study. *Mon. Wea. Rev.*, **125**, 2662–2682.

Charney, J. G., and M. E. Stern, 1962: On the stability of internal baroclinic jets in a rotating atmosphere. *J. Atmos. Sci.,***19,** 159–172.

Chelton, Dudley B., Michael H. Freilich, Steven K. Esbensen, 2000a: Satellite

Observations of the Wind Jets off the Pacific Coast of Central America. Part I: Case

Studies and Statistical Characteristics. *Mon. Wea. Rev.*, **128**, 1993–2018.

Chelton, Dudley B., Michael H. Freilich, Steven K. Esbensen, 2000b: Satellite

Observations of the Wind Jets off the Pacific Coast of Central America. Part II: Regional

Relationships and Dynamical Considerations. *Mon. Wea. Rev.*, **128**, 2019–2043.

Dee, D. P., Uppala, S. M., Simmons, A. J., Berrisford, P., Poli, P., Kobayashi, S.,

Andrae, U., Balmaseda, M. A., Balsamo, G., Bauer, P., Bechtold, P., Beljaars, A. C. M.,

van de Berg, L., Bidlot, J., Bormann, N., Delsol, C., Dragani, R., Fuentes, M., Geer, A.

J., Haimberger, L., Healy, S. B., Hersbach, H., Hólm, E. V., Isaksen, L., Kållberg, P.,

Köhler, M., Matricardi, M., McNally, A. P., Monge-Sanz, B. M., Morcrette, J.-J., Park, B.-

K., Peubey, C., de Rosnay, P., Tavolato, C., Thépaut, J.-N. and Vitart, F. , 2011: The

ERA-Interim reanalysis: configuration and performance of the data assimilation system.

*Q.J.R. Meteorol. Soc.*, **137**, 553–597.

Haynes, P. H., M. E. McIntyre, 1987: On the Evolution of Vorticity and Potential Vorticity

in the Presence of Diabatic Heating and Frictional or Other Forces. *J. Atmos. Sci.*, **44**,

828–841.

Harrison, D. E.*, and* N. K. Larkin 1998*:* El Niño-Southern Oscillation sea surface

temperature and wind anomalies, 1946–1993*. Rev. Geophys.,* **36(3)***,* 353–399*.*

Hsieh, Jen-Shan, Kerry H. Cook, 2005: Generation of African Easterly Wave

Disturbances: Relationship to the African Easterly Jet. *Mon. Wea. Rev.*, **133**, 1311–

1327.

Jiang, X. *and* D. E. Waliser 2008*:* Northward propagation of the subseasonal variability

over the eastern Pacific warm pool*, Geophys. Res. Lett.,* **35***, L09814.*

Jiang, X. *and* D. E. Waliser 2009*: Two dominant subseasonal variability modes of the eastern Pacific ITCZ, Geophys. Res. Lett.,* **36***, L04704.*

Lau, Kai-Hon, Ngar-Cheung Lau, 1992: The Energetics and Propagation Dynamics of Tropical Summertime Synoptic-Scale Disturbances. *Mon. Wea. Rev.*, **120**, 2523–2539.

Maloney, Eric D. and Dennis L. Hartmann, 2001: The Madden–Julian Oscillation, Barotropic Dynamics, and North Pacific Tropical Cyclone Formation. Part I: Observations. *J. Atmos. Sci.*, **58**, 2545–2558.

Maloney, E. D., and S. K. Esbensen, 2003: The amplification of east Pacific Madden-Julian oscillation convection and wind anomalies during June-November. *J. Climate*, **16**, 3482-3497.

Maloney, Eric D., Steven K. Esbensen, 2007: Satellite and Buoy Observations of Boreal Summer Intraseasonal Variability in the Tropical Northeast Pacific. *Mon. Wea. Rev.*, **135**, 3–19.

Maloney, Eric D., Dudley B. Chelton, Steven K. Esbensen, 2008: Subseasonal SST variability in the tropical eastern north Pacific during boreal summer. *J. Climate*, **21**, 4149–4167.

Maloney, Eric D., Dennis L. Hartmann, 2000: Modulation of Eastern North Pacific Hurricanes by the Madden–Julian Oscillation. *J. Climate*, **13**, 1451–1460.

Maloney, Eric D., Michael J. Dickinson, 2003: The Intraseasonal Oscillation and the Energetics of Summertime Tropical Western North Pacific Synoptic-Scale Disturbances. *J. Atmos. Sci.*, **60**, 2153–2168.

Molinari, John, David Knight, Michael Dickinson, David Vollaro, Steven Skubis, 1997: Potential Vorticity, Easterly Waves, and Eastern Pacific Tropical Cyclogenesis. *Mon.*

*Wea. Rev.*, **125**, 2699–2708.

Molinari, John, David Vollaro, 2000: Planetary- and Synoptic-Scale Influences on Eastern Pacific Tropical Cyclogenesis. *Mon. Wea. Rev.*, **128**, 3296–3307.

Nitta, T., and Y. Takayabu, 1985: Global analysis of the lower tropospheric disturbances in the Tropics during the northern summer of the FGGE year. Part II: Regional characteristics of the disturbances. *Pure Appl. Geophys.*, **123,** 272–292.

Norquist, Donald C., Ernest E. Recker, Richard J. Reed, 1977: The Energetics of African Wave Disturbances as observed During Phase III of GATE. *Mon. Wea. Rev.*, **105**, 334–342.

North, Gerald R., Thomas L. Bell, Robert F. Cahalan, Fanthune J. Moeng, 1982: Sampling Errors in the Estimation of Empirical Orthogonal Functions. *Mon. Wea. Rev.*, **110**, 699–706.

Pasch, Richard J., and Coauthors, 2009: Eastern North Pacific Hurricane Season of 2006. *Mon. Wea. Rev.*, **137**, 3–20.

Raymond, D. D. J., López-Carrillo, C. and Cavazos, L. L., 1998: Case-studies of developing east Pacific easterly waves. *Q.J.R. Meteorol. Soc.*, **124**. 2005–2034.

Raymond, D. J., S. Gjorgjievska, S. Sessions, and Z. Fuchs, 2013: Tropical cyclogenesis and mid-level vorticity. *Australian Journal of Meteorology*, in press.

Rydbeck, Adam V., Eric D. Maloney, Shang-Ping Xie, Jan Hafner, Jeffrey Shaman, 2013: Remote Forcing versus Local Feedback of East Pacific Intraseasonal Variability during Boreal Summer. *J. Climate*, **26**, 3575–3596.

Serra, Yolande L., George N. Kiladis, Meghan F. Cronin, 2008: Horizontal and Vertical Structure of Easterly Waves in the Pacific ITCZ. *J. Atmos. Sci.*, **65**, 1266–1284.

Serra, Yolande L., George N. Kiladis, Kevin I. Hodges, 2010: Tracking and Mean Structure of Easterly Waves over the Intra-Americas Sea. *J. Climate*, **23**, 4823–4840.

Small, R. J., S.-P. Xie, E. D. Maloney, S. P. deSzoeke, and T. Miyama, 2011: Intraseasonal variability in the far-east Pacific: Investigation of the role of air-sea coupling in a regional coupled model. *Climate Dyn.*, **36**, 867–890.

Tai, King-Sheng, Yoshi Ogura, 1987: An Observational Study of Easterly Waves over the Eastern Pacific in the Northern Summer Using FGGE Data. *J. Atmos. Sci.*, **44**, 339–361.

Vitart, Frédéric, Timothy N. Stockdale, 2001: Seasonal Forecasting of Tropical Storms Using Coupled GCM Integrations. *Mon. Wea. Rev.*, **129**, 2521–2537.

Xie, S. P., H. Xu, W. S. Kessler, and M. Nonaka, 2005: Air-sea interaction over the eastern Pacific warm pool: Gap winds, thermocline dome, and atmospheric convection. *J. Climate*, **20**, 1504-1522.

Zhang, Chidong, Michael McGauley, Nicholas A. Bond, 2004: Shallow Meridional Circulation in the Tropical Eastern Pacific. *J. Climate*, **17**, 133–139.

**Chapter 3**

Aiyyer, A. R., and J. Molinari, 2008: MJO and Tropical Cyclogenesis in the Gulf of Mexico and Eastern Pacific: Case Study and Idealized Numerical Modeling. J. Atmos. Sci., **65**, 2837-2855.

Aiyyer, A., A. Mekonnen, and C. J. Schreck, 2012: Projection of tropical cyclones on wavenumber–frequency-filtered equatorial waves. J. Climate, 25, 3653–3658.

Avila, Lixion A. and J. L. Guiney, 2000: Eastern North Pacific Hurricane Season of 1998. *Mon. Wea. Rev.*, **128**, 2990-3000.

Avila, Lixion A., Richard J. Pasch, Jack L. Beven, James L. Franklin, Miles B. Lawrence, Stacy R. Stewart, and Jiann-Gwo Jiing, 2003: Eastern North Pacific Hurricane Season of 2001. *Mon. Wea. Rev.*, **131**, 249–262.

Back, Larissa E. and Christopher S. Bretherton, 2009: A Simple Model of Climatological Rainfall and Vertical Motion Patterns over the Tropical Oceans. *J. Climate*, **22**, 6477–6497.

Bretherton, C. S., M. E. Peters, and L. E. Back, 2004: Relationships between water vapor path and precipitable water over the tropical oceans. *J. Climate*, **17,** 1517–1528.

Carlson, Toby N., 1969: Synoptic Histories of Three African Disturbances That Developed Into Atlantic Hurricanes. *Mon. Wea. Rev.*, **97**, 256–276.

Crosbie, Ewan and Yolande Serra, 2014: Intraseasonal Modulation of Synoptic-Scale Disturbances and Tropical Cyclone Genesis in the Eastern North Pacific. *J. Climate*, **27**, 5724–5745.

Davis, Christopher, Chris Snyder, and Anthony C. Didlake Jr., 2008: A Vortex-Based Perspective of Eastern Pacific Tropical Cyclone Formation. *Mon. Wea. Rev.*, **136**, 2461–2477.

Dee, D. P., and Coauthors, 2011: The ERA-Interim reanalysis: Configuration and performance of the data assimilation system. *Quart. J. Roy. Meteor. Soc.*, **137**, 553–597

Dunn, Gordon E., 1940: Cyclogensis in the Tropical Atlantic. *Bull. Amer. Met. Soc.*, **21**, 215-229.

Frank, Neil L., 1969: The "Inverted V" Cloud Pattern—an Easterly Wave?. *Mon. Wea. Rev.*, **97**, 130–140.

Gu, G*., and* C. Zhang*,* 2002: Cloud components of the Intertropical Convergence Zone*.*

*J. Geophys. Res.,* **107***, 4565.*

Gu, G., R. F. Adler, G. J. Huffman, and S. Curtis, 2004: African easterly waves and their association with precipitation. *J. Geophys. Res.*, **109.** D04101.

Hartmann, D. L., and E. D. Maloney, 2001: The Madden-Julian oscillation, barotropic dynamics, and north Pacific tropical cyclone formation. Part II: Stochastic barotropic modeling. *J. Atmos. Sci.*, **58**, 2559-2570.

Holloway, Christopher E.  and J. David Neelin, 2009: Moisture Vertical Structure, Column Water Vapor, and Tropical Deep Convection. *J. Atmos. Sci.*, **66**, 1665–1683.

Hoover, Brett T., 2014: Identifying a Barotropic Growth Mechanism in East Pacific Tropical Cyclogenesis Using Adjoint-Derived Sensitivity Gradients. *J. Atmos. Sci.*, in press.

Jiang, X., and D. E. Waliser, 2008: Northward propagation of the subseasonal variability over the eastern Pacific warm pool. *Geophys. Res. Lett.*, **35**, L09814.

Jordan, C., 1958: Mean Soundings for the West Indies Area. *J. Meteor.*, **15**, 91-97.

Kiladis, George N., Chris D. Thorncroft, and Nicholas M. J. Hall, 2006: Three-Dimensional Structure and Dynamics of African Easterly Waves. Part I: Observations. *J. Atmos. Sci.*, **63**, 2212–2230.

King-Sheng Tai and Yoshi Ogura, 1987: An Observational Study of Easterly Waves over the Eastern Pacific in the Northern Summer Using FGGE Data. *J. Atmos. Sci.*, **44**, 339–361.

Krishnamurti, T. N. and David Baumhefner, 1966: Structure of a Tropical Disturbance Based on Solutions of a Multilevel Baroclinic Model. *J. Appl. Meteor.*, **5**, 396–406.

Lau, K.-H., and N.-C. Lau, 1992: The energetics and propagation dynamics of tropical

summertime synoptic-scale disturbances. *Mon. Wea. Rev.*, **120**, 2523–2539.

Lee, H.-T., 2014: Climate Algorithm Theoretical Basis Document (C-ATBD): Outgoing Longwave Radiation (OLR) - Daily. NOAA's Climate Data Record (CDR) Program, CDRP-ATBD-0526, 46 pp.

Malkus, Joanne S. and Herbert Riehl, 1964: Cloud structure and distributions over the tropical Pacific Ocean. *Tellus*, **16**, 275–287.

Maloney, E. D., and D. L. Hartmann, 2001: The Madden-Julian oscillation, barotropic dynamics, and north Pacific tropical cyclone formation. Part I: Observations. *J. Atmos. Sci.*, **58**, 2545-2558.

Maloney, E. D., and D. L. Hartmann, 2000: Modulation of eastern North Pacific hurricanes by the Madden–Julian oscillation. *J. Climate*, **13**, 1451–1460.

Maloney, E. D., and J. T. Kiehl, 2002: Intraseasonal eastern Pacific precipitation and SST variations in a GCM coupled to a slab ocean model. *J. Climate*, **15**, 2989-3007.

Maloney, E. D., and S. K. Esbensen, 2003: The amplification of east Pacific Madden-Julian oscillation convection and wind anomalies during June-November. *J. Climate*, **16**, 3482-3497.

Maloney, E. D., and S. K. Esbensen, 2005: A modeling study of summertime east Pacific wind-induced ocean-atmosphere exchange in the intraseasonal oscillation. *J. Climate*, **18**, 568-584.

Maloney, E. D., and S. K. Esbensen, 2007: Satellite and buoy observations of intraseasonal variability in the tropical northeast Pacific. *Mon. Wea. Rev.*, **135**, 3-19.

Maloney, E. D., D. B. Chelton, and S. K. Esbensen, 2008: Subseasonal SST variability in the tropical eastern north Pacific during boreal summer. *J. Climate*, **21**, 4149-4167.

Molinari, J., and D. Vollaro, 2000: Planetary and synoptic scale influences on eastern Pacific tropical cyclogenesis. *Mon. Wea. Rev.*, **128**, 3296-3307.

Nitta, Tsuyoshi and Yukari Takayabu, 1985: Global analysis of the lower tropospheric disturbances in the tropics during the northern summer of the FGGE year part II: Regional characteristics of the disturbances. *Pure and Applied Geophysics*. **123**, 272-292.

Nitta, T., 1978: A diagnostic study of interaction of cumulus updrafts and downdrafts with large-scale motions in GATE. *J. Meteor. Soc. Japan*, **56,** 232–242.

Palmer, C. E. 1952: Reviews of modern meteorology—5. Tropical meteorology. *Quart. J. Roy. Meteorol. Soc.*, **78**: 126–164.

Pasch, Richard J., Eric S. Blake, Lixion A. Avila, John L. Beven, Daniel P. Brown, James L. Franklin, Richard D. Knabb, Michelle M. Mainelli, Jamie R. Rhome, and Stacy R. Stewart, 2009: Eastern North Pacific Hurricane Season of 2006. *Mon. Wea. Rev.*, **137**, 3–20.

Peters, O., and J. D. Neelin, 2006: Critical phenomena in atmospheric precipitation. *Nature Phys.*, **2,** 393–396.

Petersen, Walter A., Robert Cifelli, Dennis J. Boccippio, Steven A. Rutledge, and Chris Fairall, 2003: Convection and Easterly Wave Structures Observed in the Eastern Pacific Warm Pool during EPIC-2001. *J. Atmos. Sci.*, **60**, 1754–1773.

Raymond, D. J., 2000: Thermodynamic control of tropical rainfall. *Quart. J. Roy. Meteor. Soc.*, **126,** 889–898.

Raymond, D. J., C. López Carrillo, and L. López Cavazos, 1998: Case-studies of developing east Pacific easterly waves. *Quart. J. Roy. Meteor. Soc.*, **124**, 2005–2034,

doi:10.1002/qj.49712455011.

Reed, Richard J., Donald C. Norquist, and Ernest E. Recker, 1977: The Structure and Properties of African Wave Disturbances as Observed During Phase III of GATE. *Mon. Wea. Rev.*, **105**, 317–333.

Riehl, Herbert, 1945: Waves in the Easterlies and the Polar Front in the Tropics. Dept. Meteor., University of Chicago, Misc. Reports No. 17.

Riehl, Herbert, 1948: On the formation of West Atlantic Hurricanes. Dept. Meteor., University of Chicago, Misc. Reports No. 24.

Riehl, Herbert, 1954: Tropical Meteorology. McGraw-Hill Book Company, New York, N.Y., 392 pp.

Rydbeck, Adam V. and Eric D. Maloney, 2014: Energetics of East Pacific Easterly Waves during Intraseasonal Events. *J. Climate*, **27**, 7603–7621.

Rydbeck, Adam V., Eric D. Maloney, Shang-Ping Xie, Jan Hafner, and Jeffrey Shaman, 2013: Remote Forcing versus Local Feedback of East Pacific Intraseasonal Variability during Boreal Summer. *J. Climate*, **26**, 3575–3596.

Sahany, Sandeep , J. David Neelin, Katrina Hales, and Richard B. Neale, 2012: Temperature–Moisture Dependence of the Deep Convective Transition as a Constraint on Entrainment in Climate Models. *J. Atmos. Sci.*, **69**, 1340–1358.

Simpson, R. H., Neil Frank, David Shideler, and H. M. Johnson, 1968: Atlantic Tropical Disturbances, 1967. *Mon. Wea. Rev.*, **96**, 251–259.

Serra, Yolande L. and Robert A. Houze Jr., 2002: Observations of Variability on Synoptic Timescales in the East Pacific ITCZ. *J. Atmos. Sci.*, **59**, 1723–1743.

Serra, Y. L., G. N. Kiladis, and M. F. Cronin, 2008: Horizontal and vertical structure of

easterly waves in the Pacific ITCZ. *J. Atmos. Sci.*, **65**, 1266-1284.

Serra, Y. L., G. Kiladis, and K. Hodges, 2010: Tracking and Mean Structure of Easterly Waves Over the Intra-Americas Sea. *J. Climate*, **23**, 4823-4840.

Small, R. J., S.-P. Xie, E. D. Maloney, S. P. deSzoeke, and T. Miyama, 2011: Intraseasonal Variability in the far-east Pacific: Investigation of the role of air-sea coupling in a regional coupled model. *Clim. Dyn.*, **36**, 867–890.

Sobel, A. H., S. E. Yuter, C. S. Bretherton, and G. N. Kiladis, 2004: Large-scale meteorology and deep convection during TRMM KWAJEX. *Mon. Wea. Rev.*, **132,** 422–444.

Sobel, Adam H. and Christopher S. Bretherton, 2000: Modeling Tropical Precipitation in a Single Column. *J. Climate*, **13**, 4378–4392.

Robert M. Thompson Jr., Steven W. Payne, Ernest E. Recker, and Richard J. Reed, 1979: Structure and Properties of Synoptic-Scale Wave Disturbances in the Intertropical Convergence Zone of the Eastern Atlantic. *J. Atmos. Sci.*, **36**, 53–72.

Wolding, B. O., and E. D. Maloney, 2015: Objective Diagnostics and the Madden-Julian Oscillation. Part II: Application to Moist Static Energy and Moisture Budgets. *J. Climate*, accepted pending revision

Yanai, M, 1961: A Detailed Analysis of Typhoon Formation. *J. Meteor. Soc. Japan*, **39**, 1987-214.

Yanai, M and Nitta T, 1967: Computation of Vertical Motion and Vorticity Budget in a Caribbean Easterly Wave. *J Meteor Soc Japan*, **45**, 444–466

## Chapter 4

Aiyyer, A. R., and J. Molinari, 2008: MJO and tropical cyclogenesis in the Gulf of Mexico and Eastern Pacific: Case study and idealized numerical modeling. *J. Atmos. Sci.*, **65,** 2691–2704.

Alaka, G. J., 2014: African Easterly Wave Energetics on Intraseasonal Timescales. Dissertation, Colorado State University, 214 pages.

Avila, L. A., and R. J. Pasch, 1992: Atlantic tropical systems of 1991. *Mon. Wea. Rev.,***120,** 2688–2696.

Avila, L. A., and R. J. Pasch, 1995: Atlantic tropical systems of 1993. *Mon. Wea. Rev.*, **123**, 887–896.

Beven, J. L., L. A. Avila, J. L. Franklin, M. B. Lawrence, R. J. Pasch, and S. R. Stewart, 2005: Eastern North Pacific hurricane season of 2006. *Mon. Wea. Rev.*, **133,** 1403–1414.

Blake, E. S. and T. B. Kimberlain, 2013: Eastern North Pacific Hurricane Season of 2011. *Mon. Wea. Rev.*, **141**, 1397–1412.

Blake, E. S. and R. J. Pasch, 2010: Eastern North Pacific Hurricane Season of 2008. *Mon. Wea. Rev.*, **138**, 705–721.

Chelton, D. B., M. H. Freilich, and S. K. Esbensen, 2000a: Satellite observations of the wind jets off the Pacific coast of Central America. Part I: Case studies and statistical characteristics. *Mon. Wea. Rev.*, **128**, 1993–2018.

Chelton, D. B., M. H. Freilich, and S. K. Esbensen, 2000b: Satellite observations of the wind jets off the Pacific coast of Central America. Part II: Regional relationships and dynamical considerations. *Mon. Wea. Rev.*, **128**, 2019–2043.

Collins, J. M., 2010: Contrasting High North-East Pacific Tropical Cyclone Activity with Low North Atlantic Activity. *Southern Geographer*, **50**(1), 83-98.

Collins, W. D., and Coauthors, 2004: Description of the NCAR Community Atmosphere Model (CAM 3.0). NCAR Tech. Note NCAR/TN-464+STR, 226 pp. [Available online at http://www.cesm.ucar.edu/models/atm-cam/docs/description/description.pdf.]

Crosbie E. and Y. Serra, 2014: Intraseasonal Modulation of Synoptic-Scale Disturbances and Tropical Cyclone Genesis in the Eastern North Pacific. *J. Climate*, **27**, 5724–5745.

Dee, D. P., and Coauthors, 2011: The ERA-Interim reanalysis: Configuration and performance of the data assimilation system. *Quart. J. Roy. Meteor. Soc.*, **137**, 553–597.

Dunn, G. E., 1933: Tropical Storms of 1933. *Mon. Wea. Rev.*, **61**, 362–363.

Esbensen, S. K., E. I. Tollerud, and J-H. Chu, 1982: Cloud-cluster-scale circulations and the vorticity budget of synoptic-scale waves over the eastern Atlantic intertropical convergence zone. *Mon. Wea. Rev.*, **110,** 1677–1692.

Ferreira, R. N., and W. H. Schubert, 1997: Barotropic aspects of ITCZ breakdown. *J. Atmos. Sci.,***54,** 261–285.

Frank, N. L., 1970: Atlantic tropical systems of 1969. *Mon. Wea. Rev.,***98,** 307–314.

Frank, W. M., and G. S. Young, 2007: The interannual variability of tropical cyclones. *Mon. Wea. Rev.*, **135,** 3587–3598.

Hartmann, D. L., and E. D. Maloney, 2001: The Madden–Julian oscillation, barotropic dynamics, and North Pacific tropical cyclone formation. Part II: Stochastic barotropic modeling. *J. Atmos. Sci.*, **58,** 2559–2570.

Haynes, P.H. and M. E. McIntyre, 1987: On the Evolution of Vorticity and Potential Vorticity in the Presence of Diabatic Heating and Frictional or Other Forces. *J. Atmos. Sci.*, **44**, 828–841.

Holton, J. R., J. A. Wallace, and J. M. Young 1971: On Boundary Layer Dynamics and the ITCZ. *J. Atmos. Sci.*, **28**, 275-280.

Hong, S.-Y., and J. O. J. Lim, 2006: The WRF single moment 6-class microphysics scheme (WSM6). *J. Korean Meteor. Soc.*, **42**, 129–151.

Hong, S.-Y., Y. Noh, and J. Dudhia, 2006: A new vertical diffusion package with an explicit treatment of entrainment processes. *Mon. Wea. Rev.*, **134**, 2318–2341.

Jin, C.S., C.H. Ho, J.H. Kim, D.K. Lee, D.H. Cha, and S.W. Yeh, 2013: Critical Role of Northern Off-Equatorial Sea Surface Temperature Forcing Associated with Central Pacific El Niño in More Frequent Tropical Cyclone Movements toward East Asia. *J. Climate*, **26**, 2534–2545.

Johnson, Richard H. and Paul E. Ciesielski, 2013: Structure and Properties of Madden–Julian Oscillations Deduced from DYNAMO Sounding Arrays. *J. Atmos. Sci.*, **70**, 3157–3179.

Kain, J. S. 2004: The Kain–Fritsch Convective Parameterization: An Update. *J. Appl. Meteor.*, **43**, 170–181.

Kim, D., C.S. Jin, C.H. Ho, J. Kim, J.H. Kim: 2015: Climatological features of WRF-simulated tropical cyclones over the western North Pacific. *Clim. Dyn.*, **44**, 3223-3235.

Lau K.H. and Lau N.C., 1992: The Energetics and Propagation Dynamics of Tropical Summertime Synoptic-Scale Disturbances. *Mon. Wea. Rev.*, **120**, 2523–2539.

Maloney, E. D., and D. L. Hartmann, 2001: The Madden–Julian oscillation, barotropic dynamics, and North Pacific tropical cyclone formation. Part I: Observations. *J. Atmos. Sci.*, **58,** 2545–2558.

Mallard, M. S., G. M. Lackmann, A. Aiyyer, and K. Hill, 2013: Atlantic Hurricanes and Climate Change. Part I: Experimental Design and Isolation of Thermodynamic Effects. *J. Climate*, **26**, 4876–4893.

Mapes, B. E., T. T. Warner, M. Xu, and A. J. Negri, 2003: Diurnal patterns of rainfall in northwestern South American. Part I: Observations and context. *Mon. Wea. Rev.*, **131,** 799–812.

Mapes, B. E., T. T. Warner, and M. Xu, 2003a: Diurnal patterns of rainfall in northwestern South America. Part III: Diurnal gravity waves and nocturnal convection offshore. *Mon. Wea. Rev.*, **131,** 830–844.

Molinari, J., S. Knight, M. Dickinson, D. Vollaro, and S. Skubis, 1997: Potential vorticity, easterly waves, and eastern Pacific tropical cyclogenesis. *Mon. Wea. Rev.*, **125,** 2699–2708.

Molinari J. and D. Vollaro, 2000: Planetary- and Synoptic-Scale Influences on Eastern Pacific Tropical Cyclogenesis. *Mon. Wea. Rev.*, **128**, 3296–3307.

Mozer, J. B., and J. A. Zehnder, 1996: Lee vorticity production by large-scale tropical mountain ranges. Part I: Eastern North Pacific tropical cyclogenesis. *J. Atmos. Sci.,* **53,** 521–538.

Nitta, Tsuyoshi and Yukari Takayabu, 1985: Global analysis of the lower tropospheric disturbances in the tropics during the northern summer of the FGGE year part II:

Regional characteristics of the disturbances. *Pure and Applied Geophysics*. **123**, 272-292.

Peters, M. E., Z. Kuang, and C. C. Walker, 2008: Analysis of Atmospheric Energy Transport in ERA-40 and Implications for Simple Models of the Mean Tropical Circulation. *J. Climate*, **21**, 5229–5241.

Reed, R. J., and R. H. Johnson, 1974: The vorticity budget of synoptic-scale wave disturbances in the tropical western Pacific. *J. Atmos. Sci.*, **31,** 1784–1790.

Rydbeck, A. V. and E. D. Maloney, 2014: Energetics of East Pacific Easterly Waves during Intraseasonal Events. *J. Climate*, **27**, 7603–7621.

Rydbeck, A. V. and E. D. Maloney, 2015: On the Convective Coupling and Moisture Organization of East Pacific Easterly Waves, *J. Climate*, in press.

Schreck, C. J., J. Molinari, and A. Aiyyer, 2012: A global view of equatorial waves and tropical cyclogenesis. *Mon. Wea. Rev.*, **140**, 774–788.

Serra, Y. L., G. N. Kiladis, and M. G. Cronin, 2008: Horizontal and vertical structure of easterly waves in the Pacific ITCZ. *J. Atmos. Sci.*, **65,** 1266–1284.

Serra, Y. L., G. N. Kiladis, and K. I. Hodges, 2010: Tracking and mean structure of easterly waves over the intra-Americas sea. *J. Climate*, **23**, 4823–4840.

Shapiro, L. J., 1986: The three-dimensional structure of synoptic-scale disturbances over the tropical Atlantic. *Mon. Wea. Rev.,***114,** 1876–1891.

Simpson, R. H., N. Frank, D. Shideler, and H. M. Johnson, 1969: Atlantic tropical disturbances of 1968. *Mon. Wea. Rev.,***97,** 240–255.

Small, R. J., S.-P. Xie, E. D. Maloney, S. P. deSzoeke, and T. Miyama, 2011: Intraseasonal variability in the far-east Pacific: Investigation of the role of air-sea coupling in a regional coupled model. *Climate Dyn.*, **36**, 867–890.

Stevens, D. E., 1979: Vorticity, momentum, and divergence budgets of synoptic-scale wave disturbances in the tropical eastern Atlantic. *Mon. Wea. Rev.*, **107,** 535–550.

Tai K. S.and Y. Ogura, 1987: An Observational Study of Easterly Waves over the Eastern Pacific in the Northern Summer Using FGGE Data. *J. Atmos. Sci.*, **44**, 339–361.

Thiébaux, J., E. Rogers, W. Wang, and B. Katz, 2003: A new high-resolution blended real-time global sea surface temperature analysis. *Bull. Amer. Meteor. Soc.*, **84**, 645–656.

Thompson G., P. R. Field, R. M. Rasmussen, and W. D. Hall, 2008: Explicit Forecasts of Winter Precipitation Using an Improved Bulk Microphysics Scheme. Part II: Implementation of a New Snow Parameterization. *Mon. Wea. Rev.*, **136**, 5095–5115.

Thorncroft, C., and K. Hodges, 2001: African easterly wave variability and its relationship to Atlantic tropical cyclone activity. *J. Climate*, **14,** 1166–1179.

Thorncroft, C. D., N. M. J. Hall, and G. N. Kiladis, 2008: Three-Dimensional Structure and Dynamics of African Easterly Waves. Part III: Genesis. *J. Atmos. Sci.*, **65**, 3596–3607.

Tulich, S. N., G. N. Kiladis, and A. Suzuki-Parker, 2011: Convectively coupled Kelvin and easterly waves in a regional climate simulation of the tropics. *Clim. Dyn.*, **36**, 185-203.

Tyner B. and A. Aiyyer, 2012: Evolution of African Easterly Waves in Potential Vorticity Fields. *Mon. Wea. Rev.*, **140**, 3634–3652.

Toma, V. and P. J. Webster, 2010: Oscillations of the intertropical convergence zone and the genesis of easterly waves. I Theory and diagnostics. *Clim. Dyn.*,**34**,587-604.

Toma, V. and P. J. Webster, 2010: Oscillations of the intertropical convergence zone and the gensis of eeasterly waves. II Numerical experiments. *Clim. Dyn.*,**34**,605-613.

Velasco, I.*, and* J. M. Fritsch, 1987*:* Mesoscale convective complexes in the Americas*, J. Geophys. Res.,* **92***,* 9591–9613.

Warner, T. T., B. E. Mapes, and M. Xu, 2003: Diurnal patterns of rainfall in northwestern South America. Part II: Model simulation and comparison with observations. *Mon. Wea. Rev*, **131,** 813–829.